NUCLEAR MAGNETIC RESONANCE STUDIES OF SOLID STATE LITHIUM ION BATTERY MATERIALS

by

Yifeng Wang

A dissertation submitted to the Graduate Faculty in
Physics in partial fulfillment of the requirements
for the degree of Doctor of Philosophy,
The City University of New York

1999

This manuscript has been read and accepted for the Graduate Faculty in Physics in satisfaction of the dissertation requirement for the degree of Doctor of Philosophy.

5/19/99 — Date

Professor Steve G. Greenbaum, Chair of Examining Committee

5/25/99 — Date

Professor Louis Celenza, Executive Officer

Professor Marten denBoer

Professor Robert A. Marino

Professor Phillip Stallworth

Professor Ruth E. Stark

Supervisory Committee

THE CITY UNIVERSITY OF NEW YORK

Abstract

NUCLEAR MAGNETIC RESONANCE STUDIES OF

SOLID STATE LITHIUM ION BATTERY MATERIALS

by

Yifeng Wang

Advisor: Professor Steve G. Greenbaum

A variety of materials used in lithium ion battery development have been investigated by solid state ^{6,7}Li NMR.

In lithiated hard carbon, ^{7}Li high-resolution NMR measurements reveal two distinct insertion mechanisms, one is intercalation between disordered graphene planes and the other is covalently bonded with in amorphous hydrogen-containing regions of the carbon. The irreversible portion of the Li, which constitutes the solid electrolyte interface (SEI), was detected. ^{7}Li NMR results of lithiated natural graphite and mildly oxidized graphite show that the SEI formation is more efficient in latter, and that there is excess reversible capacity not associated with intercalated Li.

With measurements of electrochemically lithiated SnO by NMR, Li_2O and Li_xSn phases were detected at low and intermediate Li contents, and the $Li_{x-2}Sn$ alloy structure is significantly different at high Li content.

^{6,7}Li NMR spectroscopic measurements of $Li_{1+y}CoO_2$ (y=0.08, 0.35) suggest that only a small fraction (about 10% of the excess Li) may be reversible, the remainder of the excess are various impurities.

For physical mixtures of LiI and nano-scale particles of Al_2O_3, the high resolution (MAS) NMR method clearly resolves two or more distinct Li^+ sites, one characteristic of bulk LiI and the rest associated with surface/interface regions.

Composite solid electrolytes based on PEO, LiI and high surface area inorganic oxides were investigated. The MAS NMR spectrum of a sample with a PEO/Li ratio of 3/2 is consistent with at least two Li environments, one solvated by the polymer and one in small ionic clusters at room temperature. The Li environment becomes more purely ionic as the polymer-associated peak vanishes above 80 °C.

^{6,7}Li NMR results in Li-Co-Ni-O and Li-(Cr, Fe)-Mn-O sample systems are also presented.

ACKNOWLEDGMENTS

I owe special thanks to my advisor, Professor **Steve Greenbaum**, who advised me patiently on a variety of academic issues as well as supported me invaluably on many personal issues during the last five years. His guidance, helpful suggestions as well as encouragement on this thesis are always appreciated.

I am very grateful to the following people who provided samples for NMR experiments. They are Dr. Peled, Dr. Golodnitsky, Ms. Ardel, and Dr. Menachem, Mr. Eshkenazi in Tel Aviv University, and Dr. Croce, Dr. Carewska, and Dr. Scaccia in Roma University, and Mr. Chang and Dr. Kumta in Carnegie Mellon University, and Mr. Sakamoto, Dr. Huang and Dr. Surampudi at the Jet Propulsion Laboratory.

I also wish to thank Professors Marten denBoer, Robert A. Marino, Phillip Stallworth and Ruth E. Stark for their friendly participation in the examination committee and reading this manuscript.

I would also like to thank all the people who help me during this work.

I dedicate this paper to my grandmother on whose thin back I grew up. A strong hug goes to my wife and son who always show me understanding and support.

Financial support for this project was provided by grants from the Office of Naval Research and the Department of Energy.

Table of Contents

Page

Chapter 1. Introduction: Materials Under Investigation 1

1-1. Cathode materials 4

1-1.1. Lithium -(Co, Ni, Mn)-O materials 4

1-2. Anode materials 10

1-2.1. Carbonaceous materials 10

1-2.2. Lithium – tin materials 16

1-3. Composite electrolyte 17

1-3.1. The mixture of LiI and Al_2O_3 17

1-3.2. PEO-LiI complexes 19

1-4. Solid electrolyte interface (SEI) 20

Chapter 2. Theoretical Background of NMR 22

2-1. Basic phenomenon and theory of NMR 22

2-2. Relaxation 28

2-3. NMR interactions in solids 32

2-3.1. Zeeman interaction 34

2-3.2. Dipole-Dipole interaction 34

2-3.3. Quadrupole interaction 37

2-3.4. Electron interaction 42

Chapter 3. Research Methods.....46

3-1. Solid state NMR techniques.....46

3-1.1. Single pulse and echo pulse sequences.....46

3.1.2. Pulse sequences for T_1 measurements.....50

3-1.3. High resolution NMR techniques.....52

3-1.3.1. Magic Angle Spinning (MAS) technique.....52

3-1.3.2. Double-resonance techniques.....55

3-2. Experimental equipment.....57

3-2.1. NMR spectrometer.....57

3-2.1.1. Two resonance channels.....57

3-2.1.2. Magnet.....58

3-2.1.3. Solid temperature controller.....58

3-2.1.4. MAS speed controller.....58

3-2.1.5. Probes.....59

3-2.1.6. Spectrometer Control Program.....60

Chapter 4. Experimental Results and Discussions.....63

4-1. Intercalation compounds of graphite Li_xC for electrode materials.....63

4-1.1. Material I: Lithium battery anode materials based on disordered, hard carbon.....63

1. Samples and experiments.....63

2. Experimental results.....65

3. Discussions.....73

4-1.2. Material II: Lithiated natural graphite before and after mild oxidation....77

1. Samples and experiments....77

2. Experimental results and discussions....78

4-2. New anode materials Li-SnO....82

4-2.1. Sample background and experiments....82

4-2.2. Experimental results and discussions....83

4-2.3. Sub-conclusions....89

4-3. Battery cathode material $Li_{1+y}CoO_2$....90

4-3.1. Samples and experiments....90

4-3.2. Experimental results and discussions....91

4-3.3. Sub-conclusions....104

4-4. $LiCo_xNi_{1-x}O_2$....105

4-4.1. Sample background....105

4-4.2. Experimental results and discussions....105

4-5. $Li(Cr,Fe)_xMn_{2-x}O_4$....110

4-5.1. Experimental results and discussions....110

4-6. LiI/Al_2O_3 mixture....112

4-6.1. Sample background and experiments....112

4-6.2. Experimental results and discussions....113

4-6.3. Sub-conclusions....127

4-7. Composite solid electrolytes based on PEO, LiI and high surface area inorganic....128

4-7.1. Sample background and experiments 128

4-7.2. Experimental results and discussions 128

4-7.3. Subconclusions 136

4-8. Summary of conclusions 138

References 141

List of Tables

1-1. Summarized characteristics of cathode materials $LiCoO_2$, $LiNiO_2$, $LiMn_2O_4$ and $LiCo_xNi_{1-x}O_2$.....6

4-1. Li content of the hard carbon samples, as determined by potential vs. capacity(V/C) or NMR.....71

4-2. The spin–lattice relaxation T_1 of $Li_{1+y}CoO_2$ (y=0.0, 0.08 and 0.35).....92

4-3. Chemical (paramagnetic) shifts of extra components in non stoichiometric $Li_{1+y}CoO_2$ at various temperatures.....94

4-4. Nominal (y) and experimental (y*) lithium content, water soluble lithium, average oxidation state of Co for $Li_{1+y}CoO_2$ and chemical composition.....100

4-5. Lithium-6 and Lithium-7 line widths(full width at half maximum) of $Li_{1+y}CoO_2$, with and without Mg, at room temperature.....101

4-6. The spin-lattice relaxation time T_1 of sample system $LiCo_xNi_{1-x}O_2$(x=0,1/4)...107

4-7. ^7Li line widths (FWHM) and chemical shifts of $Li(Cr,Fe)_xMn_{2-x}O_4$.....110

4-8. ^6Li line widths (FWHM) and chemical shifts of $Li(Cr,Fe)_xMn_{2-x}O_4$.....110

List of Figures

1-1. The scheme of a lithium ion battery....3

1-2. The schematic diagram of the layered rock salt structure....5

1-3. The schematic diagram of the spinel structure....6

1-4. The schematic diagram of the carbonization process involved in the preparation of various carbon materials 12

1-5. The schematic representation of supposed lithium doping/undoping process in disordered carbon....13

1-6. The schematic model of lithium insertion into and extraction from Disordered carbons....14

1-7. The structure of $Li_{22}Sn_5$....18

2-1. Zeeman energy levels for spin -1/2 and spin -3/2 cases....23

2-2. Effect of rf pulse on magnetization....27

2-3. A FID and its spectrum....28

2-4. Rotating frame diagrams for relaxation....31

2-5. The interactions between a nuclear and its surrounding. 33

2-6. The dipolar interaction of two spins....35

2-7. The orientation of the principal-axis frame of EFG(x,y,z) relative to laboratory frame(X,Y,Z)....39

2-8. Quadrupole splitting of the magnetic resonance of a nucleus of spin 3/2....45

3-1. The sample packing in MAS experiments....46

3-2. The classical picture of single pulse....47

3-3. The classical picture of spin echo....49

3-4. Inversion recovery sequence to determine T_1....51

3-5. Saturation recovery sequence to determine T_1....52

3-6. Diagram illustrating the geometry of the MAS experiment....53

3-7. A typical MAS spectrum....54

3-8. Decoupling pulse sequence....55

3-9. CP pulse sequence....56

3-10. Schematic diagram of matching network for MAS probe....59

3-11. Schematic diagram of matching network for static probe....60

4-1. Charge/discharge curve of Li/carbon cell....64

4-2. High resolution ^{7}Li NMR spectra of fully lithiated (sample No.1, bottom), partially delithiated (sample No.2, middle), and totally delithiated (sample No.3, top) hard carbon....66

4-3. Wide line ^{7}Li NMR spectrum of fully lithiated hard carbon (samples No.1)....68

4-4. Simulation (solid curves) of experimental spectra (discrete points) with simulated spectral components....70

4-5. High resolution ^{7}Li NMR spectra of partially delithiated hard carbon....72

4-6. High resolution ^{7}Li NMR spectra of LiH....74

4-7. Structural model of hard carbon depicting intercalation....76

4-8. Wide-line ^{7}Li NMR spectra of lithiated pristine NG7, $Li_{0.21}C_6$....78

4-9. High resolution MAS ^{7}Li NMR spectra of lithiated pristine NG7, $Li_{0.21}C_6$....81

4-10. High resolution ^{7}Li NMR spectra of electrochemically lithiated SnO....84

4-11. High resolution ^{7}Li NMR spectra of electrochemically lithiated SnO, with

Li/SnO ratio of 4.3.....86

4-12. High resolution ^{7}Li NMR spectra of: (a) $Li_{4.4}Sn$ reference alloy; (b) electrochemically lithiated SnO with Li/SnO ratio of 6.4.....88

4-13. NMR spectra of stoichiometric $LiCoO_2$.....93

4-14. Expanded vertical-scale NMR spectra of $Li_{1.35}CoO_2$.....96

4-15. Expanded vertical-scale ^{7}Li absorption spectrum of $Li_{1.08}CoO_2$.....97

4-16. Lithium-7 MAS (7 kHz spinning rate) absorption spectrum of $Li_{1.35}CoO_2$ under inversion recovery.....98

4-17. (a) Lithium-6 MAS (6 kHz spinning rate) spectrum of $Li_{1.35}CoO_2$. Spinning side bands appear at ±6 kHz. (b) Same as (a) with expanded horizontal scale...99

4-18. Lithium –7 wide line spectrum of $Li_{1.08}CoO_2$:Mg.....102

4-19. Lithium-7 MAS (spinning rate 7 kHz) spectra of (a) $Li_{1.08}CoO_2$:Mg; (b) stoichiometric $LiCoO_2$.....103

4-20. Line widths with temperature for $LiNiO_2$ precursors.....106

4-21. Line widths with temperatures for $LiNiO_2$, $LiNiO_2$ (5% excess Li), $LiCo_{1/4}Ni_{3/4}O_2$, and $LiCo_{1/4}Ni_{3/4}O_2$(5% excess Li).....108

4-22. Arrhenius plot of line widths of $LiCo_xNi_{1-x}O_2$ series.....109

4-23. Lithium-7 wide-line NMR spectra of Series A LiI/Al_2O_3 samples, at 23°C.....114

4-24. Variable temperature ^{7}Li MAS NMR spectra of Series A LiI/Al_2O_3 sample (50/50).....115

4-25. Variable temperature ^{7}Li MAS spectra of Series A LiI/Al_2O_3 sample (60/40).....116

4-26. Variable temperature ^{7}Li MAS NMR spectra of Series A LiI/Al_2O_3

sample (70/30).....117

4-27. Comparison between variable temperature ^{7}Li MAS NMR spectra of Series A and Series B LiI/Al_2O_3 samples: (a) 50/50, Series A – left, Series B – right.....119

4-28. Comparison between variable temperature ^{7}Li MAS NMR spectra of Series A and Series B LiI/Al_2O_3 samples: (a) 70/30, Series A – left, Series B – right.....120

4-29. Variable temperature ^{127}I wide-line NMR spectra of 60/40 LiI/Al_2O_3, Series A – left, Series B – right.....122

4-30. Variable temperature ^{127}I MAS NMR spectra of 60/40 LiI/Al_2O_3 Series B sample.....123

4-31. Variable temperature ^{127}I spin lattice relaxation time (T_1) of Series B samples.....124

4-32. ^{7}Li spin-lattice relaxation of the -4.5 ppm peak vs. the content of Al_2O_3 in LiI/Al_2O_3.....125

4-33. Wide-line ^{7}Li NMR spectra of LiI(1)PEO(1.5)+ 6%V/V Al_2O_3 at different temperature.....130

4-34. Wide-line ^{7}Li NMR spectra of LiI(1)PEO(3)+ 12%V/V Al_2O_3 at different temperature.....131

4-35. Wide-line ^{7}Li NMR spectra of LiI(1)PEO(9)PMMA(1) EC(1) + 6%Al_2O_3 at different temperature.....132

4-36. Temperature dependence of full-width-at-half-height ^{7}Li linewidth for several CSE samples.....133

4-37. High resolution CP/MAS (spinning rate 5.5 kHz) ^{7}Li NMR spectra of CSE samples.....135

Chapter 1. Introduction: Materials under Investigation

For a long time, scientists and engineers have been working to develop higher performance ionic conductors and lithium insertion compounds. The need for the materials is urgent for the following industry areas: rechargeable batteries, high quality capacitors, electrochromics and so on. Due to the complexity and variety of the ionic conductors, various highly sophistical methods have been employed to study the materials [1] among which are solid state Nuclear Magnetic Resonance (NMR). With the continuing development in its theories and techniques, NMR has been shown to be a powerful method for the investigation.

There are certain advantages to using the well-established NMR techniques in the study of ionic conductors and lithium insertion compounds. First, by using a nuclear specific probe, NMR techniques provide a method to gain information on a material's structure at the atomic level. Second, NMR techniques can be used to explore the process of ionic transport that is the basis of ionic conductivity. To understand the ionic transport mechanism and to reveal the structure characteristic that controls the ionic transport process are of primary significance in the ionic conductor study. The power of the NMR technique matches with the above research interests perfectly. The result of NMR study can be fed back into the materials research field to enhance the development of new ionic conductors.

This thesis describes the use of solid state NMR methods to investigate the ionic conductors and lithium insertion compounds with the following emphases:

1. Using solid state NMR to explore microstructure characteristics of ionic rechargeable battery materials. The major interest includes the study of the environment around NMR nuclei, the structural distortion of crystal field, the interaction among like-nuclei and unlike-nuclei, the scale effect of particles as well as the interface effect between different phases in samples.

2. Using the solid state NMR method to investigate transport behaviors and ionic dynamics as function of temperature.

Batteries are a necessity in the life of modern human beings. Batteries with small size and high capacity are in demand by many civil industry and military industry fields. Further more, rechargeable batteries that are stable in a broad range of temperatures are often sought. Non-stop demand has made battery research and development flourish for over 100 years. In this old research and industry family, there is a new baby of only twenty years, the rechargeable lithium batteries that offer significant performance and low-cost advantages compared to the traditional Ni-Cd and Ni-H_2 batteries. Murphy *et al* was the first to propose using insertion compounds (e.g. $LiWO_4$) as the negative electrode in the lithium batteries in 1978 [2]. The specific attractions of the rechargeable lithium batteries are their ability to provide higher specific energy, higher current density and so on. Comparing to the SOA aerospace battery family, such as Ni-Cd and Ni-H_2, the rechargeable lithium battery family has 2-4 times specific energies (Wh/kg) and energy densities (Wh/l) of that of SOA advanced versions of nickel-cadmium and nickel-hydrogen batteries. Three typical lithium batteries are presently under development around the world. They are lithium metal, lithium-ion, and lithium polymer electrolyte

battery. This study will focus on the materials relative to rechargeable lithium batteries. Briefly, lithium ion battery consists of a lithium transition metal oxide cathode and a carbon compound anode, with a porous polymer separator and a non-aqueous electrolyte between the electrodes. As the battery is charged and discharged, the lithium ions shift back and forth between the cathode and anode. **Figure 1-1** is a typical schematic diagram of a lithium-ion cell.

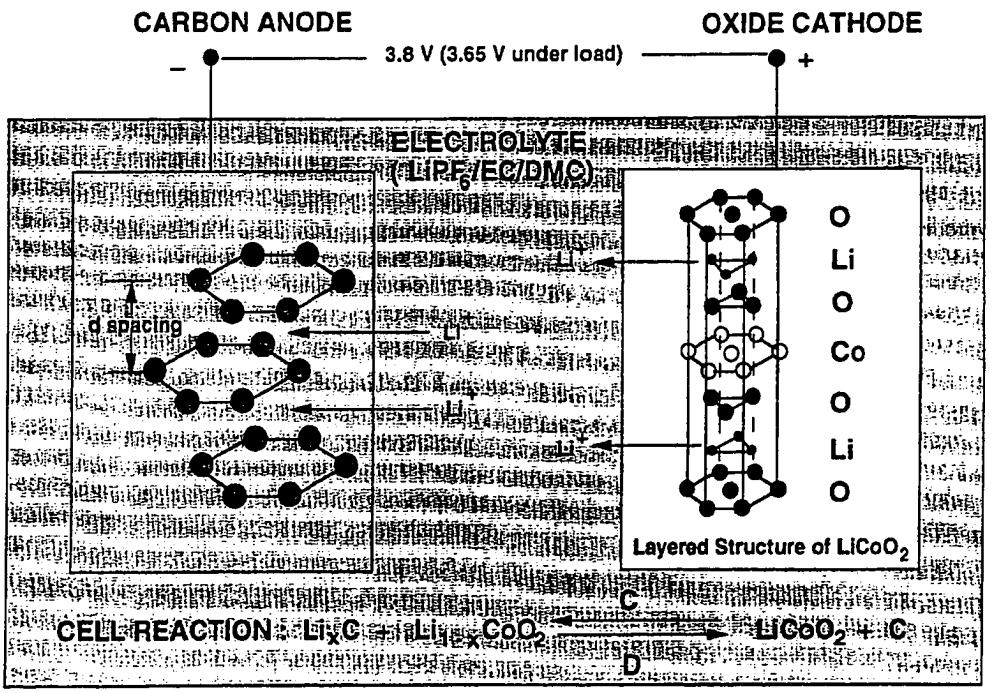

Figure 1-1: The scheme of a lithium ion battery.

1-1. Cathode materials

Rechargeable lithium ion batteries can use a wide variety of intercalation compounds as cathodes. The requirements of lithium ion cathode materials are their high voltage vs. Li, good reversibility, high lithium ion mobility, and minimal changes in crystal structure due to lithium ion intercalation and deintercalation reactions, good electronic conductivity, chemical and electrochemical stability, and non-toxicity. Recently identified intercalation compounds that meet the above requirements are $Li_{1-x}CoO_2$, $Li_{1-x}NiO_2$, $Li_{1+x}Mn_2O_4$, and $Li_{1+x}V_3O_8$ [3-6].

1-1.1. Lithium- (Co, Ni, Mn)-O materials

For over a decade, layered $LiNiO_2$ [7] and $LiCoO_2$ [6,8] have both been proposed to be used as the electrode materials in secondary Li batteries. Batteries assembled in the charged state have cathodes of form of $Li_{1-x}CoO_2$ (x=0~0.5) and $Li_{1-x}NiO_2$ (x=0~0.5), which can be prepared with electrochemical methods by deintercalation of Li from either $LiNiO_2$ or $LiCoO_2$. On the other hand, in 90's Dahn et al [9] stated that Li_2CoO_2 does not form by electrochemical intercalation of Li in $LiCoO_2$ as it does in the analogous Li_2NiO_2. Later, $Li_{1+x}CoO_2$ (x<0.2) with rich Li was also investigated by Dr. Croce et al [10] who are our collaborators. On developing the above two new materials for Li battery, the basic idea is to increase a material's Li-capacity. A secondary goal is that its electrical conductivity as cathode might be enhanced. Both $LiCoO_2$ and $LiNiO_2$ families show a layered rock-salt type structure illustrated in **Figure 1-2.**

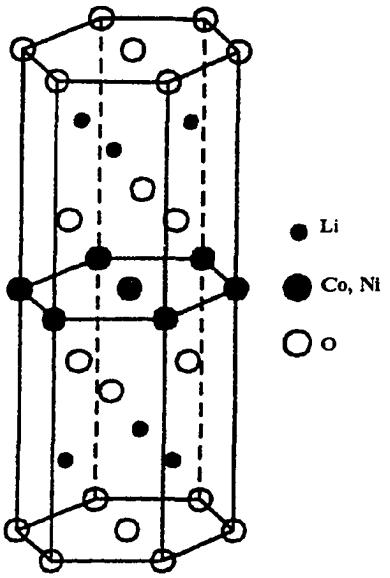

Figure 1-2: The schematic diagram of the layered rock salt structure.

It is well known that $Li_{1-x}CoO_2$ is one of the best cathode materials in secondary lithium batteries and is the basis of the commercial (SONY) Li ion technology. The cell voltages of $Li/Li_{1-x}CoO_2$ lie in the range of 3.5 ~ 4.5V. In market, $LiCoO_2$ is very expensive ($80-140/kg) compared to $LiNiO_2$ (only $18-30/kg). Under economic consideration as well as based on the fact that the two have same chemical structure, some groups have been developing a combination of $LiCo_xNi_{1-x}O_2$ [11]. Some groups also have been pioneering the use of $LiMn_2O_4$ and $Li(Mn_{2-x}Co_x)O_4$ systems. The parent structure of $Li(Mn_{2-x}Co_x)O_4$ systems is called spinel (see **Figure 1-3**).

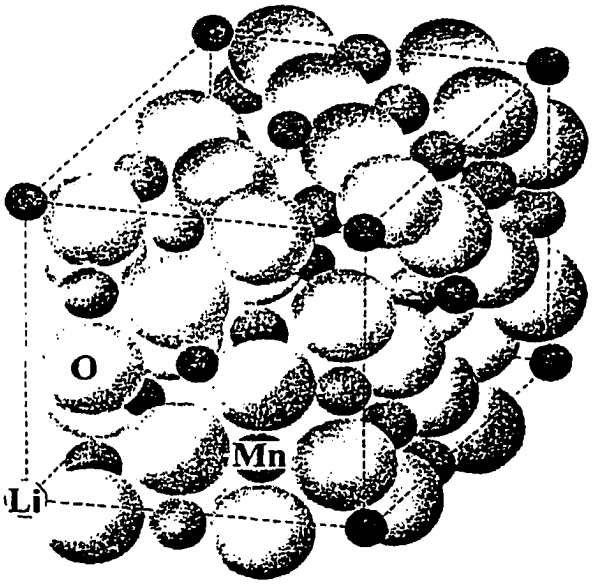

Figure 1-3: The schematic diagram of the spinel structure.

Also $LiMnO_2$ with a layered structure was synthesized by Capitaine et al [12]. The material is a new candidate as a cathode used in lithium ionic batteries. **Table 1-1** summarizes characteristics of cathode materials $LiCoO_2$, $LiNiO_2$, $LiMn_2O_4$ and $LiCo_xNi_{1-x}O_2$.

Table 1-1 Summarized characteristics of cathode materials $LiCoO_2$, $LiNiO_2$, $LiMn_2O_4$ and $LiCo_xNi_{1-x}O_2$.

Material	$LiCoO_2$	$LiNiO_2$	$LiMn_2O_4$	$LiCo_xNi_{1-x}O_2$
Structure	Layered	Layered	Spinel	Layered
Cost	\$80-140/kg	\$18-30/kg	\$7-30/kg	Moderate
Average Capacity	140mAh/g	160mAh/g	120mAh/g	Lower capacity than pure $LiNiO_2$

Li-Co-O cathode materials have been extensively studied by electrochemical and X-ray methods and a lot of valuable information has been obtained. However, X-ray scattering power on Li is too small to gain enough information on local environment of Li^+ ions. On the other hand electrochemical method can only offer us macro statistical information. NMR is well suited to explore the local environment of Li^+ ions in structure. Garcia *et al* [13] studied the structure of low temperature crystallized $LiCoO_2$ by ^7Li MAS NMR. They found one single peak at −1 ppm for all samples associated to similar rotation bands, which are symmetrically observed around each NMR peak. They had the following conclusions:

a) The coordination of lithium is in the same position for all phases;
b) The chemical shift of -1 ppm characterizes a lithium atom in octahedral site;
c) The small chemical shift to the reference indicates no paramagnetic shift from impurity ions;
d) A slightly broader signal is observed at low temperatures indicating a larger structural disorder in the second coordination sphere of lithium.

Ouyang et al [14] studied $Li_{1-x}CoO_2$, obtained from $LiCoO_2$ with lithium electrochemically removed by NMR method and concluded:

a) The parent compound, $LiCoO_2$, is characterized by both a small chemical shift ~5ppm relative to aqueous LiCl solution, and a relatively narrow line width, 130 ppm full width at half maximum;
b) The lack of observable quadrupole satellite transitions, coupled with very low ionic mobility inferred from variable temperature studies, indicates that the Li site symmetry is high;

c) The large chemical shifts and increased line widths of the Li-deficient materials are attributed to localized spin on the Co sites;

d) Spin-lattice relaxation (T_1) measurements were made at various temperatures. The results indicate that the stoichiometric compound exhibits remarkably little variation over the large 350°C range. Spin lattice relaxation of Li deficient materials change by about a factor of four over the same temperature range.

In 1998 (after the related work described in this thesis was done), Peters et al [15] studied rock-salt type Li_xCoO_2 (x=0.48~1.05) by ^6Li, ^7Li and ^{59}Co MAS NMR. Their ^7Li MAS NMR spectra of Li_xCoO_2 -T_{400} samples (Low Temperature, 400°C) showed -0.9 ppm peak, characteristic of lithium in an octahedral coordination. A narrower resonance at the same position was observed in the ^7Li MAS NMR spectra of Li_xCoO_2 -T_{900} (High Temperature, 900°C) samples with a Li/Co ratio ≤ 0.95. $LixCoO_2$ -T_{900} samples with Li/Co ratio > 0.95 showed several new lithium features. They realized that the new features indicate the presence of a paramagnetic cobalt species in the materials. In ^{59}Co MAS NMR spectra, the resonance positions are attributed to Co^{3+} octahedrally coordinated by oxygen. With variable external field measurements performed at 14.1 and 7.05 T, no quadrupole shift indicates an undistorted octahedral coordination of cobalt in the materials studied. Electrochemical extraction of lithium leads to a low field shift of the lithium resonance of 60-120 ppm, depending on the amount of lithium removed. Electrochemical deintercalation of the samples results in the reappearance of the original lithium spectra. Partly charged samples give signals in the range of 120-60 ppm and a signal at –0.9 ppm characterize samples, indicating part of the lithium remains in an unchanged environment.

Many groups have reported extensive results of the studies on the electrochemical and chemical properties of lithium manganese spinels [16-19]. Kanzaki et al studied the mechanism of lithium ion insertion into λ-MnO_2 in 1991[20]. They reported the Knight shifts for sample Li_2MnO_3 and $LiMn_2O_4$, which are 0 and 50~60 kHz from aqueous LiCl NMR reference with a field strength of 6.3T. In early 50's, John [21] reported the Knight shift of metal lithium, which is about 28 kHz (268 ppm), using the same NMR reference.

Ouyang et al conducted a comparative study of spinel $LiMn_2O_4$ from several commercial sources and $LiMn_2O_4$ prepared by themselves. In their NMR results, both a very broad line and large shift from the reference LiCl position characterize the spectra. The results indicate that there is a large magnetic interaction between spins localized on the Mn^{4+}(and to a lesser extent Mn^{2+}) and the ^7Li nuclei. In this paper, investigation on chemical shifts vs. temperatures as well as on temperature vs. linewidth on $LiMn_2O_4$ samples from different sources are also described.

Ganguly et al [22] published their NMR results for Li-Ni-Co-O system. The results indicate that ^7Li NMR line is narrow in the nonmagnetic compounds containing only Co ions as in $LiCoO_2$ and $La_2Li_{0.5}Co_{0.5}O_4$. When Co^{3+} ions was replaced by Ni^{3+} ions, a large chemical shift was observed, for example, ~580 ppm in $LiNiO_2$. These results are in agreement, with those of Itoh et al [23] and Villeneuve et al [24]. The authors reasoned that the large shift is mainly due to a dipolar field, which is formed from the magnetic Ni site or the oxide ions if a hole on oxygen is also associated with a spin.

From the above NMR results we have the following conclusion: a paramagnetic shift signal was observed in the systems due to the existence of paramagnetic ions of various valence.

1-2. Anode materials

Several anode materials were investigated for improving the cycle life performance and safety of rechargeable lithium batteries. The requirements of anode materials for lithium ion batteries are: a large lithium capacity, a low voltage with respect to lithium, fast kinetics for lithium charge/discharge reactions, high reversibility, good electronic conductivity and chemical and thermal compatibility with the electrolyte. The lithium anode materials can be classified into three categories: 1) lithium alloys (Li, Li-Sn, Li-Sb and so on), 2) lithium intercalation compounds (for example Li-C), and 3) metal oxide compounds (Sn-O, Sb-O, Pb-O).

1-2.1. Carbonaceous materials

Carbon is one of the best materials for an alternative anode in lithium ion rechargeable battery [25]. Recently, a lot of carbon materials have been considered for this purpose. As anode materials, carbon has the mentioned advantages. To use lithium carbon compounds to replace metallic lithium anodes can improve safety in lithium batteries. Structure of carbon strongly depends on the processing temperature of the organic precursor. **Figure 1-4** shows the carbonization process with temperature. With a temperature range of lower than 300°C, the resulting carbon has an amorphous structure. When the temperature rises to the ranges of 300 – 500°C and 500 – 1000°C, the structure becomes more crystalline and the results are known as pitch and coke. Below about 1000°C, a significant amount of hydrogen remains in the structure. Natural graphite begins to form in the temperature range of 1000-2500°C. When the temperature is in as high as the range of 2500-3000°C, the resulting product is highly crystalline graphite,

which has the best ordered and layered 2-D structure. Some organic precursors can never yield the ordered graphite structure, even at high temperature. The resulting material is often called carbon.

The lithium ion intercalation and deintercalation are a key factor controlling the lithium specific capacity and the life length of cells. Carbons with different structure phases can have very different lithium ion intercalation and deintercalation. For carbon materials that have so many structural phases, to find the key structural properties that control their electrochemical performance is not an easy task. So far we have known carbon blacks show very poor lithium intercalation capacity, which is about 20-40mAh/g. Coke type carbons exhibit lithium intercalation capacity in the range of 140-180mAh/g. Graphitic carbons have reversible lithium capacity in the range of 250-350mAh/g. Many studies have been carried by the electrochemical method [26-28].

Many groups also have worked on this task by using solid state NMR. In 1995, Mori et al [29] published ^{7}Li NMR spectra and suggested that two types of lithium doping sites exist in the coke: one type (S-site) has a wide range of spinning side bands while the other (C-site) has a narrower range. It is believed that the C-site lithium atoms are located between the carbon sheets, while the S-site lithium atoms are on the surface of the microcrystallites formed by these sheets or at their microcavities. In the paper, a lithium doping/undoping process pattern (See **Figure 1-5**) was given to explain the mechanism of lithium charge and discharge.

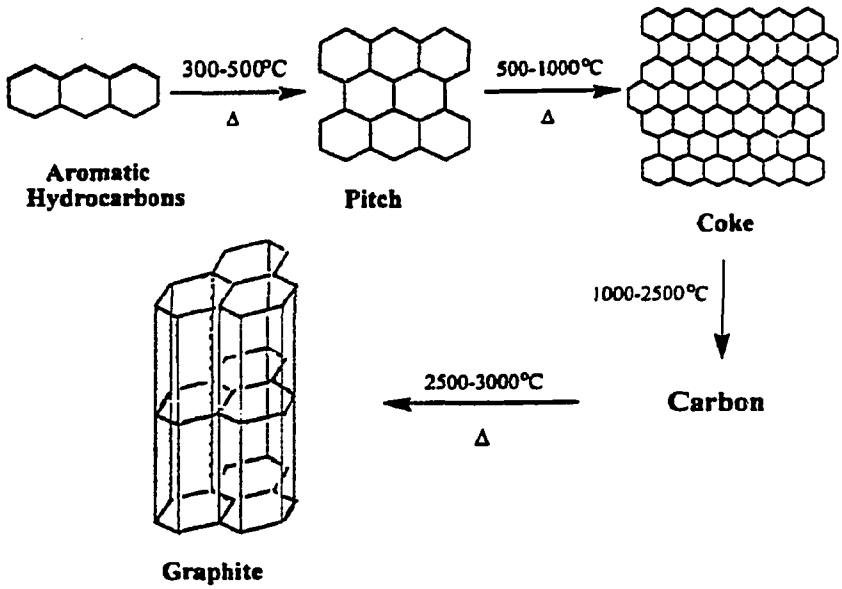

Figure 1-4: The schematic diagram of the carbonization process involved in the preparation of various carbon materials [30].

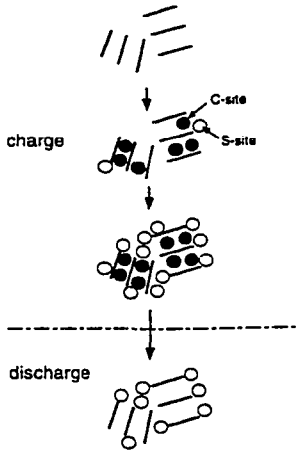

Figure 1-5: The schematic representation of supposed lithium doping /undoping process in disordered carbon [29].

In the case of mesocarbon microbeads (MCMBs) heat-treated above 2000°C [31], the fully lithiated MCMBs with the stacking order of graphite layers showed two sites by ^{7}Li NMR. One at 45 ppm is relative to the structure with the AB stacking order of graphite layers. The other at 27 ppm a turbostratic disordered structure with a random stacking sequence of graphite layers. Takami et al [32] constructed a model of lithium insertion into and extraction from disordered carbons. The model is displayed in **Figure 1-6.**

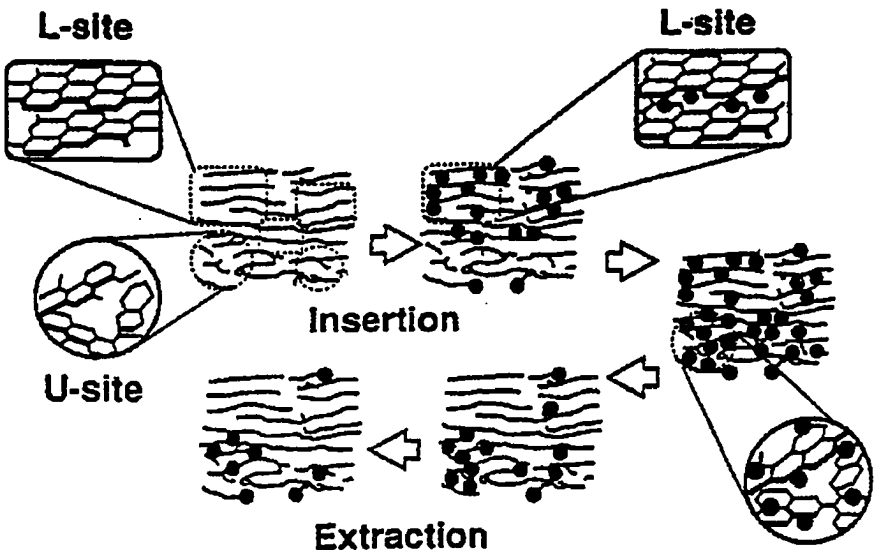

Figure 1-6: The schematic model of lithium insertion into and extraction from disordered carbon [32].

The ^{7}Li NMR results show that there are two rather small shifts of A and B (<10 ppm) with LiCl as reference. The authors assigned shift A to ionic lithium stored, not only in the L-site but also on the aromatic ring in the U-site, while band B is assigned to lithium trapped in the edge of the aromatic ring. The results supported the concept that a large amount of lithium ions stored on the aromatic rings as an ionic complex caused the high reversible capacity of disordered carbons containing hydrogen. Let's list the important ^{7}Li NMR results below:

1. Satoh et al, Toshiba Corp[33]:

Non -graphite carbon fiber

NGCF 900: 1 ppm at 100 mAh/g

	70.8 and 13.8 ppm	at 700 mAh/g
NGCF 1100:	3.6 ppm	at 100 mAh/g
	83.7 and 12.6 ppm	at 600 mAh/g
NGCF 1600:	9.8 ppm	at 100 mAh/g
	36.1 ppm	at 250 mAh/g

2. Takami et al [32]:

Mesophase-pitch-based carbon fiber (N4CF 900)

Sharp band at -1. 4 ppm	at 100 mAh/g
Sharp band at 16.9 ppm and broad band at its bottom	at 400 mAh/g
Sharp band at 20.9 ppm and broad band at its bottom	at 600 mAh/g

Perylene based disordered carbon (PBDC 550):

Sharp band at - 1. 5 7 ppm	at 100 mAh/h
Sharp band at -1.36 ppm and shoulder at 2.30 ppm	at 300 mAh/g
Sharp band at 0. 31 ppm and shoulder at 7.11 ppm	at 900 mAh/g

3. Nagai et al [34]:

Pseudo Isotropic Carbon (PIC 1200, cross-finked petroleum pitch, hard):

Sharp bands at 0 and at 11 ppm	at 186 mAh/g
Sharp bands at 0 and at 2 4 ppm	at 279 mAh/g
Sharp band at 0 ppm and broad band + shoulder at 47 ppm	at 3 72 mAh/g
Sharp band at 0 ppm and broad bands at 70 and 104 ppm	at 450 mAh/g

Sharp band at 0 ppm and broad bands at 80 and 110 ppm at 500 mAh/g

Sharp band at 0 ppm and broad band + shoulder at 110 ppm at 600 mAh/g

4. Mori et al [29]:

Pitch coke (C750):

Sharp band at 0 ppm and broad band at 23 ppm at 773 mAh/g

Sharp bands at 0 and at 55 ppm at 343 mAh/g (MAS)

Pitch coke (C1000):

Sharp band at 0 ppm and broad band at 20 ppm at 306 mAh/g

5. Sato et al[35] :

Poly(p-phenylene) based disordered carbon (PPP 700):

Sharp band at 0 ppm and broad at 9.16 ppm at 1000 mAh/g

1-2.2. Lithium -tin materials

Lithium –tin alloy usually has a high specific lithium capacity. However, with it being used as electrode, it has a major disadvantage that it is mechanical unstable during charge and discharge cycling. In 1994, Fuji Photo Film, in Japan, filed a patent for Li-ion cells containing an amorphous tin-based composite oxide anode [36]. Since then it has attracted researchers to study the potential of substituting tin oxides for carbon as anode materials in lithium ion batteries. The mechanism of lithium ion insertion into SnO electrode can be explained by the following reactions [37]:

$$2Li + SnO + 2e^- \rightarrow Sn + Li_2O \quad (1\text{-}1)$$

$$y\,Li^+ + Sn + ye^- \rightarrow Li_ySn \quad (1\text{-}2)$$

The starting SnO has an intermetallic phase or composites of several intermetallic phases (Sn_2Fe). During the electrochemical reaction with metal Lithium, Li-Sn alloys with

different ratios of Li/Sn can be obtained. The electrochemical reaction is (we take $Li_{4.4}Sn$ as an example):

Initial		Fully discharged		Charged again
$6.4Li + SnO$	$\rightarrow$	$Li_2O + Li_{4.4}Sn$	$\leftrightarrow$	$Li_2O + 4.4Li + Sn$

Dahn et al [37] found the structure of $Li_{4.4}Sn$ ($Li_{22}Sn_5$). Their results indicated the alloy has a BCC lattice, of cube of edge a with all the lithium and tin atoms are placed at the vertexes. The tin positions are in random groups oriented tetrahedra of Sn, having edges of length $(2a)^{1/2}$. The structure of $Li_{22}Sn_5$ is displayed in **Figure 1-7.**

Lithium Tin alloys usually have high specific capacity of lithium. But the major problem is the mechanical stability during charge-discharge cycling. The tin oxide anode material is somewhat more reversible. When lithium reacts with tin oxide anodes, tin metal, which is surrounded by Li_2O matrix, will be formed. Although the actual lithium insertion involves only the tin metal, the Li_2O phase can improve the mechanical stability of lithium alloy electrode.

1-3. Composite electrolyte

1-3.1. The mixture of Li and Al_2O_3

Polymer electrolytes have low ionic conductivity at room temperature and poor mechanical properties above 60°C. Inserting filler (Al_2O_3) into polymer solid electrolytes can enhance their mechanical and electrical properties. In 1973 it was discovered by C.C. Liang [38] that the conductivity of LiI salt can be increased by a factor of 50~100 at room

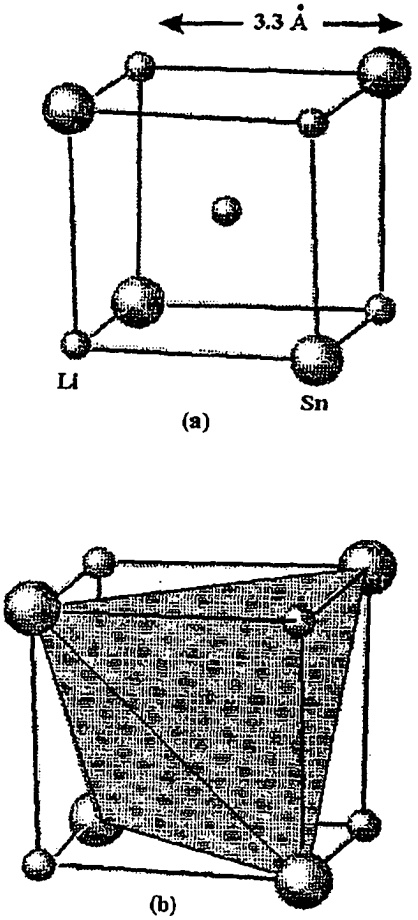

Figure 1-7: The structure of $Li_{22}Sn_5$. (a) A BCC unit of the structure which has four tin atoms. (b) Showing how the four tin atoms in (a) are on the corners of a tetrahedron. [37].

temperature in LiI +40% Al_2O_3 system. Observations of the enhancement of lithium salts ionic conductivity up to three orders of magnitude by adding inorganic oxides such as Al_2O_3 have been reported [38-43]. This effect is of significant interest scientifically because the conductivity enhancement mechanism involves surface level interaction between the lithium salt and oxide particles. Conductivity enhancement is also technologically important because of the need to develop new solid ionic conductors. More recently, the addition of inorganic oxides to polymer electrolytes has also been investigated, and significant improvement in electrical properties has been reported. Dupree et al [43] studied the mixture of LiI with γAl_2O_3 by ^7Li NMR methods. With a mixture of LiI with 30m/o γAl_2O_3 sample, two relaxation rates are found which show the heterogeneous nature of the material. From the relative amplitude of these rates, the authors found that about 50% of the lithium are in a radically different environment from that in pure LiI. They concluded that the increasing conductivity observed in composite materials such as this is associated with this different environment. In 1980, Wang et al [44] studied LiCl with Al_2O_3 (α,β,γ) by solid state NMR. The spectra of ^7Li NMR show that a narrow peak overlaps with a broad peak. The explanation of the conductivity mechanism was given based on their NMR results.

1-3.2. PEO-LiI complexes

Composite polymer electrolytes consisting of poly (ethylene oxide) (PEO), a lithium salt and an inorganic oxide with nanoscale inorganic powders such as Al_2O_3, TiO_2 and MgO have received considerable attention, especially for higher than ambient temperature (80-120°C) applications [45,46]. Recently, many attempts have been made to

improve the electrical or mechanical properties by adding other components to the basic PEO-Li salt complex, including plasticizers and inorganic oxides. Previous work has demonstrated beneficial effects of high surface area inorganic ceramic additives to polymer electrolytes, such as enhanced dimensional stability, reduced crystallinity and improved stability toward lithium [47-49]. In highly salt-concentrated PEO complexes, the presence of the inorganic additive also has been implicated in improvement of interfacial ion transport through grain boundaries parallel to the current flow in the electrolyte [50]. In 1997, Wong et al [51] used solid state NMR to study a nanocomposite polymer electrolyte. They did variable temperature measurements of ^{7}Li line widths. The observation of linewidth narrowing at interlayer cation site suggests that the cation dynamics in the nanocomposite polymer electrolytes can be probed. And the timescale differs from the dynamics associated with segmental motion of the polymer. The cation environment in the vicinity of Li^{+} differs substantially from that found in solid polymer electrolytes and for the larger cation in the nanocomposite. In the paper, authors provided a sensitive test on the existing theories of polymer electrolyte conductance.

1-4. Solid electrolyte interface (SEI)

Lithium metal is an attractive anode material for rechargeable cells because of its high specific capacity 502(Wh/Kg) and high oxidation potential. However, due to its high oxidation potential, it is difficult to find thermodynamically stable electrolyte systems for lithium metal. A portion of solvent reacts with lithium metal anode to form a surface layer that is called the solid electrolyte interface (SEI). The formation of SEI, while necessary to prevent further solvent Li reaction and provide an ionically conductive

medium between the anode and electrolyte, also has several disadvantages: 1) the surface films formed on lithium anode often insulate a portion of the electrode and make it inaccessible for electrochemical reaction. 2) The deposition of lithium occurs non-uniformly, especially on the film covered electrode, leading to the formation of lithium dendrites. Such lithium dendrites can penetrate through the separator, causing internal shorts. The cycle life and reliability of Li-metal rechargeable cells are greatly decreased by the dendritic Li deposition [52-55]. To overcome the weaknesses of lithium metal as anode and for safety concerns, researchers have worked on alternative anode materials.

Chapter 2. Theoretical Background of NMR

2-1. Basic phenomenon and theory of NMR

Since Bloch et al. and Purcell et al [56,57] first separately observed Nuclear Magnetic Resonance (NMR) phenomenon in 1946, both NMR theory and NMR technology have had great development. Integrated theoretical and experimental systems have been built up. To explain NMR, two approaches have been used: quantum and classical treatments. The quantum treatment is characterized by the spin quantum number I and the magnetic quantum number m, while the classical treatment mainly benefits to us by providing a vivid physical picture. The following discussion starts with the quantum treatment approach.

Generally speaking [58,59], all nuclei possess the property of spin. The spin angular momentum is denoted as $\hbar\mathbf{I}$, where $\hbar$ is Planck's constant h divided by 2π, and I is nuclei spin. According to the principles of quantum mechanics, the magnetic moment μ of a nucleus with spin **I** is proportional to the magnitude of the spin:

$$\mu = \gamma\hbar\mathbf{I} \tag{2-1}$$

where γ is the gyromagnetic ratio of the nucleus. In the presence of a static applied magnetic field $\mathbf{H_o}$, the magnetic moment μ will interact with $\mathbf{H_o}$. The Hamiltonian of Zeeman interaction is given by:

$$H_{Zeeman} = -\mu\cdot\mathbf{H_o}. \tag{2-2}$$

Taking the field $\mathbf{H_o}$ along the Z-direction of the laboratory coordinate, the Hamiltonian can be rewritten as:

$$H_{Zeeman} = -\gamma\hbar|\mathbf{H_o}|I_z = -\hbar\omega_o I_z, \tag{2-3}$$

where $\omega_o = \gamma|\mathbf{H_o}|$, and I_z is the z-component of **I**. The energy states thus can be characterized by the magnetic number m:

$$E_m = -\hbar\,\omega_o\,m \qquad m = |\mathbf{I}|, |\mathbf{I}|-1, \ldots\ldots, -|\mathbf{I}| \tag{2-4}$$

The separation between two adjacent energy levels is

$$\Delta_{Em,m-1} = \hbar\,\omega_o\,. \tag{2-5}$$

Figure 2-1 illustrates a schematic diagram of Zeeman energy levels of spin-1/2 and spin-3/2.

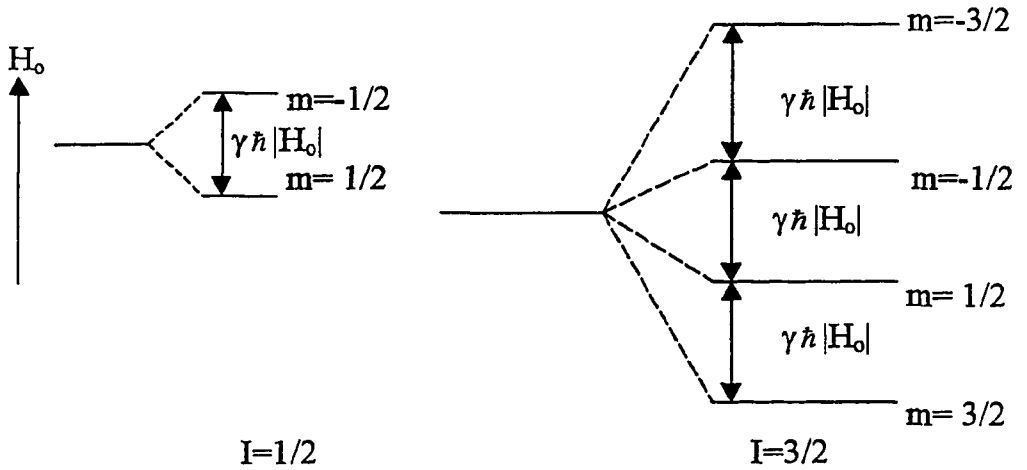

Figure 2-1: Zeeman energy levels for spin-1/2 and spin-3/2 cases.

The transition between two nuclear spin levels can be induced by applying a small sinusoidal radio-frequency (rf) magnetic field H_1 ($|\mathbf{H_1}| << |\mathbf{H_o}|$) of frequency ω perpendicular to the applied static field. The Hamiltonian for this interaction includes two terms:

$$H = -\gamma \hbar \mathbf{I} \cdot \mathbf{H_o} - \gamma \hbar \mathbf{I} \cdot \mathbf{H_1} \tag{2-6a}$$

When taking the field $\mathbf{H_o}$ along the Z-direction and $\mathbf{H_1}$ along the X-direction, one has:

$$\begin{aligned} H &= -\gamma \hbar |\mathbf{H_o}| I_z - \gamma \hbar I_x (2|\mathbf{H_1}| \cos\omega t) \\ &= -\hbar \omega_o I_z - 2\hbar \omega_1 I_x \cos\omega t \end{aligned} \tag{2-6b}$$

where $\omega_o = \gamma|\mathbf{H_o}|$, $\omega_1 = \gamma|\mathbf{H_1}|$.

If $|\mathbf{H_1}|$ is so small that time dependent perturbation theory applies, then the transition rate is:

$$P_{mm'} = \gamma^2 |\mathbf{H_1}|^2 |\langle m|I_x|m'\rangle|^2 \delta(\nu_{mm'} - \nu) \tag{2-7}$$

where

$$\nu_{mm'} = \frac{\Delta E_{mm'}}{h} = \frac{\gamma |\mathbf{H_o}| |m - m'|}{2\pi} \tag{2-8}$$

Therefore, the following conclusions can be obtained:

(a) The transition rate is proportional to γ^2 and the amplitude of sinusoidal rf field $\mathbf{H_1}$.

(b) $\mathbf{H_1}$ must be perpendicular to $\mathbf{H_o}$. Otherwise, no transition occurs due to condition $\langle m|I_x|m'\rangle = \gamma \hbar \delta_{mm'}$.

(c) $|m - m'| = 1$ and $2\pi\nu_{mm'} = \gamma |\mathbf{H}_o|$ are the conditions that have to be fulled in order to induce transitions. The second condition can be rewritten as the well-known resonance condition:

$$\omega_o = \gamma|\mathbf{H}_o|,$$

where ω_o is called the Larmor frequency.

Discussed above is so-called the quantum mechanical treatment and next the classical macroscopic treatment of NMR is introduced. The latter may be more helpful for us to visualize NMR by giving a vivid physical picture.

For a system with many molecular magnetic moments, a vector called macroscopic magnetization **M** is defined as

$$\mathbf{M} = \Sigma \mu_i \tag{2-9}$$

It is the sum of all the individual nuclear or molecular magnetic moments per unit volume. When a static magnetic field **H** is applied, **M** undergoes precession about the direction of **H**. The motion of **M** in the external field **H** is described by

$$\frac{d\mathbf{M}}{dt} = \gamma\, \mathbf{M}\times\mathbf{H}. \tag{2-10}$$

The equation can be easily solved in a frame (x', y', z') rotating with frequency ω with respect to the laboratory frame (X, Y, Z). The transformed equation is

$$(\frac{d\mathbf{M}}{dt})_{rot} = (\frac{d\mathbf{M}}{dt})_{lab} - \omega \times \mathbf{M} = \gamma\, \mathbf{M} \times \mathbf{H} - \omega \times \mathbf{M} = \gamma\, \mathbf{M} \times (\mathbf{H} + \frac{\omega}{\gamma}). \tag{2-11}$$

Taking a static field $\mathbf{H}_o$ along the Z-direction and an rf field $\mathbf{H}_1$ along the X-direction, in the vector form, the **H** is written as:

$$\mathbf{H} = (\mathbf{H}_o)_Z + 2(\mathbf{H}_1)_X \cos\omega t. \tag{2-12}$$

$\mathbf{H}_1 = (2|\mathbf{H}_1|\cos\omega t, 0)$ can be decomposed into two counter-rotating vectors $\mathbf{H}_L + \mathbf{H}_R = (|\mathbf{H}_1|\cos\omega t, -|\mathbf{H}_1|\sin\omega t) + (|\mathbf{H}_1|\cos\omega t, |\mathbf{H}_1|\sin\omega t)$. If the direction of z' in rotating frame (x', y', z') coincides with the Z-direction in the laboratory frame, then in the rotating frame, $\mathbf{H}_L$ is static with amplitude of $\mathbf{H}_1$, while $\mathbf{H}_R$ is rotating at 2ω which can be ignored. Equation (2-11) becomes as:

$$(\frac{d\mathbf{M}}{dt})_{rot} = \gamma\mathbf{M} \times [(|\mathbf{H}_o| + \frac{\omega}{\gamma})\mathbf{e}_{z'} + |\mathbf{H}_1|\mathbf{e}_{x'}] = \mathbf{M} \times \gamma\mathbf{H}_{eff} \qquad (2\text{-}13)$$

where $\mathbf{H}_{eff} = (|\mathbf{H}_o| + \frac{\omega}{\gamma})\mathbf{e}_{z'} + |\mathbf{H}_1|\mathbf{e}_{x'}$.

When $\omega = -\gamma|\mathbf{H}_o|$, $\mathbf{H}_{eff} = |\mathbf{H}_1|\mathbf{e}_{x'}$, i.e. a static field aligned on x' axis and **M** will precess about the x'-axis with frequency $\gamma|\mathbf{H}_1|$. This makes **M** tip in longitudinal direction. The tipping angle θ of **M** is given by

$$\theta = \gamma|\mathbf{H}_1|t_p, \qquad (2\text{-}14)$$

where t_p is the duration of $\mathbf{H}_1$, which can be such that makes the magnetization **M** tips in angle 90°, as illustrated in **Figure 2-2**, which corresponds the **M** vector being rotated from the vertical direction into the horizontal plane. After this 90° pulse, **M** will decay in time as the system comes back to equilibrium due to some mechanisms. The magnetization dephases in the x'-y' plane because the field inhomogeneity, but it also tends to regrow along z' direction as it approaches thermal equilibrium.

When the spin system is placed into an rf-coil, a small voltage is induced in the coil. This induced voltage is a measure of the component of a magnetization **M** in the horizontal plan after the rf pulse. The induced voltage decays due to spin-spin interaction and inhomogeneity of the static field $\mathbf{H}_o$. It is called the Free Induction Decay (FID),

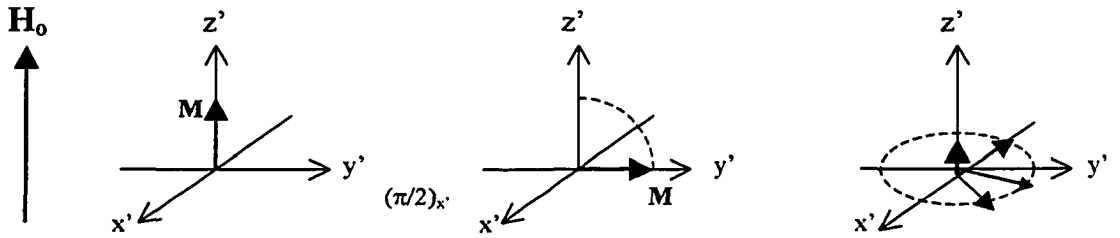

Figure 2-2 : Effect of rf pulse on magnetization.

referring to the absence of the field $\mathbf{H_1}$. With Fourier Transform (FT), the FID is converted from time domain $f(t)$ to frequency domain to obtain the absorption spectrum F(ω) or F(ν).

Assume a FID signal $f(t)$ is an exponential decay function:

$$f(t) = A_0 e^{-\frac{t}{T_2^*}} \tag{2-15}$$

where T_2^* is a characteristic time constant. The spectral lineshape is its Fourier transform. Fourier transform is done in terms of the equation:

$$F(\omega(= \int_{-\infty}^{\infty} f(t) e^{-i\omega t}\, dt = v - iu \tag{2-16}$$

where

$$v = \frac{A_0 T_2^*}{1 + \omega^2 T_2^{*2}} \qquad u = \frac{A_0 T_2^{*2} \omega}{1 + \omega^2 T_2^{*2}} \tag{2-17}$$

The real part ν is termed the absorption spectrum and the imaginary part u is the dispersion spectrum. The magnitude spectrum is

$$M = \sqrt{v^2 + u^2} \tag{2-18}$$

The linewidth $\Delta\nu$ for a Lorentzian absorption spectrum ν is expressed as

$$\Delta\nu = \frac{1}{\pi T_2^*}. \tag{2-19}$$

Figure 2-3 shows a typical free induction decay and its Fourier transform spectrum.

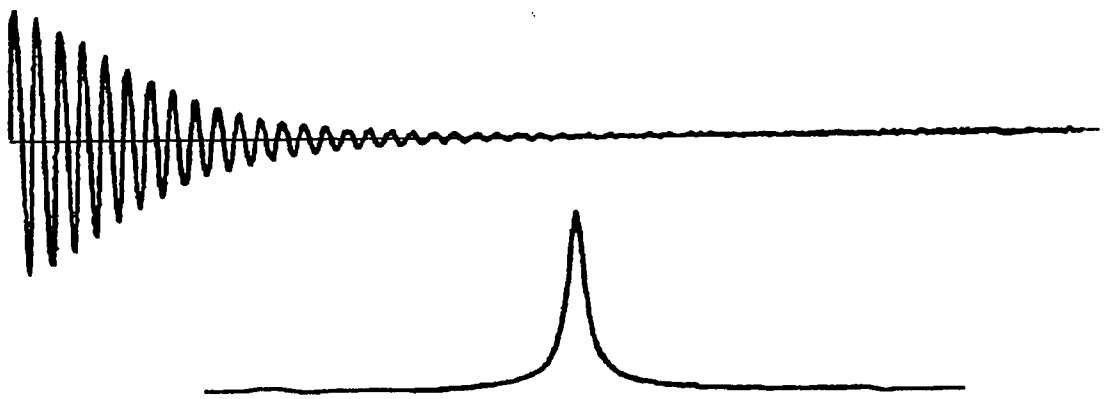

Figure 2-3: A FID and its spectrum. Top: FID. Bottom: The spectrum.

2-2. Relaxation

After being disturbed by an rf pulse to an excited state, the system tends to return to the equilibrium by releasing its extra energy. This process is called relaxation. It is well known that a spin in a higher energy state can make a transition to a lower energy state via spontaneous emission or stimulated emission. The probability of spontaneous emission at radio frequency is too small to be significant (the probability of spontaneous emission is $A_{spon} \propto \omega^3_{kk'}$). Thus, all NMR transitions are considered to be via stimulated emissions. In order to realize a stimulated emission, there must exist some interaction between nuclear spin and the surroundings, or "lattice", to transfer the excess energy from the spin system to the "lattice". Two kinds of interaction are considered affecting NMR relaxation:

(1) Interaction between a time varying magnetic field and nuclear magnetic dipole moments.

(2) Interaction between a time varying electric field gradient (EFG) and the electric quadrupole moment of the nucleus for nuclei with spin>1/2.

Since the nuclear spin-lattice relaxation process depends on the existence of molecular motion to generate a randomly fluctuating magnetic field or EFG, valuable information about the motion can be retrieved from relaxation measurements.

Now consider the spins as an isolated system from the thermodynamic point of view. Incident radiation in the form of an rf pulse transfers "heat" to the spins and raises their "spin temperature". The relaxation process then transfers "heat" to the lattice that acts as a reservoir and thus restores the system to thermal equilibrium. The spin-lattice relaxation time, called T_1, is a measurement on the rate of transferring energy from the spin to the lattice. The spin-spin relaxation T_2 time is a measurement of the time for

which the energy is redistributed within the spin system. The spin-lattice relaxation time T_1 characterizes the rate of recovery of the Z-axis component (M_z) of the total magnetization towards its equilibrium value ($\mathbf{M_o}$) along $\mathbf{H_o}$, while the spin-spin relaxation time T_2 characterizes the rate of the loss of phase coherence of a spin system.

Bloch proposed from phenomenological arguments that the disturbed magnetization **M** returns to its equilibrium value exponentially in time. Assuming $\mathbf{H_o} = |\mathbf{H_o}|\mathbf{e_z} + |\mathbf{H_1}|\mathbf{e_x}$ and $\mathbf{M_o} = M_x\mathbf{e_x} + M_y\mathbf{e_y} + M_z\mathbf{e_z}$, the Bloch equation (2-10) was rewritten in the following form in the laboratory frame.

$$\frac{dM_x}{dt} = \gamma(\mathbf{M}\times\mathbf{H_o})_x - \frac{M_x}{T_2}, \tag{2-20}$$

$$\frac{dM_y}{dt} = \gamma(\mathbf{M}\times\mathbf{H_o})_y - \frac{M_y}{T_2} \tag{2-21}$$

$$\frac{dM_z}{dt} = \gamma(\mathbf{M}\times\mathbf{H_o})_z - \frac{M_z - M_x}{T_1}, \tag{2-22}$$

The solution of Bloch equation in the rotating frame can be found in Reference [58]. **Figure 2-4** is a vector diagram describing the process of spin-spin and spin-lattice relaxation, in z' direction and x'y' plane, respectively. From the equations (2-20,21,22) one can see that spin-lattice relaxation is related to recovery of M_z which is parallel to $\mathbf{H_o}$, and spin-spin relaxation is associated with the variation of the components of **M** perpendicular to $\mathbf{H_o}$.

There are many processes through which the spin system may relax. The interactions resulting in a relaxation process will be discussed in the following section.

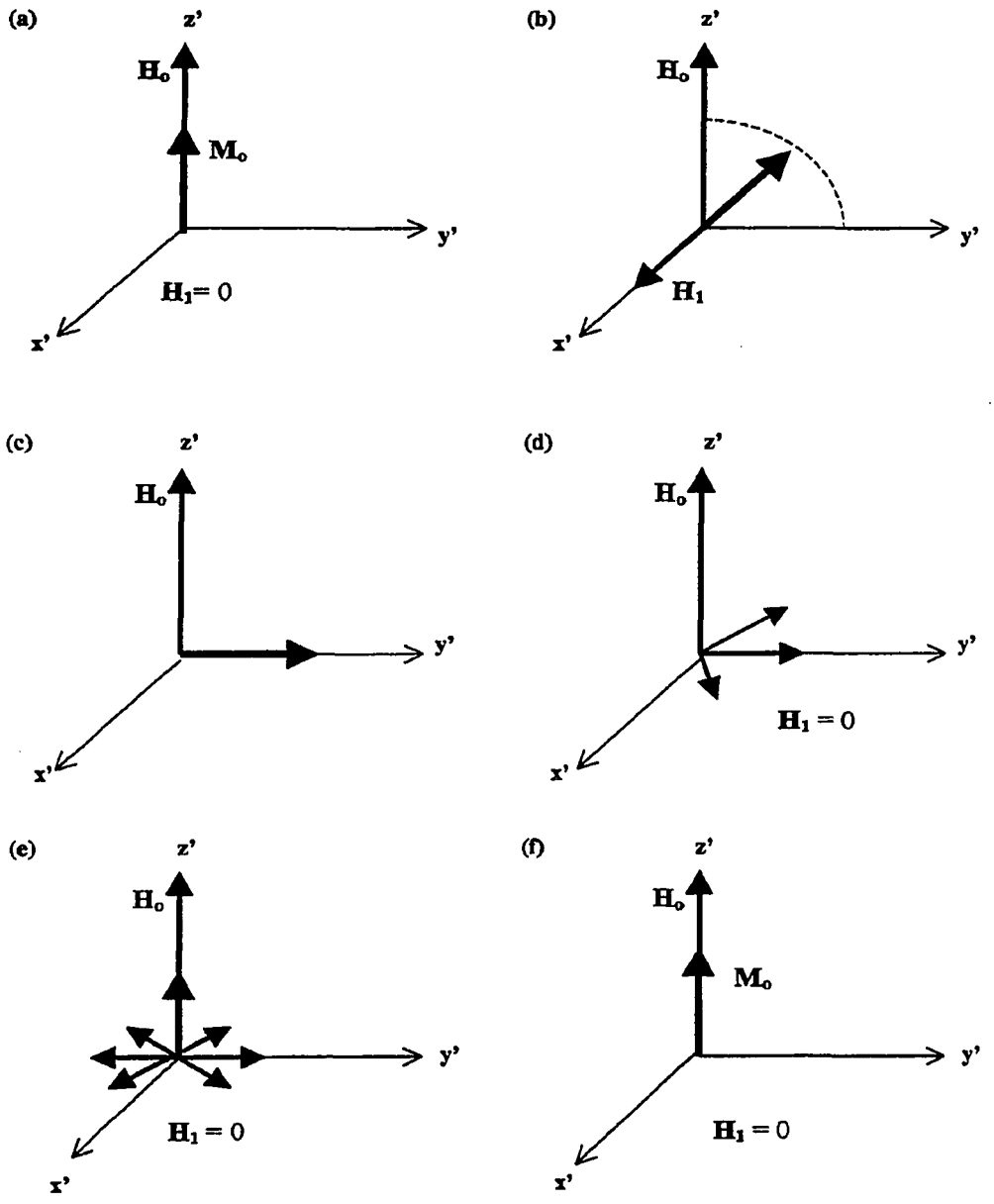

Figure 2-4: Rotating frame diagrams describing for relaxation (a) The net magnetization $\mathbf{M_o}$ is aligned along the magnetic field direction; (b) and (c) An rf pulse $\mathbf{H_1}$ is applied perpendicular to $\mathbf{H_o}$. The duration of H1 is sufficient to tip the net magnetization by 90°. (d) And (e) The spins begin to relax in the x-y plane by spin-spin (T_2) processes and in z' direction by spin-lattice (T_1) processes; (f) the equilibrium magnetization is reestablished along $\mathbf{H_o}$.

2-3. NMR interactions in solids

Understanding the various complicated interactions in solids is one of important tasks when using NMR techniques. **Figure 2-5** illustratively gives us a basic understanding about NMR interactions in solids. The more we understand these interactions, the better we can clearly extract information from the data.

Although there are many kinds of interactions, here we only concentrate on the interactions of primary importance in solids, such as Zeeman interaction, dipole-dipole interaction and quadrupolar interaction. A more complete discussion about interactions can be read in some classic NMR books [58,59].

In terms of quantum mechanism, the interaction between the nucleus and its environment is represented by the Hamiltonian of the nucleus. **Figure 2-5**, shows that the Hamiltonian contains, in general case, several terms including:

(1) Zeeman interaction H_{Zeeman} with applied static field $\mathbf{H}_o$;

(2) nuclear electrical qudrupole interaction $H_{quadrupole}$;

(3) dipole-dipole interaction between nuclear spins $H_{dipole\text{-}dipole}$;

(4) chemical shift caused by shielding electrons around nucleus $H_{chemical\text{-}shift}$ and so on. The total Hamiltonian of the nucleus, which is used to describe the interactions with its environment, is written by

$$H = H_{Zeeman} + H_{quadrupole} + H_{dipole\text{-}dipole} + H_{chemical\text{-}shift} + \text{"Other"} \qquad (2\text{-}23)$$

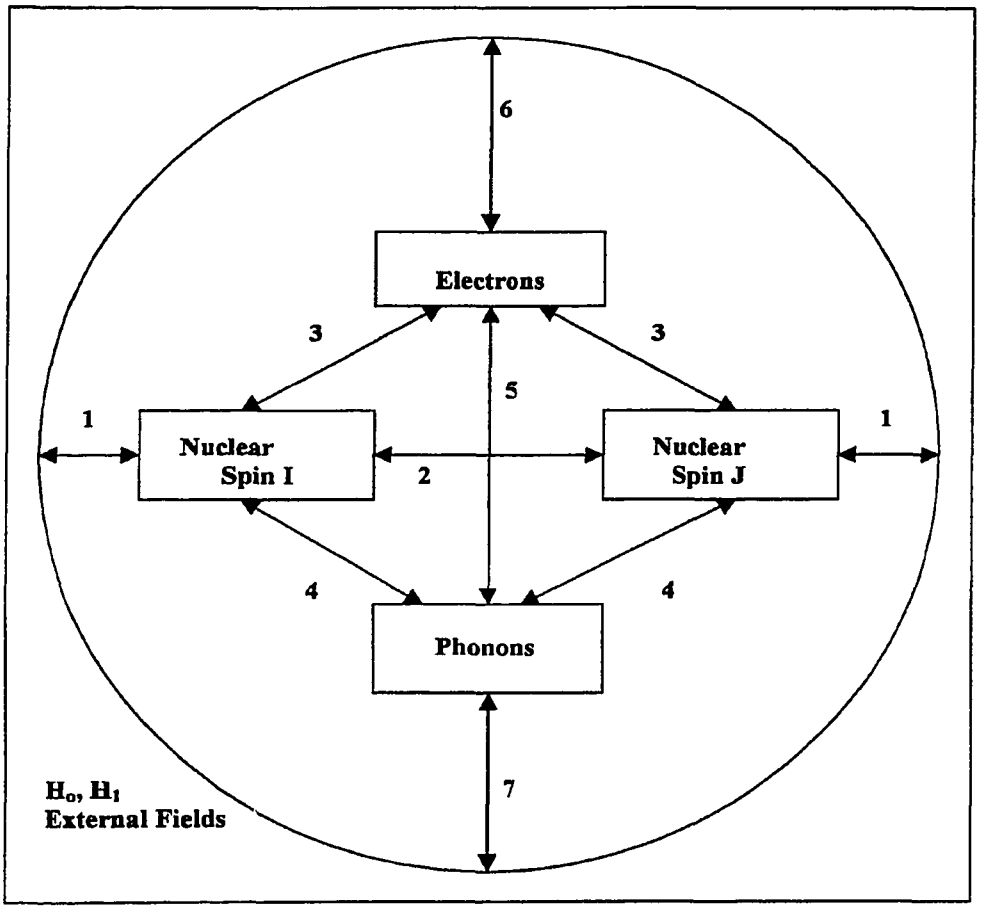

Figure 2-5: The seven-fold way a nuclear spin can interact with its surrounding. (1) Zeeman interaction of spins. (2) Direct spin interaction. (3) Nuclear spin-electron interaction and indirect spin interaction. (4) Direct spin-lattice interaction. (5) Indirect spin lattice interaction via electrons. (6) Shielding and polarization of nuclear spins by electrons. (7) Coupling of nuclear spins to acoustic field etc[60].

where "Other" represents terms such as scalar J or indirect coupling of the nuclear spins, the spin-rotation interaction and coupling of nuclear spin to acoustic field etc., which will not be covered in the thesis.

2-3.1. Zeeman interaction

The Zeeman term, which is an interaction between a nucleus with non-zero spin **I** and static external magnetic field $\mathbf{H_o}$, has been discussed previously. According to equation $H=\hbar\omega$, the magnitude of the Hamiltonian can be expressed in the unit of frequency ω which is the ratio of H to $\hbar$. For example, Zeeman frequency for Lithium nuclear (I=3/2) is about 116 MHz and 300MHz for proton (I=1/2) in a static magnetic field of 7 Tesla.

2-3.2. Dipole-Dipole interaction

The direct dipole interaction refers to the coupling of the resonant nucleus with the field produced by the magnetic dipoles of neighboring nuclei. The dipole contribution to the Hamiltonian of a pair of nuclear spins is given by

$$H_{dipole\text{-}dipole}=\frac{\mu_1\cdot\mu_2}{r^3}-\frac{3(\mu_1\cdot r)(\mu_2\cdot r)}{r^5} \qquad (2\text{-}24)$$

where r is the radial vector from μ_1 to μ_2, $\mu_1=\gamma\hbar\mathbf{I}_1$ and $\mu_2=\gamma\hbar\mathbf{I}_2$ as shown in **Figure 2- 6.**

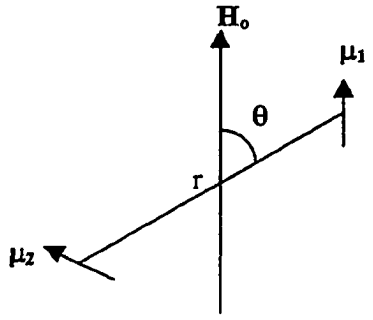

Figure 2-6: Formation of the dipolar interaction of two spins.

In the spherical coordinate system (with $\mathbf{H_o}$ in the Z direction) the dipolar interaction term can be written by:

$$H_{dipole\text{-}dipole}=\frac{\gamma_1\gamma_2\hbar^2}{r^3}(A+B+C+D+E+F), \qquad (2\text{-}25)$$

where

$$A = I_{1z}I_{2z}(1\text{-}3\cos^2\theta)$$

$$B = -\frac{1}{4}(I_1^+I_2^- + I_1^-I_2^+)(1\text{-}3\cos^2\theta)$$

$$C = -\frac{3}{2}(I_1^+I_{2z} + I_{1z}I_2^+)\sin\theta\cos\theta e^{-i\phi}$$

$$D = -\frac{3}{2}(I_1^-I_{2z} + I_{1z}I_2^-)\sin\theta\cos\theta\, e^{-i\phi}$$

$$E= -\frac{3}{4} I_1^- I_2^- \sin^2\theta\, e^{-i\phi}$$

$$F= -\frac{3}{4} I_1^- I_2^- \sin^2\theta\, e^{-i\phi}$$

The frequency shift due to the dipole interaction can be estimated by the factor of $\gamma_1\gamma_2\hbar/r^3$. For a pair of lithium-7 nuclei separated by 4 Å , the frequency shift is about

$$\nu_{7Li}= \gamma_{7Li}^2\hbar/r^3 = (1.0398\times 10^4)^2 \times (1.05\text{x}10^{-27})/(4\times 10^{-8})^3 = 1.8 \text{ kHz}.$$

For a pair of protons separated by about 2 Å , the shift is about 95 kHz.

Compared to the Zeeman interaction, the contribution from dipole interaction term to the total Hamiltonian is very small. One, therefore, treats it with first-order perturbation theory. Only A and B terms are used to calculate the effect of $H_{dipole\text{-}dipole}$ on the eigenstates of H_{Zeeman}. They will vanish under Magic Angle Spinning (MAS) because they are both proportional to the factor of $(1 - 3\cos^2\theta)$. The terms C, D, E, and F are off-diagonal; they introduce slight admixtures of the zero-order states into the exact states and can usually be ignored.

It is necessary to consider a special situation in which internuclear lines of dipole pairs are isotropically oriented in all directions without motion. The line broadening thus observed is referred to as the powder pattern. This will be discussed further for the case of the quadrupole interaction.

2-3.3. Quadrupole interaction

Nuclei with spin I >1/2 have an electric quadrupole moment. The interaction between the electric quadrupole moment of a nucleus and the Electric Field Gradient (EFG) produced by surrounding electrons is called the quadrupole interaction. By studying the interaction one can obtain much more information about the local environment of the resonant nuclei. It indeed is considered a very useful tool to probe shorting-range environment of the nucleus. The following review is on the quadrupole interaction theory [61,62].

Considering a nuclear charge density $\rho(\mathbf{r})$ and a potential arising $V(\mathbf{r})$ from all charges except from the nucleus, the classical electrostatic interaction can be written as:

$$\mathbf{E} = \int \rho(\mathbf{r})\mathbf{V}(\mathbf{r})\mathbf{dV} \tag{2-26}$$

The potential V(r) can be expanded by the Taylor theorem:

$$V(x,y,z) = V_0 + \sum_i \left(\frac{\partial V}{\partial x_i}\right)_{r=0} x_i + \frac{1}{2}\sum_{i,j}\left(\frac{\partial^2 V}{\partial x_i \partial x_j}\right)_{r=0} x_i x_j + \ldots \quad , \tag{2-27}$$

where x_i denotes the Cartesian components of the coordinate system. Substituting equation(2-27) into Equation (2-26),one has

$$E = V_o \int \rho(r)dv + \sum_i V_i \int x_i \rho(r)dV + \frac{1}{2}\sum_{ij} V_{ij} \int x_i x_j \rho(r)dv + \ldots. \tag{2-28}$$

where $V_i = \left(\frac{\partial V}{\partial x_i}\right)_{r=0}$, and $V_{i,j} = \left(\frac{\partial^2 V}{\partial x_i \partial x_j}\right)_{r=0}$.

In Equation(2-28), the first term is identified as the electrostatic potential energy of nuclear charge. The second integral is the electric dipole moment of the nucleus. It vanishes for all nuclei in their ground states because these states have definite parity. The third term is called the electric quadrupole moment while V_{ij} is a component of the Electric Field Gradient (EFG) tensor at the nucleus. The new quantity Qij is defined

$$Q_{ij} = \int (3x_i x_j - \delta_{ij} r^2)\rho(\mathbf{r})dv \tag{2-29}$$

In terms of the Q_{ij}, one has the quadrupole energy $E_{quadrupole}$

$$E_{quadrupole} = \frac{1}{6}\sum_{i,j} V_{ij}Q_{ij} \tag{2-30}$$

The Hamiltonian of the quadrupole interaction in quantum mechanical form is expressed as:

$$H_{Quadrupole} = \frac{eQ}{6I(2I-1)}\sum_{ij} V_{ij}\left[\frac{3}{2}(I_iI_j + I_jI_i) - \delta_{ij}I^2\right] \tag{2-31}$$

By selecting the coordinate system of XYZ as the principal axes of the symmetrical tensor Vij so that $V_{xy} = V_{xz} = V_{yz}=0$, and considering the condition $|V_{xx}| \leq |V_{yy}| \leq |V_{zz}|$. , $H_{Quadrupole}$ is reduced to a simpler form:

$$H_{Quadrupole} = \frac{e^2qQ}{4I(2I-1)}\left[3I_z^2 - I^2 + \eta(I_x^2 - I_y^2)\right] \tag{2-32}$$

where eq= V_{zz} which is the largest component of EFG and η is called asymmetry parameter defined as

$$\eta = \frac{V_{xx} - V_{yy}}{V_{zz}} \tag{2-33}$$

Applying the magnetic field $\mathbf{H_o}$ along the Z axis of the laboratory frame, the angles θ and ϕ between the principal axis coordinate (x,y,z) and laboratory frame(X,Y,Z) are shown in **Figure 2-7.**

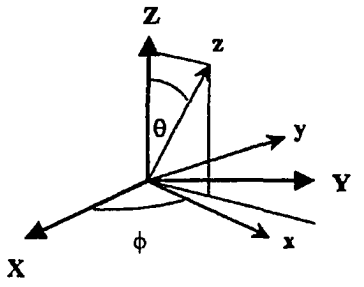

Figure2-7: The orientation of the principal-axis frame of EFG(x,y,z) relative to laboratory frame(X,Y,Z). The V_{zz} component of EFG tensor is aligned the z-axis.

Assuming an electric field gradient with axial symmetry (I_x=I_y or η=0) and under the principal coordinate system of the EFG tensor relative to $\mathbf{H_o}$, $H_{Quadrupole}$ can be written as

$$H_{quadrupole} = \frac{e^2qQ}{4I(2I-1)}\left[3I_z^2\cos^2\theta + 3I_x^2\sin^2\theta + 3(I_zI_x + I_xI_z)\sin\theta\cos\theta - I^2\right] \tag{2-34}$$

In a high magnetic field, the quadrupole Hamiltonian can be treated as a perturbation of the Zeeman Hamiltonian. The energy shift of Zeeman energy level up to the first order perturbation is

$$E_m = \frac{e^2qQ}{8I(2I-1)}(3\cos^2\theta - 1)\left[3m^2 - I(I+1)\right] \qquad (2\text{-}35)$$

In the case of asymmetric field gradient $\eta \neq 0$, the first order energy shift has the following form:

$$E_m = \frac{e^2qQ}{8I(2I-1)}(3\cos^2\theta - 1 + \eta\sin^2\theta\cos 2\phi)\left[3m^2 - I(I+1)\right] \qquad (2\text{-}36)$$

It also can be rewritten in the first order frequency shift form for the $m \rightarrow m\text{-}1$ NMR transition,

$$\omega^{(1)}_{m\leftrightarrow m-1} = -\frac{\omega_Q}{4}\left[(3\cos^2\theta - 1) - \eta\sin^2\theta\cos 2\phi\right](2m-1) \qquad (2\text{-}37)$$

where $\omega_Q = \frac{3e^2qQ}{2I\hbar(2I-1)}$.

In the case of the second order perturbation, the frequency shift of the central transition $1/2 \leftrightarrow -1/2$ is:

$$\omega^{(2)}_{1/2\leftrightarrow -1/2} = \frac{\omega_Q^2}{16\omega_L}\left[I(I+1) - \frac{3}{4}\right](9\cos^2\theta - 1)(1 - \cos^2\theta) \qquad (2\text{-}38)$$

From equations (2-37) and (2-38), one arrives at the following the conclusions:

(1) For a given orientation in a single crystal, 2 x I discrete resonance lines are observed. For example, for nuclear ^{7}Li with spin I=3/2, three discrete resonance lines are observed. The transitions adjacent to the central one are called satellite lines.

(2) $\omega_{m\leftrightarrow m-1}$ equals zero for m = ½. Thus, the frequency of the central transition 1/2 → -1/2 has no shift in the first order by quadrupole interaction.

(3) When EFG is small enough, the first order satellite splitting may be observed. As the quadrupole interaction increases, there can also be a shift and a splitting of the central line.

(4) Since the second order frequency shift is inversely proportional to the applied field ($\omega^{2}_{1/2\leftrightarrow -1/2} \propto 1/\omega_L$), one can observe the second order quadrupole effect by the varying of the applied static field.

In fact, the integrity of a crystal is not perfect. The nuclei in the sample encounter the different EFG from nucleus to nucleus. There may be a distribution of splittings. In the first order effect, the central transition has no frequency shift and is only dipolar broadened. In second order, the central resonance is strongly broadened asymmetrically. When the quadrupole interaction is strong enough, the satellites and eventually the central transition can be broadened beyond detection.

In a polycrystalline powder or amorphous sample, since structural units assume random orientations with respect to the static applied magnetic field, the NMR response

is continuously distributed over a range of frequencies, called the powder pattern. The line shape of this powder pattern is calculated by [61]

$$S(\nu)d\nu = \frac{1}{4\pi}\sum_{m}\int_{d\nu}^{\nu+d\nu} I_m d(\cos\theta)d\phi \qquad (2\text{-}39)$$

where the I_m is the transition probability from state i to state j. The integration is over those elements with solid angle $d(\cos\theta)d\phi$ such that the resonance frequency falls between ν and $\nu+d\nu$. **Figure 2-8** shows Quadrupole splitting of the magnetic resonance of a nucleus for spin =3/2 e.g. ^{7}Li, ^{23}Na.

2-3.4. Electron Interaction

The presence of the static applied magnetic field inevitably changes the distribution of electronic current, which arises from the orbital motion of valence and conduction electrons, which in turn changes the magnetic field experienced by the nuclei (either shielding or deshielding). This causes a change in the resonance frequency of the nucleus. It is called the chemical shift effect. For paramagnetic and diamagnetic systems, shifts of the spectral line relative to that of the free nucleus are in opposite directions. The chemical shift Hamiltonian can be written as:

$$H_{\text{Chemical shift}} = \gamma \hbar \, \mathbf{I} \cdot \sigma \cdot \mathbf{H_o} \qquad (2\text{-}40)$$

where σ is the chemical shift tensor. In the principal axis coordinate system, the first order shift in Zeeman frequency is:

$$\Delta\nu_{\text{Chemical Shift}} = -\nu_{\text{Zeeman}}[\sigma_{\text{isotropic}} + \sigma_{\text{anisotropic}}(3\cos^2\theta - 1) + \sigma_{\text{axial}}\sin^2\theta\cos 2\phi] \qquad (2\text{-}41)$$

where

$$\sigma_{iso} = \frac{1}{3}(\sigma_1 + \sigma_2 + \sigma_3)$$

$$\sigma_{aniso} = \frac{1}{6}(2\sigma_3 - \sigma_{12} + \sigma_2)$$

$$\sigma_{axial} = \frac{1}{2}(\sigma_2 - \sigma_1)$$

where σ_1 , σ_2 ,σ_2 are the principle components of the chemical shift tensor σ. From equation (2-41), one can see that the average over all orientations removes the anisotropic and axial terms from the $\Delta\nu_{Chemical\text{-}Shift}$.

For example, in a liquid sample, due to the fast tumbling of the molecules, the average over all orientations leads to the observation of angularly independent term σ_{iso}, called the isotropic chemical shift.

In a metal sample, there exists a similar effect which is named after Walter Knight, who first observed the phenomenon in metallic copper. Further studies revealed that the phenomenon is common to all metallic samples. The shift is from the interaction between the nucleus and spins associated with conduction electrons. The quantitative theoretical expression for the shift is written as[50]:

$$\frac{\Delta H}{H_o} = \frac{8\pi}{3}\left\langle |u_k(0)|^2 \right\rangle_{E_F} \chi_e^s \qquad (2\text{-}42)$$

where ΔH is the shift of nuclear resonance signal, $\mathbf{H_o}$ is the static applied field, $\left\langle |u_k(0)|^2 \right\rangle_{E_F}$ gives the density of electrons near the Fermi level. χ_e^s is the magnetic susceptibility. From the equation, the following conclusions can be found:

(1) ΔH is positive with respect to the diamagnetic reference.

(2) The fractional shift $\Delta H/Ho$ is independent of ω_o.

(3) The fractional shift is almost independent of temperature because $\left\langle |u_k(0)|^2 \right\rangle_{E_F}$ and χ_e^s are both nearly independent of the temperature.

(4) The fractional shift increases in general with increasing nuclear charge.

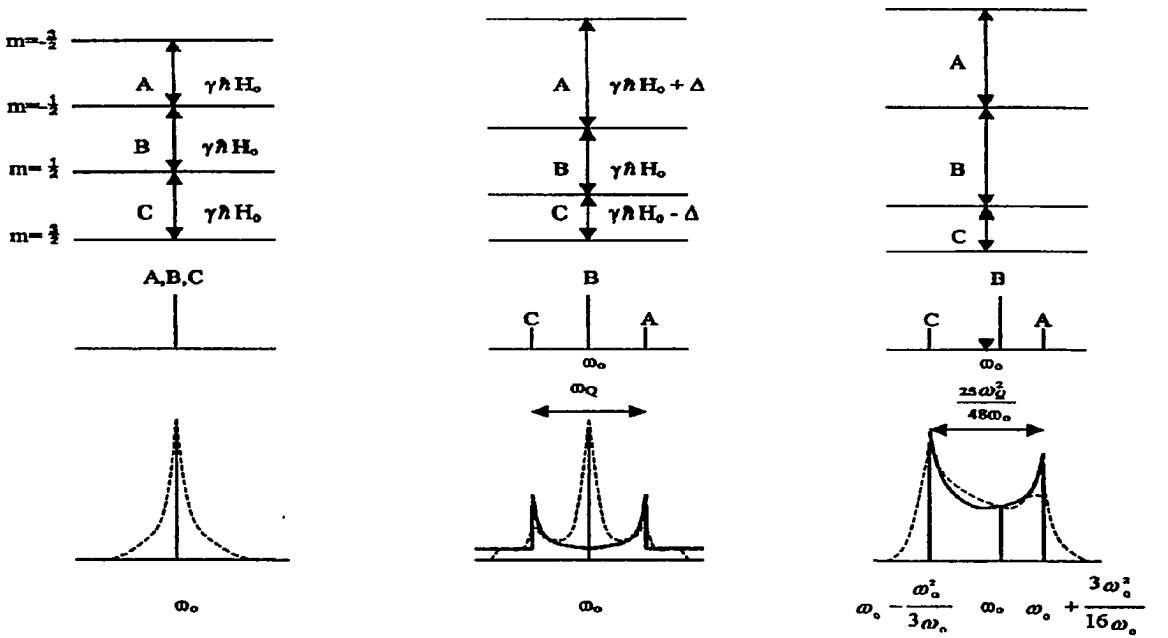

$$\omega_0 = \gamma H_0 \qquad \omega_Q = \frac{e^2 qQ}{2\hbar} \qquad \Delta = \frac{\omega_q (3\cos^2\theta - 1)}{2}$$

Figure 2-8: Quadrupole splitting of the magnetic resonance of a nucleus of spin 3/2. Left: no quadrupole interaction. Center: first order splitting of satellite. Right: second order shifting of the central component. Top: energy spectrum. Middle; spectrum of a single nucleus without dipolar broadening. Bottom: spectrum of a powered sample with axially symmetric field gradient. With the dipolar broadening superimposed , the dotted curves result.

Chapter 3. Research Methods

3-1. Solid state NMR techniques[64]

For static NMR measurements, samples were packed into either 5 or 10mm diameter sample tubes. **Figure 3-1** is the sample's packing scheme of MAS. Typical radio frequency pulse lengths were from 2μs to 5μs. However, a shorter pulse length might be required to cover a suitable range of frequency for the broad resonance spectra.

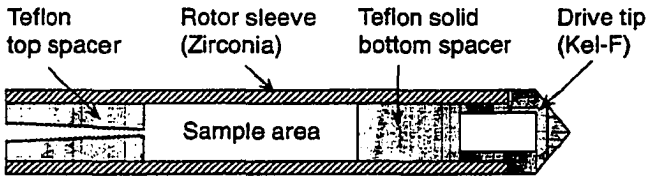

Figure 3-1: The sample packing scheme in MAS experiment

3-1.1. Single pulse and echo pulse sequences

Single pulse and echo pulse sequences are the two typical pulse sequences used to get time-domain signals from samples. They are described as below:

1. Single pulse sequence

The single pulse sequence is the simplest and most often used method to measure the NMR spectrum of a sample. The 90° pulse rotates the magnetization **M** by 90° to align it on the x'-y' plane. When the spin system dephases inside a radio frequency (RF) – coil (after the pulse is turned off), a voltage is induced in the coil. The induced voltage

is a measurement of the **M** in the horizontal plane (x'-y'), which is called FID because it decays after the pulse due to spin-spin interaction as well as inhomogeneity of the static field $\mathbf{H_0}$. The FID signal is collected in time domain. In **Figure 3-2,** a typical single pulse sequence is illustrated.

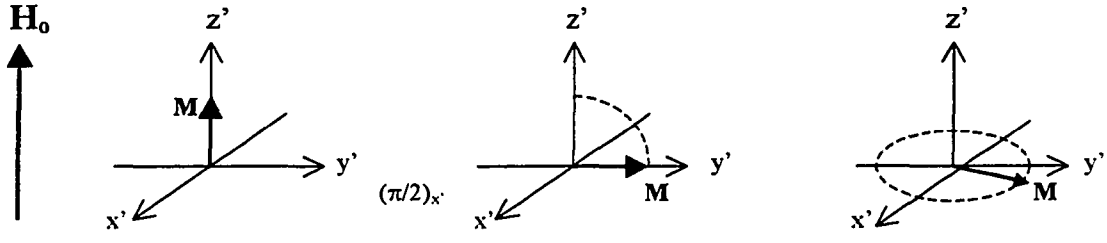

Figure 3-2: The classical picture of single pulse

2. Echo pulse sequences

In solid state NMR experiments, there is a unique problem called "dead time" of the spectrometer. The "dead time" indicates the time needed for the spectrometer to recover from the burst of the high power RF pulse. FID acquisition can only be started after the "dead time" following the pulses. A major source of the "dead time" is the magneto acoustic ringing of coil after pulse. The ringing is stronger at low frequencies than at high frequencies. The "dead time" can be a serious problem for solid state NMR because most solids have broad NMR lines and short spin - spin relaxation time which means their FIDs are weak and short. Signals submerged in the "dead time" can be a

significant portion of the FID for a solid. To overcome the problem, echo techniques, invented by Hahn [65], are commonly utilized.

a. Spin echo pulse sequence

A classical picture of spin echo is illustrated in **Figure 3-3**. The magnetization **M** lies along the Z-axis initially, parallel to the static external magnetic field $\mathbf{H_o}$. Suppose a 90° pulse is applied along x' at time t=0 and is denoted as $90°_{x'}$. This $90°_{x'}$ pulse flips **M** by 90° to lie along the y'-axis. Since nuclear spins in a macroscopic sample might have different local environment and therefore experience different local fields, they precess at different rates. As a result, the different contributions to the magnetization will get out of phase with each other. The contribution to the magnetization that arises from one such small local segment of the sample, experiencing a homogeneous applied field, is called a spin isochromat. The spin isochromats will shortly thereafter dephase in the x'-y' plane. When t equals τ, a $180°_{x'}$ pulse is applied to the partially dephased spin system. The part of **M**, which has been recovered due to spin - lattice relaxation to lie back along the z–axis, would be then rotated 180° to the -z direction. In most solid state NMR experiments, this is only a very small fraction of the total **M** (i.e. $T_2 << T_1$). Of **M** remaining in x'-y' plane each one of the spin isochromats would be rotated 180° about the x' axis. Therefore, following the 180° pulse, the spin isochromats begin to rephase to form a net magnetization as the rapid isochromats catch up with the slow ones. The result is that the magnetization becomes refocused along the -y' axis at time 2τ. The spin echo process is then completed. The echo actually consists of two FIDs back-to-back and the second half of the echo is processed as the FID signal from a single pulse. One of the benefits of

using the echo pulse is that the "dead time" problem is overcome by using a suitable τ to move the FID signal away from the region of the "dead time". The second benefit is that the spin-spin relaxation time, T_2 can be measured directly.

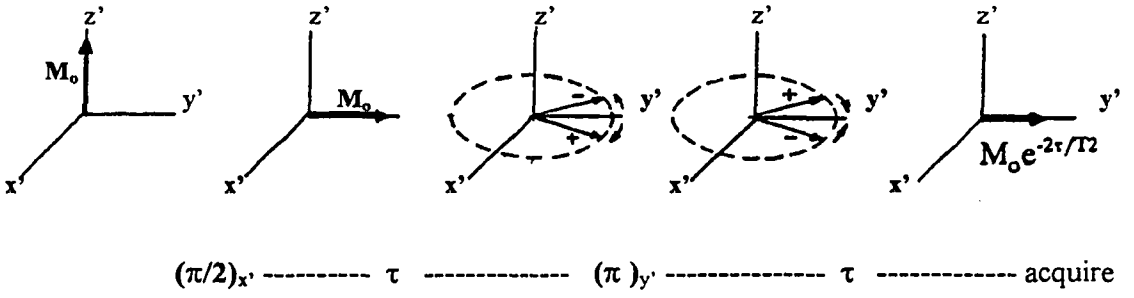

Figure 3-3: The classical picture of spin echo.

b. Solid echo pulse sequence

A quadrupole echo pulse sequence (solid echo pulse sequence) is used when the main source of line broadening is the quadrupole interaction. Due to the similarity between the first order quadrupole and magnetic dipole Hamiltonian terms, the same sequence is also effective for strongly dipolar coupled systems. The quadrupole pulse sequence can generate a refocused signal. An example of quadrupole pulse sequence is $90°_{x'}$ - τ - $90°_{y'}$ - τ - echo. The general form of such a pulse sequence can be written as $90°_{x'}$ - τ - $\beta°_{\phi'}$ - τ - echo. Unfortunately, there is no classical picture to describe the process. The explicit equation for a very simple case of I=1[66] can be derived by density matrix methods, which is written as:

$$S(t) = \sin^2\beta\cos[\, a(t-\tau)\,]\,(1-e^{-i2\phi}) \qquad (3\text{-}1)$$

where S(t) is the complex amplitude of a FID, β is the second pulse rotation angle and ϕ is the phase angle relative to the z' - axis for the second pulse.

From the above equation, we can see the maximum S(t) occurs when $t=2\tau$, the second pulse $\beta=90°$ and shift $\phi = 90°$. This can be verified by experiment.

3-1.2. Pulse sequences for T_1 measurements

In order to determine the spin-lattice relaxation time (T_1) for a spin system, the spin system is first disturbed into a non-equilibrium state and then its recovery process is measured. It can be done with at least two basic methods, inversion-recovery and saturation-recovery.

1. Inversion-recovery method

The pulse sequence of inversion-recovery is shown in **Figure 3-4**. For a spin system initially at equilibrium ($M_z = M_o$), the first 180° pulse is used to rotate the magnetization such that $M_z(t=0) = - M_o$. Then at a time τ, a 90° pulse is applied to generate a FID. $M(\tau)$ can be expressed as:

$$M(\tau) = M_o\,(1 - 2e^{-\tau/T_1}) \qquad (3\text{-}2)$$

where T_1 is the spin-lattice relaxation time. After the measurement of the FID, it is necessary to wait a time long enough for the $M(\tau)$ to relax back to its thermal equilibrium value M_o. The waiting time is usually taken as $5T_1$. Then the same echo pulse procedure is applied again with a different τ to get another FID. The FIDs are the signal averaged until adequate signal-to-noise ratio is obtained. One repeats the above procedure for

different values of τ to get a set of $M(\tau)$. The spin relaxation time T_1 can then be calculated by fitting to the above equation.

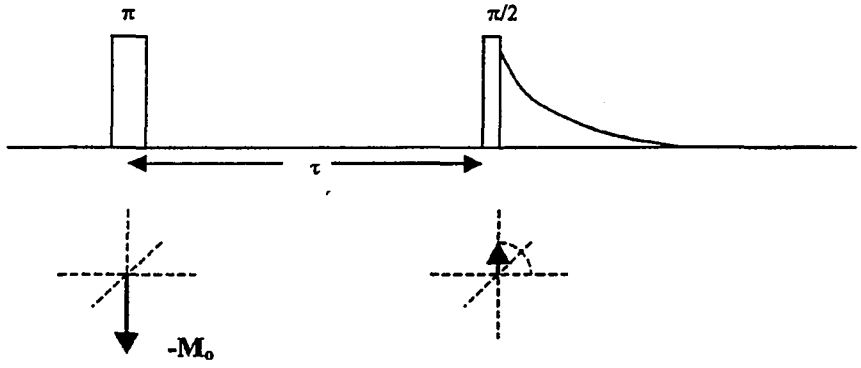

Figure 3-4: Inversion recovery sequence to determine T_1.

2. Saturation recovery method

The saturation recovery pulse sequence is shown in **Figure 3-5**. The magnetization is saturated by "comb" of 90° pulses and after a waiting period τ another 90° pulse is applied to generate a FID. The $\mathbf{M}(\tau)$ is expressed by the following equation:

$$\mathbf{M}(\tau) = M_0(1 - e^{-\tau/T_1}) \qquad (3\text{-}3)$$

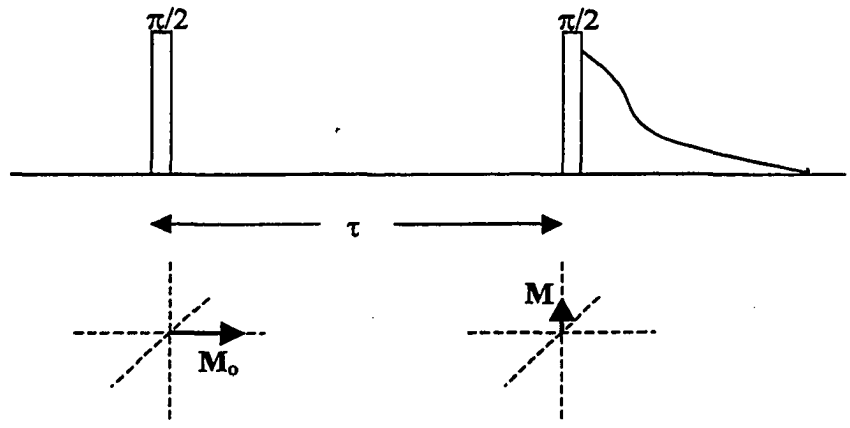

Figure 3-5: Saturation recovery sequence to determine T_1.

3-1.3 High resolution NMR techniques

3-1.3.1. Magic Angle Spinning (MAS) technique

In order to improve resolution of NMR spectrum, a famous technique called "Magic Angle Spinning"(MAS) is commonly used. The so-called magic angle is 54.74°. The method is quite simple: to spin a sample, at a frequency of several kHz, about z-axis at 54.74° with respect to the magnetic field $\mathbf{H_o}$, see **Figure 3-6**. At this magic angle θ=54.74°, the chemical shift anisotropy, which has an angular dependence of $(3\cos^2\theta - 1)$ can be averaged to zero. Also at this magic angle θ =54.74°, the magnetic dipole-dipole coupling between two spins and the first order quadrupole interaction, both of which have an angle factor $(3\cos^2\theta - 1)$ that is usually called the anisotropic orientation factor and causes an inhomogeneous broadening of the spectra, can be reduced. **Figure 3-7** shows a typical MAS spectrum.

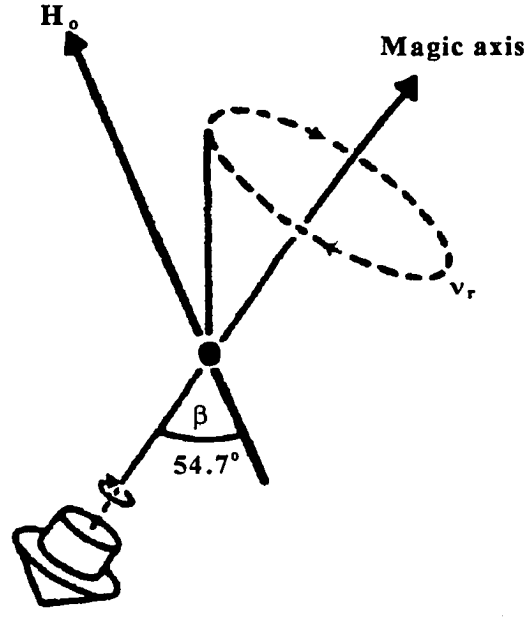

Figure 3-6: Diagram illustrating the geometry of the MAS experiment when a solid is rotated with frequency ν_r about an axis inclined at magic angle β=54.74° to $\mathbf{H_o}$.

In a MAS spectrum, there are spinning sidebands at the multiples of the spinning rate on both sides of the true resonance line. From the sideband separation, the spinning rate can be easily identified. For effectively reducing the line broadening, the spinning rate should be comparable to the linewidth for the static spectrum of the sample.

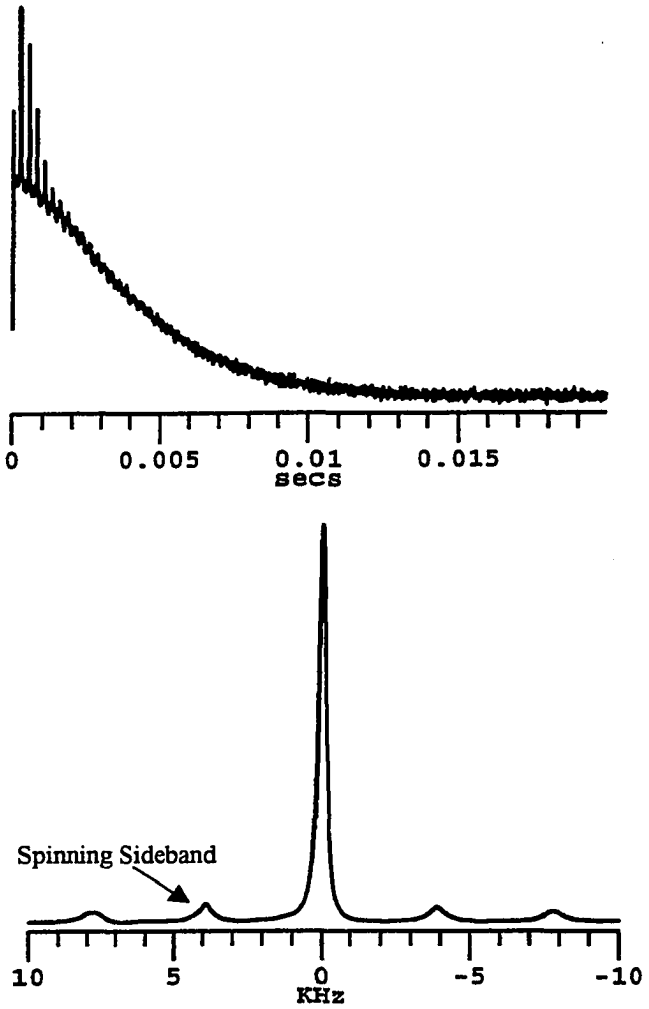

Figure 3-7: A typical MAS spectrum. Top: FID. Bottom: The spectrum.

3-1.3.2. Double - resonance techniques

Double-resonance techniques are very useful to obtain high resolution spectra in heteronuclear systems. For example, the heteronuclear dipole interaction can be studied by the high power decoupling technique that is a typical double resonance technique (DRT). In our experiments, two typical DRTs are used. One is Decoupling Technique (DT), the other is called Cross Polarization technique (CP).

Let's take an example to first introduce the DT technique. We have a ^{13}C and ^{1}H solid system. The pulse sequence of DT is illustrated in **Figure 3-8**.

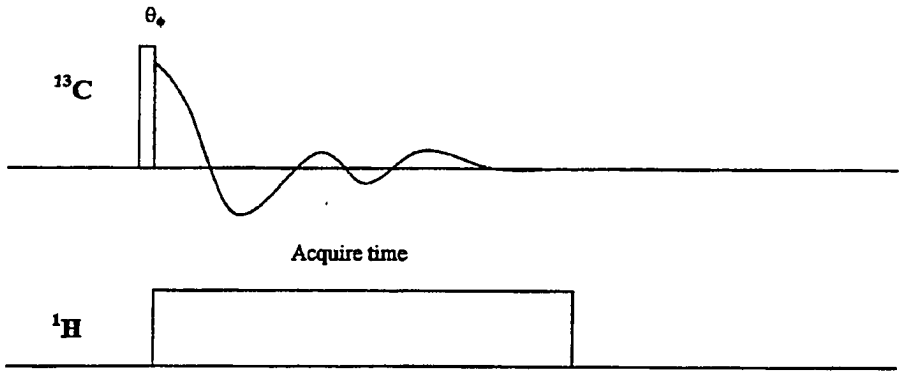

Figure 3-8: Decoupling pulse sequence.

In H channel, a longer pulse whose length equals the acquisition time in X channel is sent into a sample. X channel is reserved to acquired ^{13}C signal, and the H channel is

used to remove the effect of ^{1}H. The DT technique is a very useful tool to get relatively narrow spectrum.

To discuss CP, we also use as an example, the ^{13}C and ^{1}H sample system being used. ^{13}C is a relatively insensitive nucleus due to its low isotopic abundance. CP can make ^{13}C sensitive by taking advantage of dipolar reservoir of an abundant nucleus ^{1}H in the same system, to transfer magnetization from ^{1}H to ^{13}C. The sensitivity of ^{13}C signal is enhanced by cross-polarization from proton provided that the Hartmann-Hahn matching condition $\gamma_H H_{1H} = \gamma_C H_{1C}$ is satisfied, where H_{1C}, H_{1H} denote the RF field of carbon and proton resonance respectively. **Figure 3-9** illustrates the basic pulse sequence of CP.

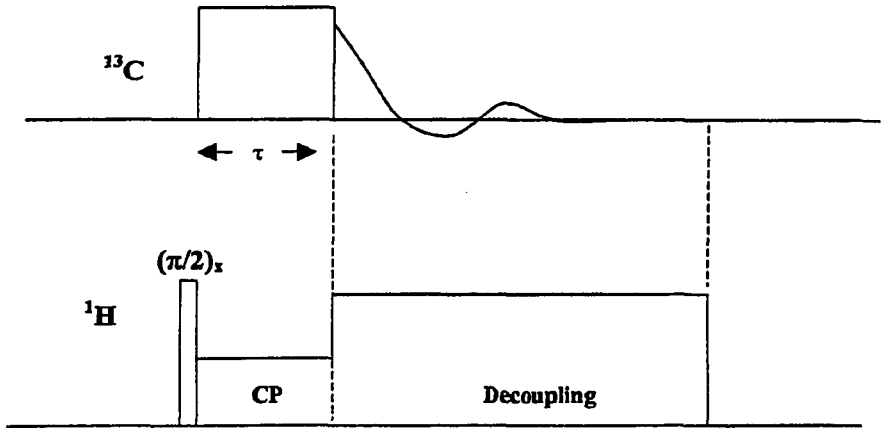

Figure 3-9: CP pulse sequence.

The CP technique can be used to get high resolution ^{13}C spectrum. It can also be employed to study the neighbor interaction between ^{13}C and ^{1}H. The important benefit of using CP is that the sensitivity enhancement allows the observation of spectra that often can not be obtained by single resonance methods.

3-2. Experimental equipment

3-2.1. NMR spectrometer[58]

All the measurements were conducted with a Chemagnetics CMX-300 spectrometer with double resonance channels. The CMX-300 spectrometer is an advanced system for performing modern NMR experiments on solid samples. Its six key components are described briefly below:

3-2.1.1. Two resonance channels

CMX-300 spectrometer can conduct double resonance experiments. There are two separate rf channels with separate high power amplifiers(model CE - 300ps for H-channel and ENI type for X-channel). The maximum power of the H-channel's high frequency power amplifier is up to 1kW in maximum. Its frequency range is from 282 MHz to 310MHz. The power of the low frequency power amplifier of the X-channel is 1.5kW in maximum output. Its frequency range is from 10MHz to 125MHz. The receiver has 360° phase range and its frequency range is 185-205MHz and <10-100MHz for H channel and X channel, respectively. The receiver bandwidth of both channels is more than 2MHz. The main parameters of the pulse program for both channels are 100MHz (Master Clock), 10 nsec (Resolution), 100 nsec (Minimum Interval Time), and 6553.6 sec

(Maximum Interval Time). Each channel contains two digitally controlled adjustable RF synthesizers. The transmitters are capable of fine phase resolution (1.4°), fast frequency switching over 2 MHz. Its phase range and frequency range are the same as the receiver.

3-2.1.2. Magnet

A JMT NMR superconducting magnet system with field strength 7 Tesla superconducting magnet produces the static field H_o. The homogeneity of H_o is determined by the linewidth for a liquid sample (D_2O), which is about 0.095 ppm when the resonance frequency is 46MHz and 5mm coil is used and is about 0.15 ppm when 10mm coil is used.

3-2.1.3. Solid temperature controller

The solid temperature controller can control the temperature range from -200 °C to 300°C during the NMR experiments. But one has to beware that the probe we used can only endure temperature range from -150 °C to 250 °C.

The controller uses a microprocessor to regulate temperature with accuracy (±0.2°C). It actually controls the temperature of gas (N_2, Air) which flows around the samples.

3-2.1.4. MAS speed controller

The MAS Speed Controller monitors and controls the spinning speed (Max. 7 kHz) of rotors used in solid state NMR MAS probes.

3-2.1.5. Probes

The Chemagnetics commercial probes are employed in the experiments. MAS probe is used in double resonance experiment with spinning. The tuning system is shown in **Figure 3-10.** Both MATCH and TUNE with the right combination of capacitors (C_b, Cf) for special nuclei are adjustable. The range of magic angle adjustment is from +5° to -5°. The 7.5mm rotors made of Zirconia are used in MAS experiments. The limitation of rotor spinning speed is up to 7 kHz. The MAS probe has a working temperature range from -150° to +250°C.

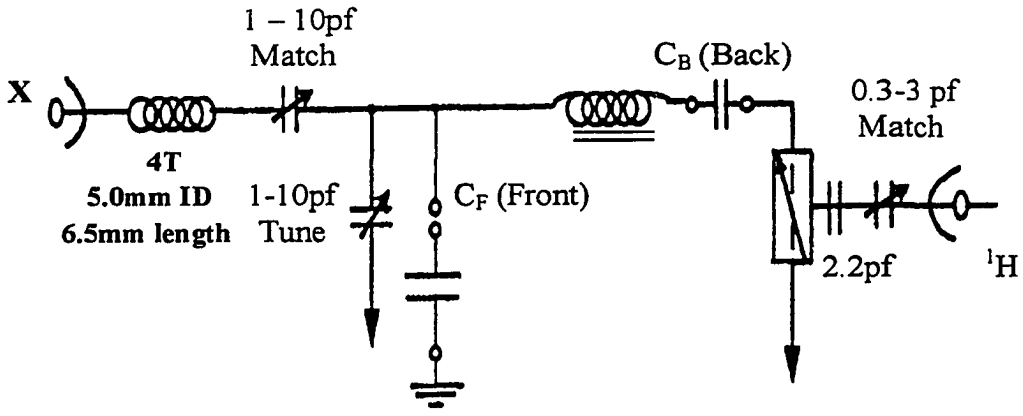

Figure 3-10: Schematic diagram of matching network for MAS probe.

The static wide-line probe (SRNS -2242) is used in the X-channel experiment. The circuit schematic of tuning is shown in **Figure 3-11.** Both MATCH and TUNE with different plug-in coil for different nuclei are adjusted to tune the probe.

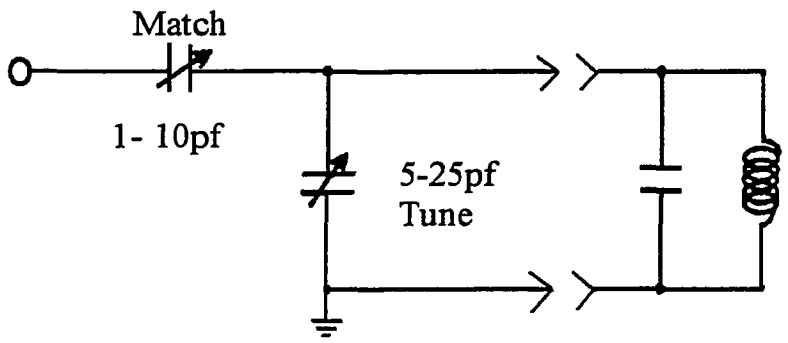

Figure 3-11: Schematic diagram of matching network for static probe.

3-2.1.6. Spectrometer Control Program

The Sun workstation (SPARC-2) is used to control the spectrometer. Programs CMXW and SPINSIGHT are running on SPARC-2 to acquire data, process data, edit pulse programs and store data. Many standard pulse programs contained in the CMXW and SPINSIGHT programs are used in various NMR experiments. Typical pulse sequence programs are shown here[67]:

```
1       /* 1pulse.sm4 */

2       .title          single pulse Bloch Decay
3       .a_mode         0
4       .channels       1
5       .include        defs.inc
5       .lpct           al
7       .time           pw ad rd pd
9               aqtm=dw*al+1u
10              exam=pw+rd+ad+aqtm+pd
11      .phase          p
12
13      .program
14      start:  A1(SS ph1)                              T1(1m);
15      loop:                           S1(TG)          T1(pw);
16              A1(AT rcvr)             S1(TB)          T1(rd);
17                                      S1(TB RE)       T1(ad);
18                                      S1(TB RE AE)    T1(aqtm);
19              A1(SS ph1)                              T1(pd)          I1(jump loop);
20
21      .list1  rcvr            P(p);
22      .list1  ph1             P(0); P(180); P(90); P(270);
23
24      .strings
25      abpn=0213
26      pw<excitation pulse
27      p<receiver phase
```

Some of the program lines are described here:

Lines 8-10: The .time command block

The .time command block defines time parameters which are pulse width(pw), acquisition delay(ad), receiver delay(rd), pulse delay(pd), aqtm(acquisition) experiment time(extm).

Lines 13-19: The .program command block

The .program command block contains instructions that actually start the RF Pulse and begin the experiment.

Lines 21-22: The .list1 command block

The .list1 command block sets up values for phase, frequency offset, and amplitude attributes.

Chapter 4. Experimental Results and Discussions

4-1. Intercalation compounds of graphite Li_xC for electrode materials

4-1.1. Material I: Lithium battery anode materials based on disordered, hard carbon (provided by V. Eshkenazi and E. Peled , Tel Aviv University)

1. Samples and experiments [68]

Cotton-based cloth was heated under nitrogen up to 500 °C. Cooling was performed under a reducing atmosphere of argon/hydrogen (92%/8% mixture) in order to minimize oxidation effects from possible exposure to air during later sample handling. Such material, even when fully pyrolyzed to 2500 °C, will not form the highly ordered graphite structure. This is referred to as hard carbon. After grinding, the material was heated to a final temperature of 1000 °C and cooled, again under argon/hydrogen. The obtained carbon was emulsified in cyclopentanone with 6.9% of polyvinyldifluorine (PVDF) binder and 4.9% of Shawinigan Black and pressed on a nickel grid to form the electrode. Three cells were made from this electrode in combination with Li metal(pressed on nickel grid) as the counter electrode in ethylene carbonate: diethyl carbonate (EC:DEC) electrolyte containing 1.2 M $LiAsF_6$. Cycling was performed on a 16-bit Maccor 2000 battery Tester. The procedure consisted of discharge at decreasing current density, namely, 2 mA/cm^2 down to 0.500 V vs. Li/Li^+, 1mA/cm^2 down to 0.300 V, 50 $\mu A/cm^2$.

According to the charge/discharge curve for hard carbon, the Li insertion curve exhibits two different regions: a sloping one, from 1.1 to 0.1 V (vs. Li/Li^+) denoted as the high-voltage region (HVR), and a plateau between 0.1 and zero V, denoted as the low-voltage plateau (LVR). The samples were chosen based on the curve [68] (see **Figure 4-1**).

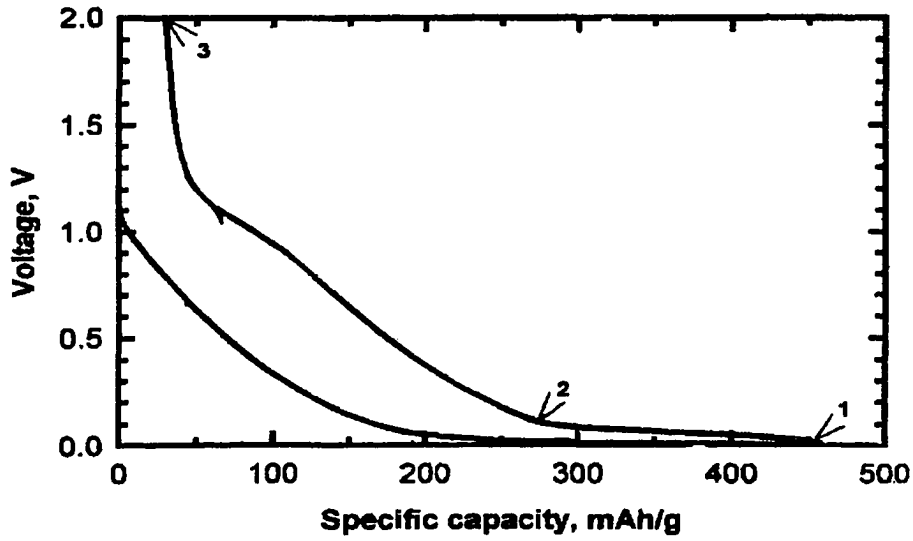

Figure 4-1: Charge/discharge curve of Li/carbon cell.[68]

Sample no.1 was taken at 0.009 V Cutoff point on discharge curve (lithium insertion), sample no.2 was prepared at 0.100 V of charge curve (lithium deinsertion) and sample no.3 was prepared at 2.000 V of charge curve.

Lithiated samples were sealed under argon in Aldrich 5mm (o.d.) x 23mm tubes, which were then surrounded by Teflon sleeves (home made) and packed into 7.5 mm (o.d.) Zirconia NMR rotors. Both wide-line and high-resolution MAS spectra were acquired, the latter utilizing MAS, with spin rate around 5 kHz. In some cases, proton decoupling was employed, with a typical decoupling field strength of 80 kHz. Aqueous LiCl solution was used as a chemical shift reference. Also the variable temperature experiment was done.

2. Experimental results

High resolution magic angle spinning (MAS) ^{7}Li NMR spectra, including spinning sidebands with 5.5 kHz spacing, of all three samples are shown in **Figure 4-2**. The lithiated carbon (Sample no.1) exhibits three prominent features: a broad component centered at about 50 ppm; a relatively narrow line at 17 ppm with an overlapping component at around zero ppm. The broad 50-ppm feature is attributed to intercalated Li^{+} ions residing between graphene rings in the small ordered (crystalline) domains of the hard carbon. This assignment is based on the well-known "signature" of approximately 40-50 ppm pertaining to single stage LiC_6 graphite [69]. Thus the ordered domains in hard carbon are intercalated in a fashion similar to that of graphite, where conduction electron density associated with the graphene planes, supplied by the ionized Li 2s electrons, yields the observed Knight shifts. The enhanced breadth of the 50 ppm component relative to that of the highly ordered graphite compound suggests a distribution of Knight shift, which is consistent with the small domain sizes in the ordered regions inferred from the XRD result [68].

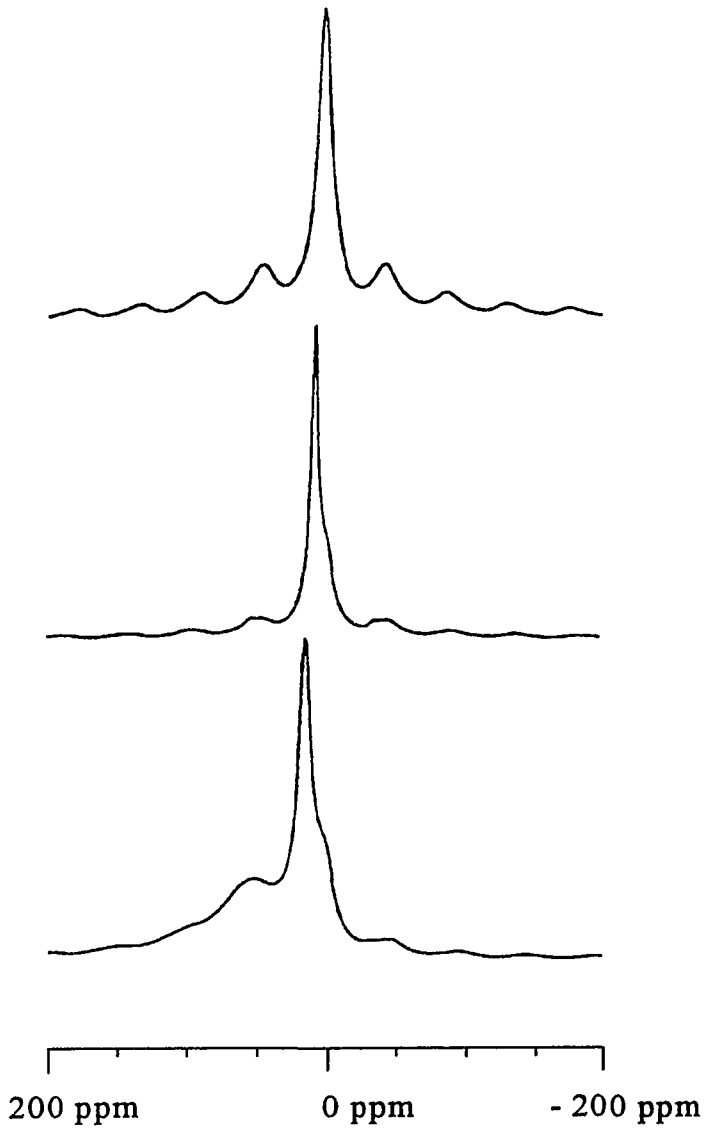

Figure 4-2: High resolution ^{7}Li NMR spectra of fully lithiated (sample No.1, bottom), partially delithated (sample No.2, middle), and totally delithated (sample No.3, top) hard carbon.

The ^{7}Li wide line NMR spectrum of sample no.1 is shown in **Figure 4-3**. With a conversion factor of 116 ppm/1000kHz, the scale in **Figure 4-3** is over a factor of two greater than that in **Figure 4-2**. Even with the low resolution inherent to wide-line methods, one can still clearly observe a left-side shoulder on the main peak, which is associated with the 50 ppm feature observed in the high-resolution mode. In LiC_6 graphite, one can observe additional satellite transitions ($\pm 3/2 \leftrightarrow \pm 1/2$) which arise due to the nuclear quadrupole interaction between the ^{7}Li quadrupole moment and the surrounding axial electric field gradient [70]. No satellite transitions are observed in **Figure 4-3**, however. Lithium sites that are heterogeneous in such a way as to yield a distribution in Knight shift will probably also produce a distribution of quadrupole coupling parameters and hence satellite transitions. Apparently the satellite distribution is sufficiently broad as to be effectively unobservable. An additional factor, which may be associated with the Knight-shift distribution and lack of quadrupole satellites, is turbostratic disorder of the graphene planes that was discussed in reference[68]. A wider scan than that shown in Figure 4-3 failed to detect metallic Li, which produces a strong Knight-shifted resonance at around 260 ppm.[69]

Sample no.2 was partially delithiated by effectively removing the LVP part of the charge curve. The 50 ppm component is clearly absent, and its assignment to graphite-like intercalated Li is given further credence by the charge/discharge behavior of graphite [71], which does not exhibit an HVR feature. The NMR spectrum of sample no.2 exhibits only the 17 ppm component with the shoulder centered at zero ppm. The correspondence of the 17 ppm feature with HVR portion of the lithium insertion suggests a fundamentally

different insertion mechanism from the LVP correlated intercalation. Spectroscopically, the 17 ppm chemical shift is more in line with covalently bonded Li than intercalated Li

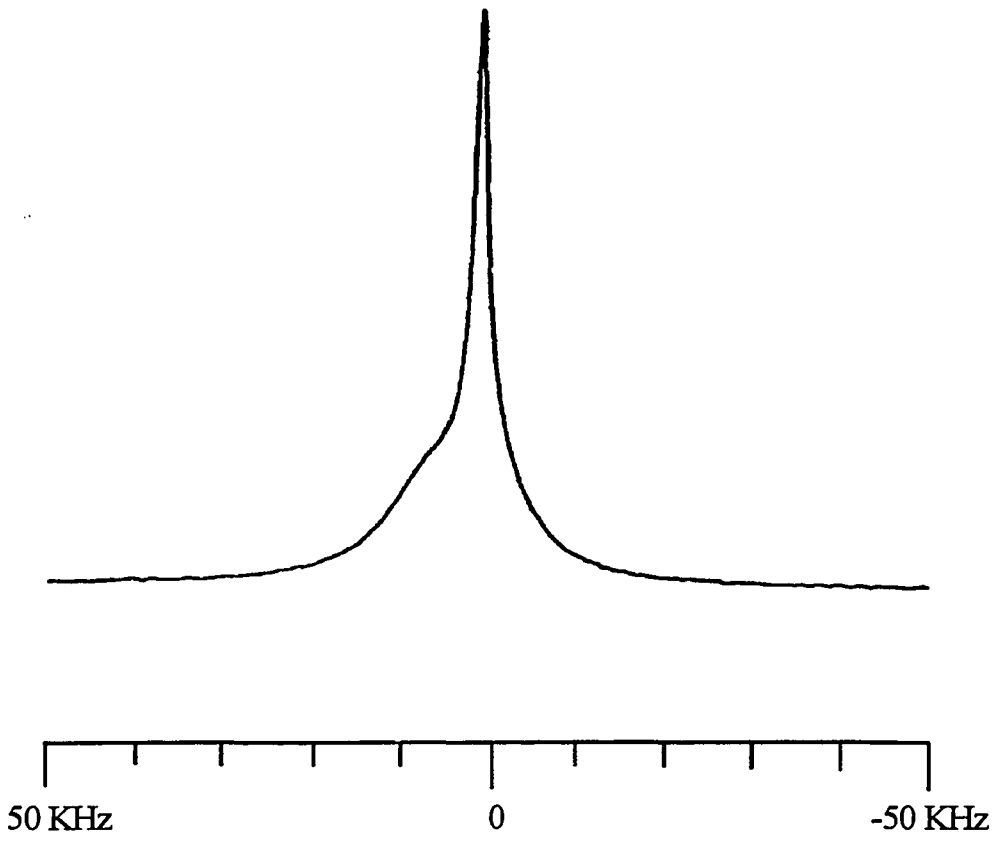

Figure 4-3: Wide line ^{7}Li NMR spectrum of fully lithiated hard carbon (samples No.1).

(the latter characterized by the substantially larger shift of ~ 50 ppm due to the conduction-electron density at the Li site), given that Li chemical isotropic shifts for covalent Li tend to be smaller still, typically ranging from +5 to –10 ppm (relative to

aqueous LiCl) [72]. The presence of a small amount of conduction electron density may be required to explain why the observed shift is somewhat outside the covalent range, but there is no additional experimental evidence for this at the present time. A recent ^{7}Li NMR study of disordered carbons based on mesophase-pitch and on perylene, which are structurally different from the carbon investigated in this work, revealed main resonance that shift from near 0 ppm to about 21 ppm as the Li content was increased from 100 to 600 mAh/g [32]. However no evidence for intercalated Li (around 40-50 ppm) in these carbons was reported, as discussed in the earlier literature survey [69].

In sample no.3, all reversible Li was removed, so that what Li remains is associated with the solid electrolyte interface (SEI). As seen from **Figure 4-2**, the shoulder feature present in samples no.1 and no.2 is the only spectroscopic component remaining in sample no.3. The effectively zero chemical shift of the spectrum of sample no.3 implies that the SEI consists of one or more ionic Li compounds. In lithiated graphite, LiF, Li_2O, Li-semicarbonates and carbonates have been identified by vibrational spectroscopy and photoelectron spectroscopy[73-76]. However, the generally small range of ^{7}Li chemical shifts among these species makes their specific identification by NMR difficult. Although there is no photoelectron or vibrational spectroscopy data for the present samples at this time, it is likely that the SEI composition is similar to that of the lithiated graphite. The relative integrated intensities of the three spectral components in sample no.1 were calculated on the basis of the intensities of the separate line shape components, which are shown in the fitted spectra for samples no.1 and no.2 in **Figure 4-4**. The results are listed in **Table 4-1**, alongside the Li contents estimated from the charge/discharge (potential vs. capacity) curve. The agreement between the spectroscopic

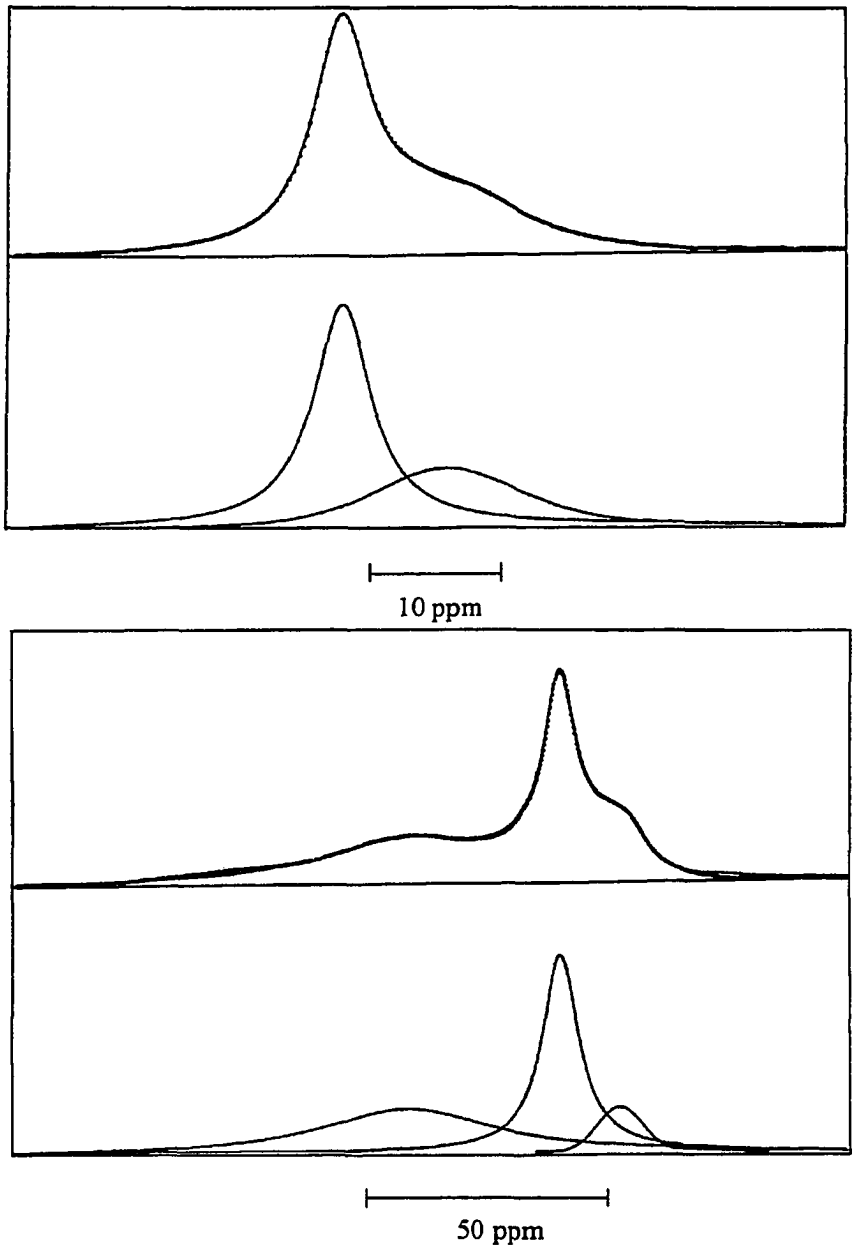

Figure 4-4: Simulation (solid curves) of experimental spectra (discrete points) with simulated spectral components shown below. Bottom: fully lithiated hard carbon (sample No.10; top: partially delithiated hard carbon (sample No.2).

Table 4-1. Li content of the samples, as determined by potential vs. capacity(V/C) or NMR.

Sample ID	1		2		3	
Methods	V/C	NMR	V/C	NMR	V/C	NMR
LVR	23%[a]	42%	_____	_____	_____	_____
HVR	46%[a]	49%	60%[a]	67%	_____	_____
SEI	31%[a]	9%	40%[a]	33%	100%[a]	100%
Total	100%	100%	100%	100%	100%	100%

[a] Estimations [68].

and potential vs. capacity results is particularly good for sample no.2 but not as satisfactory for sample no.1. For the latter, NMR gives a somewhat low estimate of the SEI lithium while the potential vs. capacity result is probably high. Likely sources of disagreement include the relatively low precision of counting all of the charge in the potential vs. capacity, and possibly some error introduced into the NMR line shape fitting associated with removing the spinning side-band.

Because of the previously cited correspondence between excess Li capacity and residual H content [77-79], attempts were made to see if spatial correlation between Li and H could be observed by NMR. ^{7}Li MAS spectra of sample no.2 are displayed in **Figure 4-5** at both 23 °C and –40 °C. Both single channel and proton-decoupled spectra were acquired at both temperatures. The effect of proton decoupling on the MAS linewidth is rather modest (reduced about 10-13%), but nonetheless observable. Because

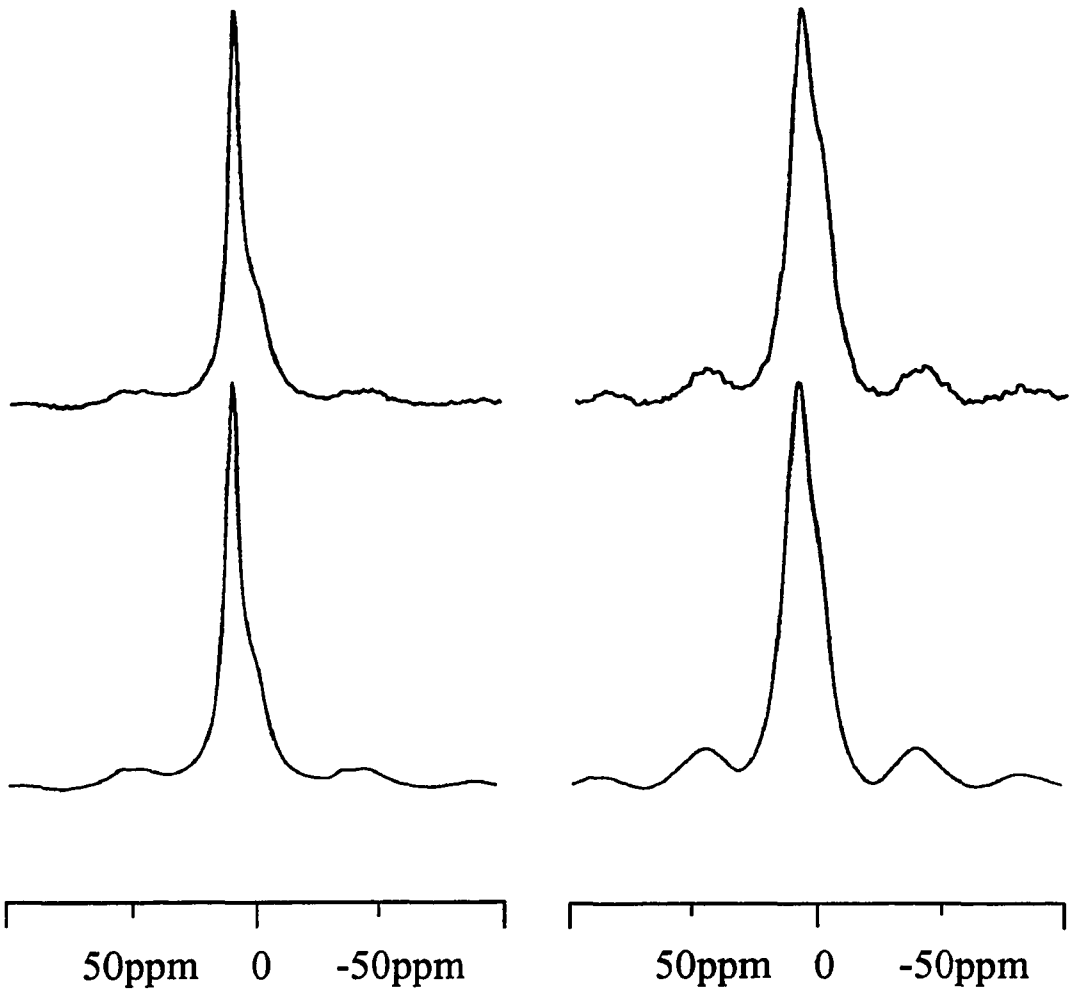

Figure 4-5: High resolution ^{7}Li NMR spectra of partially delithated hard carbon (sample No.2). Bottom: single-resonance spectra; top: proton decoupled spectra: left: +23°C; right: -40°C.

the nuclear magnetic dipole-dipole interaction falls off as the cube of the distance between the nuclei, the observation of any decoupling effect implies a Li-H separation of not more than about 4 Å. Because relative motion between the nuclei can average out the

dipole-dipole interaction, the effect of lowering the temperature was examined. The reduction in linewidth due to proton decoupling is about the same at both temperatures shown in **Figure 4-5**, and does not change significantly even at –100°C. In order to "calibrate" the decoupling method and thus place a lower bound on the Li-H distance, a decoupling experiment for a known compound, LiH, was performed. ^{7}Li MAS spectra of LiH (Aldrich), acquired at 23°C, are displayed in **Figure 4-6**, both with and without proton decoupling. The effect of proton decoupling on the LiH linewidth is, not surprisingly, rather significant, in that over half of the intensity outside of the first set of side bands, without decoupling, has been transferred to the central peak, with decoupling. Therefore, while the observation of a modest decoupling effect in lithiated hard carbon demonstrates that the 17 ppm signal arises from lithium that is spatially correlated with hydrogen (i.e., residing in the hydrogen-rich regions of the carbon), there is no evidence for Li directly bonded to H. If LiH does exist in the samples, its concentration is very small relative to the other Li species. Decoupling experiments on sample no.3, which contains only Li associated with SEI, also show a modest Li-H spatial correlation. The H in the SEI probably originates from reduction products of the electrolyte solvent.

3. Discussions

High Li capacity hard carbon exhibits two distinct insertion mechanisms, one is intercalation between turbostratically disordered graphene planes and the other is most likely covalent C-Li bond formation. Several alternative (to intercalation) schemes for Li insertion have been suggested for modified graphites, which contain terminal carbon sites [80]. For example, some postulated reactions and their estimated E^{o} values (electro-chemical potential) are [80]:

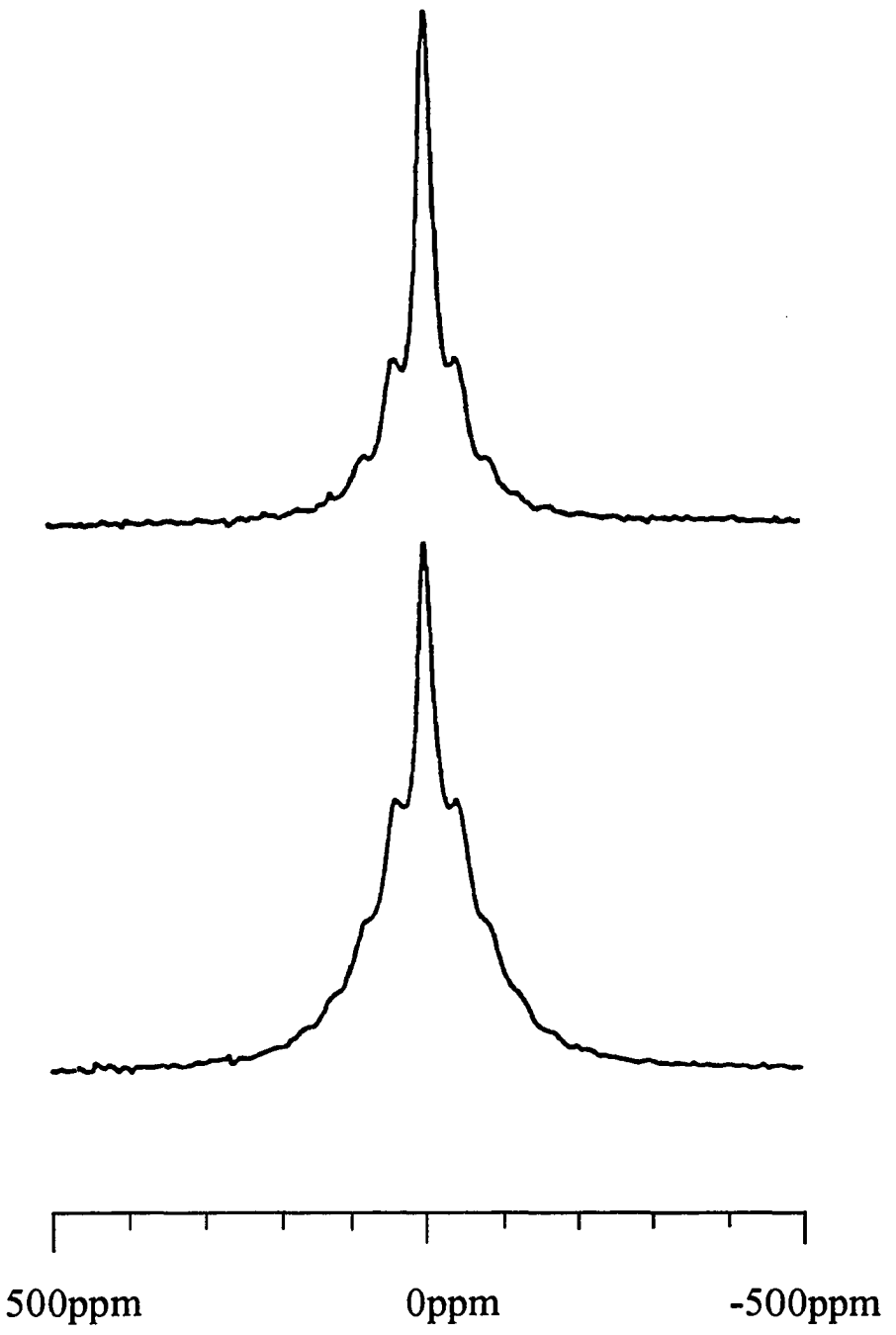

Figure 4-6: High resolution ^{7}Li NMR spectra of LiH: Bottom: single resonance spectrum; Top: proton decoupled spectrum.

$$C^{\bullet} + Li = C\text{-}Li \qquad (E^{\circ} \sim 0.3\ V)$$

$$C\text{-}H + 2Li = C\text{-}Li + LiH \qquad (E^{\circ} \sim 0.6\ V)$$

$$C\text{-}H + Li = C\text{-}Li + 1/2\ H_2 \qquad (E^{\circ} \sim 0.5\ V)$$

All of the estimated E° values are within the HVR and are thus candidates for Li insertion via covalent bond formation in hard carbon. Although there is no evidence of the presence of LiH (as per the proton decoupled NMR experiments), reaction 2 cannot be ruled out at this time because of the several-day time delay between sample preparation and the NMR measurements. Any LiH formed (if it did form) during lithiation would soon react within the carbon matrix to form another product. For example, the very reducing hydride ion could react with oxygen- containing species in the SEI.

Finally, a qualitative model of Li insertion in hard carbon is depicted in **Figure 4-7** where both intercalated and covalent Li sites are shown. The disordered, hydrogen-rich regions of the carbon are portrayed as voids in the graphene ring array and edge sites, although other arrangements are certainly possible. The Li-H spatial correlation suggested here arises from Li and H bonded to adjacent C atoms, although at this time it is not possible to rule out Li and H bonded to the same C atom.

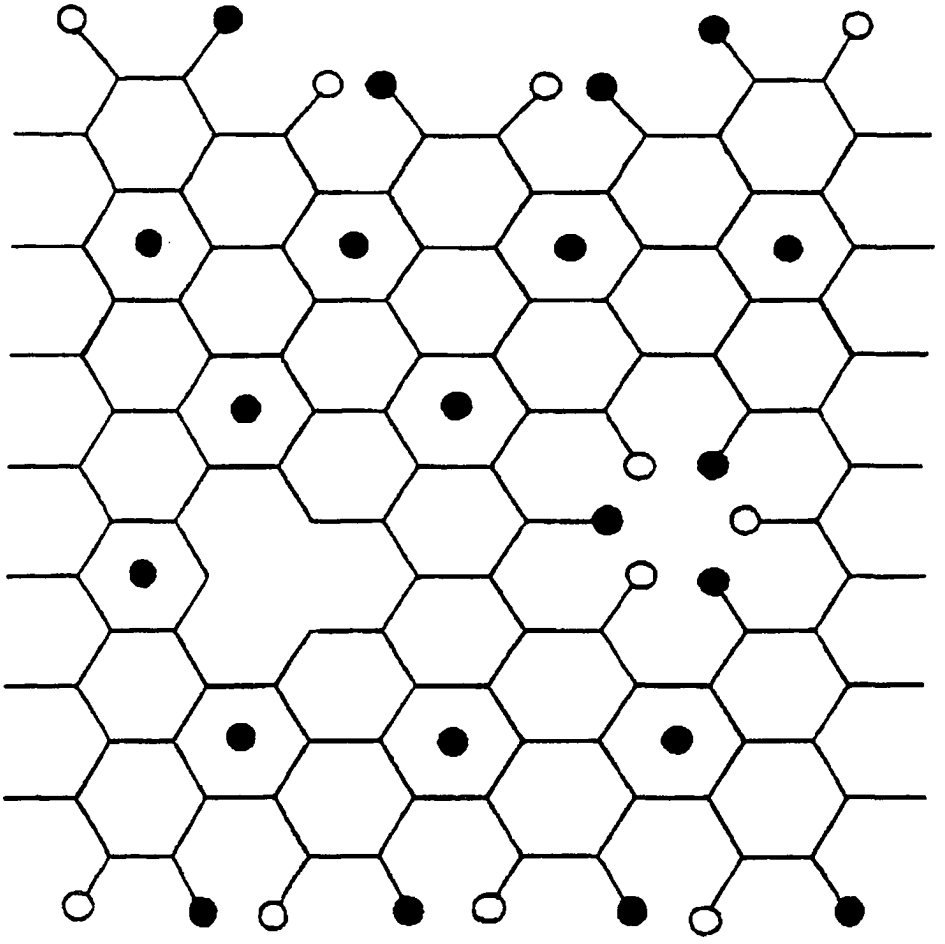

Figure 4-7: Structural model of hard carbon depicting intercalation, edge, and void sites for Li (filled circle). Hydrogen is represented by the opening circles.

4-1.2. Material II: Lithiated natural graphite before and after mild oxidation

(Provided by C. Menachem and E. Peled, Tel Aviv University)

1. Samples and experiments [81]

To prepare the NMR samples, electrochemical Li/Li_xC_6 cells were constructed. These cells consisted of porous natural graphite (NG7-Kansai Coke) electrode and a lithium foil supported by a nickel screen, a separator and electrolyte containing 1 M lithium hexafluoroarsenate ($LiAsF_6$) and 1:2 (v/v) mixture of ethylene carbonate (EC) and diethyl carbonate (DEC). The graphite electrodes were made by spreading paste which consists of 6.5% (w/w) Poly (vinylidene fluoride)(PVDF), 93.5% graphite powder and cyclopentanone on the nickel screen. The electrodes were rolled to a thickness of 200 μm and vacuum dried at 170 °C for 3 hours. The partially oxidized graphite (hereafter referred to as burnt) was prepared prior to electrode preparation: NG7 powder was air-oxidized at 550°C for 30 min and lost 15% of its initial weight. The cells were cycled with the use of a 16-bit Maccor 2000 Battery Tester at 50 $\mu A/cm^2$ over voltage range of 0.8-0.005 V. The cells were cycled one full intercalation-deintercalation cycle. At the second cycle, one set of cells was partially intercalated down to 120 mV and another set of cells was fully intercalated (down to 5 mV). After 24 hours at rest, the cells were disassembled. The graphite electrodes were washed in dimethyl carbonate (DMC) and vacuum dried at room temperature for 1 hour. The lithiated graphite was separated from the nickel screen, crushed and inserted into 5mm (o.d) x 22 mm Pyrex tubes for the NMR measurements. Both wide line and magic angle spinning (MAS) NMR measurements were conducted on 500-700 mg sample at a ^7Li frequency of 116.9 MHz. A single pulse

sequence was employed for spectral acquisition, with a typical pulse width of 4μs. The MAS spinning rate was about 3 kHz, and the Pyrex sample tubes were fitted with Teflon sleeves prior to insertion into the MAS rotor. Aqueous LiCl was employed as a chemical shift reference.

2. Experimental results and discussions

In order to identify the environment of the extra capacity lithium in burnt graphite, wide-line ^{7}Li measurements of pristine graphite, lithiated to x = 0.21 (Li_xC_6), and burnt graphite, lithiated to x = 0.24, were carried out. The two spectra, displayed in **Figure 4-8**, are similar in appearance, both being dominated by a strong central transition flanked by outer satellite transitions associated with a first-order electric quadruple interaction between the ^{7}Li nucleus and the axial electric field graphite surrounding the Li^+ ion. Similar spectra for Li-intercalated graphite have been reported previously [69]. Both main peaks are centered at about 40 ppm, close to the 45 ppm Knight shift value reported for LiC_6 [69]. In addition to the intercalated ^{7}Li signal, there is some NMR intensity near around 0 ppm in both samples, considerably more so for the burnt graphite. As discussed previously in the case of hard carbon, this feature corresponds to the SEI [82,83]. The considerably larger feature in the burnt graphite, centered around 12-18 ppm, is attributed to the extra reversible lithium capacity in this material.

In order to gain additional information on the nature of this excess Li, high resolution ^{7}Li MAS measurements were undertaken, and MAS spectra of both samples described above (pristine graphite lithiated to x=0.21 and burnt graphite lithiated to x=0.24) are shown in **Figure 4-9.** The high-resolution spectra reveal additional intensity

in the burnt graphite compared to pristine graphite, at least some of which is associated with the excess Li capacity in the former, more clearly than the wide-line spectra do. The excess Li spectral component appears as a broad line centered at around 14 ppm. In addition, there is greater intensity in the 0 ppm region in the burnt graphite compared to the pristine graphite. Both wide-line and MAS ^{7}Li NMR measurements on fully intercalated graphite, corresponding to LiC_6 for pristine graphite and $Li_{1.08}C_6$ for burnt graphite, were also performed. The spectra are qualitatively similar to those for the partially lithiated samples (**Figure 4-8 and 4-9**), except that the SEI and excess Li (the latter in only the burnt sample) contribution to the signal is considerably smaller than that of the intercalated Li, due to the higher degree of lithiation in these samples. The 14 ppm feature is almost unobservable in the fully lithiated burnt graphite, which implies that the extra Li capacity is associated with potentials larger than 0.1 V, and not with potentials close to 0, vs. Li.

The mechanism by which partial oxidation increases the reversible Li capacity is believed to be related to Li bonding at edge atomic sites, as opposed to intercalation between graphene sheets. In particular, oxidation proceeds most rapidly at the edge sites, and results in the formation of acid groups, which have been detected directly (along with CH and COH and C=O groups) by X-ray photoelectron spectroscopy [75]. These acid groups, in turn, are transformed into a chemically bonded SEI during the first Li insertion step [82,83]. The larger NMR intensity around 0 ppm in the burnt sample (**Figure 4-9**) is attributed to either a thicker SEI, or an SEI that is richer in Li salts (at the expense of organic decomposition products), compared to the pristine graphite case. This conclusion

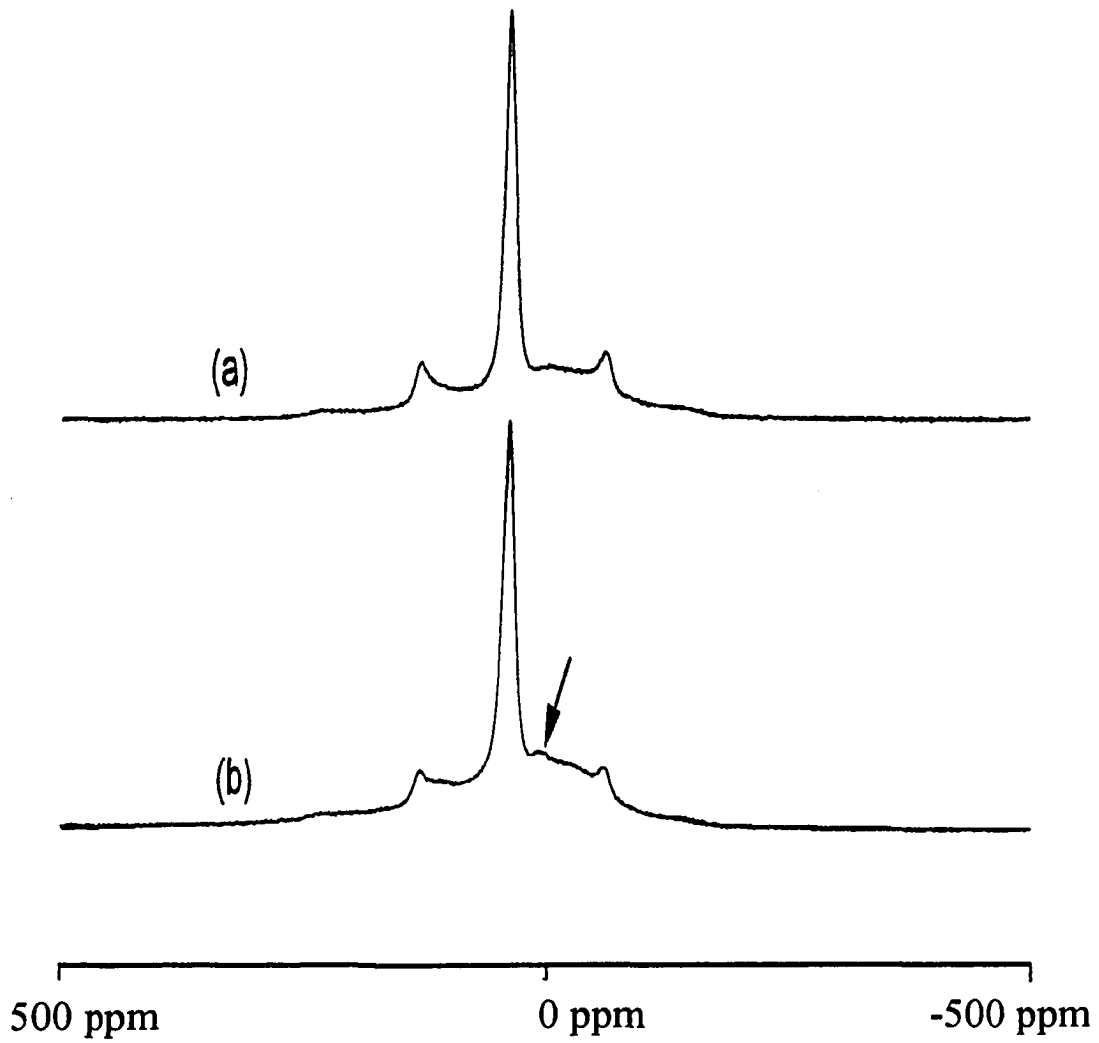

Figure 4-8: Wide-line ^{7}Li NMR spectra of lithiated pristine NG7, $Li_{0.21}C_6$ (a) and lithiated burnt NG7, $Li_{0.24}C_6$ (b). Arrow indicates spectral component associated with excess lithium capacity.

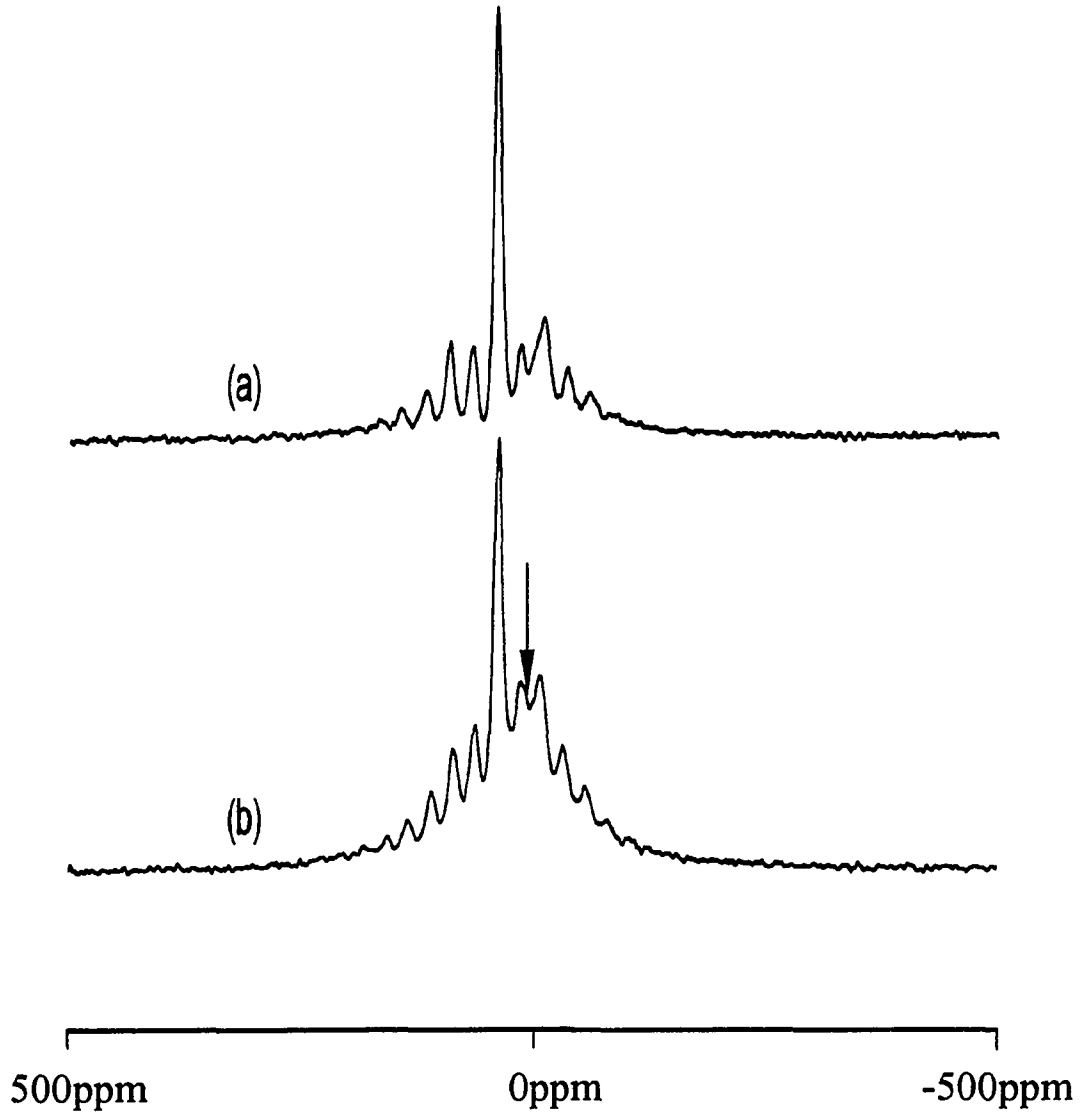

Figure 4-9: High resolution MAS ^{7}Li NMR spectra of lithiated pristine NG7, $Li_{0.21}C_6$ (a) and lithiated burnt NG7, $Li_{0.24}C_6$ (b). Arrow indicates spectral component associated with excess lithium capacity.

is supported by X-ray photoelectron spectroscopy results, which found evidence of both thicker SEI and higher Li salt content in burnt graphite compared to pristine graphite [73]. The fact that the irreversible capacity of the latter is smaller than that the former [80,83] can be taken as evidence that the SEI formation process is more efficient in burnt graphite.

4-2. New anode materials Li-SnO

(Provided by J. Sakamoto, C.K. Huang, and S. Surampudi, Jet Propulsion Laboratory)

4-2.1. Sample background and experiments [84]

Li was electrochemically titrated into SnO using half cells containing Li as the anode, SnO as the cathode and 30% EC/70% DMC/1M:$LiPF_6$ electrolyte. SnO electrodes were fabricated using 6% (by weight) PVDF binder, and 10% carbon black and copper foil substrates. Selected amounts of Li, varying from 0 to 6.4 mol per mol of SnO, were titrated into or extracted from SnO using galvanostatic measurements and a current density of 0.20 mA /cm^2. Reference alloys were prepared by adding metallic Li to molten Sn in an argon dry box, and annealing at 150 °C for several hours. For NMR measurements, samples were packed into hermetically sealed 7.5 mm Zirconia NMR rotors, also in the dry box. High resolution magic-angle-spinning (MAS) NMR spectra were acquired, utilizing a single-pulse sequence (typical pulse width of 5μs) at 23°C. Spin rates were about 5 kHz. Aqueous LiCl was employed as a chemical shift reference.

4-2.2. Experimental results and discussions

High resolution ^{7}Li NMR spectra of Li/SnO samples with Li/SnO ratios of 0.5, 2.0 on discharge (in the Li/electrolyte/SnO half-cell), 2.0 on charge (after having been discharged to the maximum Li/SnO ratio of 6.4) and 1.8 on charge (despite the expectation that Li contents below 2.0 are irreversible, the 1.8 value was indicated from the coulometric titration curves corresponding to the charge/discharge reactions), are displayed in **Figure 4-10**. Also included is the spectrum of a commercial (Aldrich) Li_2O reference compound. All of the Li/SnO spectra are similar in appearance and are characterized by an isotropic chemical shift of about zero ppm (relative to aqueous LiCl), as is the Li_2O reference compound. However the Li/SnO spectra exhibit a more extensive spinning side band pattern than Li_2O. X-ray diffraction measurements in this investigation [84] and in other [85] have failed to detect the presence of crystalline Li_2O. These spectra are thus attributed to an amorphous Li_2O phase. The enhanced line width (relative to the crystalline compound), most of which is due to the ^{7}Li-^{7}Li nuclear dipole-dipole interaction, arises from a distribution of Li-Li distances within the amorphous compound. An additional contribution to the line intensity (and line width), especially for the x=0.5 compound, is expected from lithium-containing electrolyte reduction products. In lithiated carbons, such reduction products are present as the SEI, which has been discussed previously in this thesis and in reference [86]. Hydrogen in the SEI yields a broader NMR line via ^{7}Li-^{1}H dipolar interaction, and the x=0.5 sample has the largest SEI/Li_2O ratio. In fact, this sample also exhibits an enhanced low-resolution (non-spinning) NMR line width.

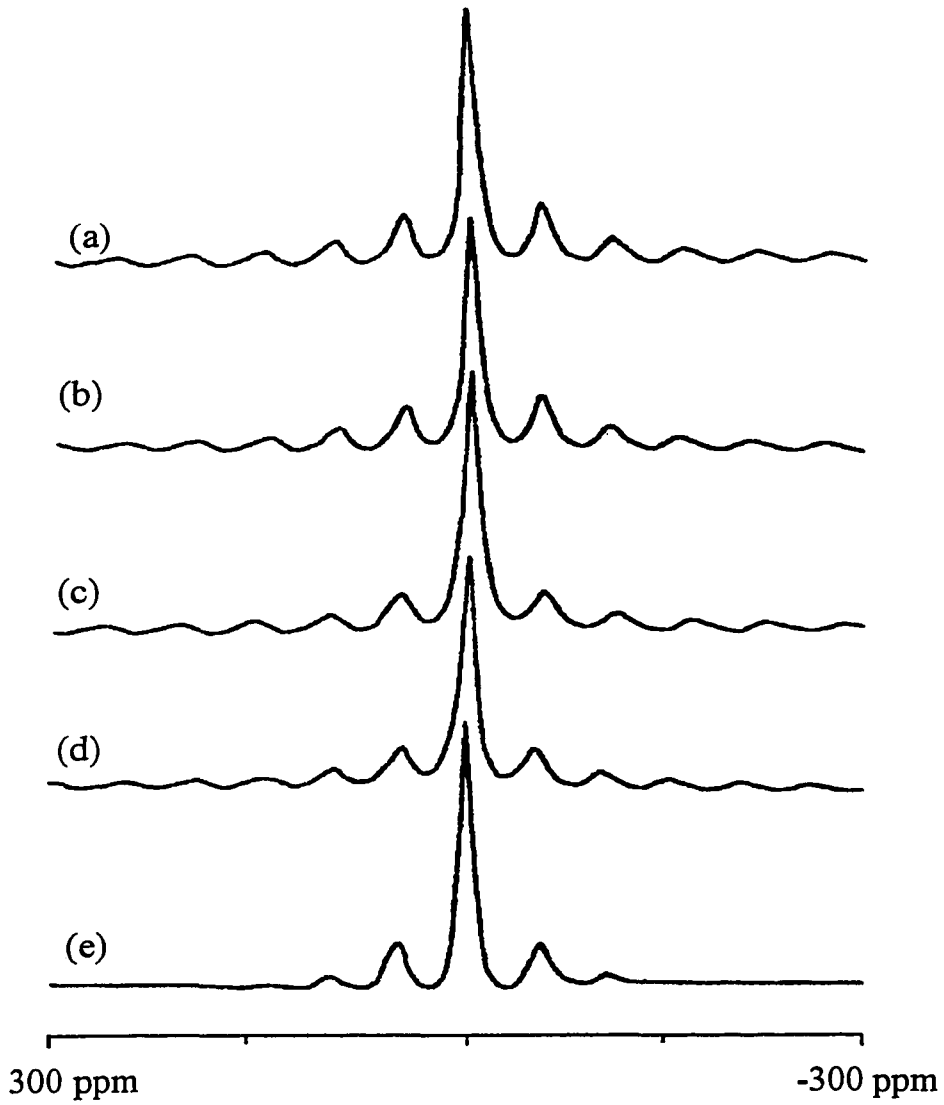

Figure 4-10: High resolution ^{7}Li NMR spectra of electrochemically lithiated SnO, with Li/SnO ratios of: (a) 0.5; (b) 2.0, on first discharge of half –cell; (c) 2.0, on subsequent charge of half –cell; (d) 1.8 on subsequent charge of half-cell; (e) crystalline Li_2O reference compound.

High resolution ^{7}Li NMR spectra for sample with a Li/SnO ratio equal to 4.3 are shown in **Figure 4-11**. The top spectrum corresponds to initial lithiation and the middle spectrum refers to a sample partially delithiated from the maximum value (Li/SnO=6.4). The $Li_{2.3}$ Sn reference alloy spectrum appears at the bottom of the figure. Both lithiated SnO spectra in **Figure 4-11** exhibit three distinct Li environments corresponding to the intense feature at ~17 ppm, a large shoulder centered at around 0 ppm and a smaller peak at 43 ppm. The 0 ppm shoulder is attributed to the same amorphous Li_2O phase as observed in the Li/SnO ≤ 2 samples (**Figure 4-10**) and the other peaks arise from Knight shift interactions in the metallic Sn/Li phase. Earlier work reported a similar 17 ppm shift for a sample with Li/SnO ratio very close to the 4.3 value chosen for this investigation, but those results were apparently derived from wide-line as opposed to high resolution NMR, so it is likely that the smaller 43 ppm peaks was obscured by the overall line width [87]. The reference $Li_{2.3}Sn$ alloy exhibits only two peaks, a large one at 17 ppm and a smaller one at around 47 ppm, with prominent spinning sidebands. Thus it appears that the NMR data for Li/ SnO values up to 4.3 fit the simple model given in the introduction, namely in this case that the Li/SnO=4.3 material is approximately a superposition of Li_2O and $Li_{2.3}Sn$. The presence of the smaller 43-47 ppm features, which represents a significantly different Li^+ structural and electronic environment than that giving rise to the 17 ppm peak, implies that there is more than one "pure" phase in $Li_{2.3}Sn$ alloy. The cycled sample (middle spectrum in **Figure 4-11**), in fact, has narrower spectral features than the initially lithiated sample (top spectrum), which suggests that the alloy phases become more sharply defined upon cycling.

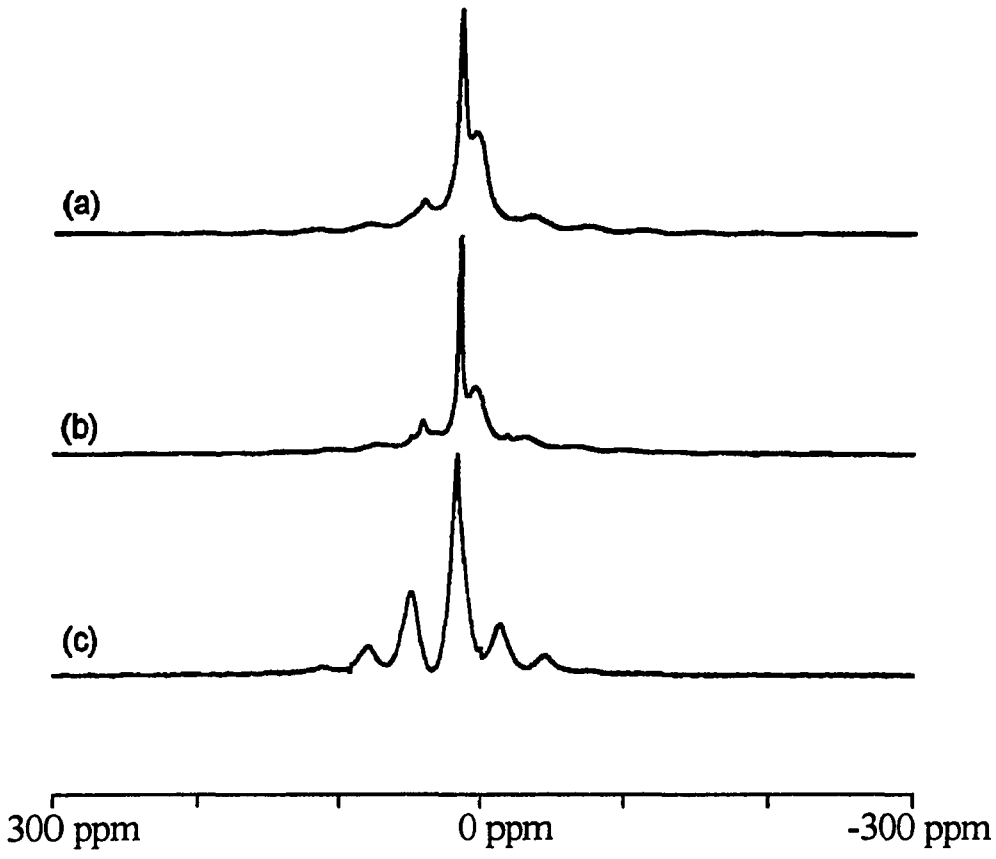

Figure 4-11: High resolution ^{7}Li NMR spectra of electrochemically lithiated SnO, with Li/SnO ratio of 4.3: (a) on first discharge of half-cell, (b) on subsequent charge of half-cell; (c) $Li_{2.3}Sn$ reference alloy.

According to the Sn/Li alloy phase diagram, well ordered alloy phases exist for several Li/Sn ratios, including 2.3 and 4.4, the latter of which represents the maximum Li loading possible [88]. The charge/discharge behavior of SnO/Li electrodes also suggests that 6.4 is the maximum Li/SnO ratio obtainable electrochemically [85]. High resolution ^{7}Li NMR spectra of both Li/SnO equal to 6.4 and the $Li_{4.4}Sn$ reference alloy are displayed in **Figure 4-12**. The latter exhibits a broad major component centered at around 69 ppm, consistent with a metallic environment around the Li^+ ions, and a minor and narrow component at around 8 ppm. The results, that $Li_{4.4}Sn$ alloy exhibits two major components (69 ppm and 8 ppm), are supported by J.R Dahn 's work [37]. In that paper, it is indicated that there exist two different structure units sites in alloy $Li_{4.4}Sn$ ($Li_{22}Sn_5$). In addition, there is a small peak, representing less than 2% of the total Li content of the sample, at around 260 ppm, attributed to metallic Li. The presence of a small amount of metallic Li is not surprising, given that the nominal composition of the alloy corresponds to the maximum possible Li content. The Li/SnO sample however shows markedly different behavior, with only a single peak at around 8 ppm, very close to the minor peak observed in the $Li_{4.4}Sn$ alloy. The asymmetry of the line arises from spectral intensity at around 0 ppm, again due to the same amorphous Li_2O phase observed in the other Li/SnO samples represented in **Figure 4-10,12**.

The large difference in Knight shift environments between the melt-prepared alloy and the electrochemically lithiated metal oxide at maximum Li content reflects a significant difference in the local structures of these two materials. Unfortunately, the lack of X-ray diffraction peaks corresponding to an ordered alloy phase in the Li/SnO =6.4 sample precludes a sample interpretation based on the presence of known crystalline

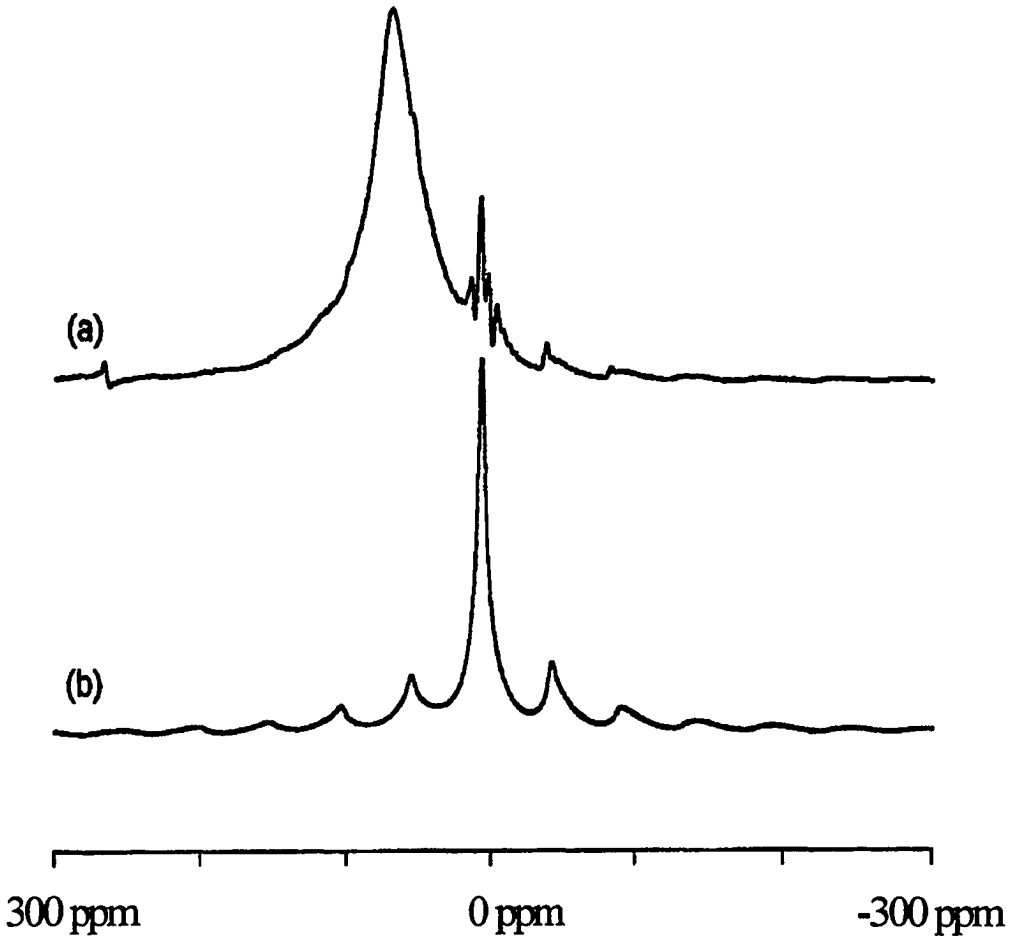

Figure 4-12: High resolution ^{7}Li NMR spectra of: (a) $Li_{4.4}Sn$ reference alloy; (b) electrochemically lithiated SnO with Li/SnO ratio of 6.4.

phases[84]. For example, metallic tin exists in two forms, the so-called α-form with a cubic structure and the β-form with a tetragonal structure, the latter being the dominant phase above 13°C [89]. It is thus possible that Sn/Li alloys could also have different stable structure, perhaps depending on factors such as Sn/Li ratio and whether the samples were prepared from the molten phase or electrochemically. Although there are no published NMR data for Sn/Li alloys (except for a few specific compositions in the reference [87]), we suggest that a different form of Sn/Li alloy can be stabilized by electrochemical lithiation than occurs by melt preparation, particularly at high Li contents. At this time it is not possible to assign the 8ppm component to a particular local alloy environment, but it must be differ considerably from that corresponding to the 69 ppm feature, owing to the sensitivity of NMR to the structural and electronic environment of Li^+ ions in metallic hosts. In fact, even the melt-prepared alloy exhibits some of the 8 ppm feature observed for the lithiated metal oxide, although the resonance in the latter is significantly broader, reflecting the disorder implied by the X-ray diffraction results, which showed no crystalline alloy phases. It remains to determine what the two alloy structures are that give rise to the 8 ppm and 69 ppm ^{7}Li signals, and to explain why the former is preferred in the fully lithiated SnO material.

4-5.3. Sub-conclusions

In order to test the hypothesis that lithiation of SnO anodes proceeds by the mechanism: $SnO + xLi \rightarrow Li_2O + Li_{x-2}Sn$, we have performed high resolution ^{7}Li NMR measurements on several Li/SnO materials prepared electrochemically, and on the corresponding $Li_{x-2}Sn$ alloy made by adding Li to molten Sn. Agreement between the

NMR results and the proposed mechanism is reasonable at Li/SnO ratios up to 4.3. Although there is no evidence of crystalline Li_2O, an amorphous form of Li_2O appears to be present. At the maximum Li/SnO ratio (6.4) the Li environments of the lithiated SnO and reference $Li_{x-2}Sn$ alloy are very different, suggesting that the metallic $Li_{4.4}Sn$ phase formed by electrochemical lithiation of the oxide is structurally different than that of the melt-prepared alloy.

4-3. Battery cathode material $Li_{1+y}CoO_2$

(Provided by Dr. F. Croce el at, University of Rome. Some NMR performed by Dr.S. Arumugam)

4-3.1. Samples and experiments [10]

Samples of $Li_{1+y}CoO_2$ were prepared by mixing thoroughly lithium and cobalt carbonates (previously dried) (Aldrich, p.a.), corresponding to the following nominal composition y=0.00, 0.08, 0.35 and 0.50, with acetone in a planetary mill for 2 hours. Magnesium was added as MgO to the former two compositions in order to evaluate the effect of doping on the electrical properties of $LiCoO_2$. All the mixtures were transferred to high-purity alumina boats and slowly heated within 5 hours in air to 650°C, held at this temperature for 10 hours and then allowed to return to room temperature gradually inside the furnace after the power was switched off. The powders were subjected to further heating at 900 °C in air for 10 hours.

Solid-state NMR measurements of both ^6Li and ^7Li isotopes (at natural abundance) were performed at $^{6,7}Li$ resonance frequencies of 44 and 116 MHz,

respectively. Sample masses ranged from ~500-1000mg. Both wide-line and high-resolution MAS techniques were employed. Wide-line spectra were obtained by both single pulse and quadrupole echo sequences, with typical 90° pulse widths of 2μ. MAS spectra, with spinning rates up to 7 kHz, were obtained with single pulses (90° pulse widths of 4 ms), and spin-lattice relaxation times (T_1) were determined by inversion recovery. Aqueous LiCl was used as NMR reference.

4-3.2. Experimental results and discussions

Wide-line ^{7}Li and ^{6}Li spectra of stoichiometric $LiCoO_2$ (y=0.00) are displayed in **Figure 4-13**. The main peaks are shifted less than 1 ppm with respect to the aqueous LiCl reference. This result confirms the expectation that the Li is completely ionized [14]. This is validated further by high resolution MAS results (shown later). The figures also show there are no quadrupole splittings besides the central peaks. The lack of quadrupole splittigs in both the ^{7}Li and ^{6}Li spectra demonstrates that the electric field gradient surrounding the Li site is very small. This is consistent with the octahedral symmetry of the Li sites deduced from the crystal structure of the stoichiometric compound (see **Figure 1-2**). The experimental ratio of the ^{7}Li/^{6}Li line widths (full width at half maximum) is ~ 3.4. Heteronuclear dipolar interactions between ^{6,7} Li and ^{59}Co should scale as the magnetic moment ratio of the two isotopes ($\gamma_7/\gamma_6 = 2.7$), while the ^{7}Li - ^{7}Li homonuclear dipolar interaction should be about 4 times that of the ^{7}Li - ^{6}Li heteronuclear contribution [59]. These two sources of line-broadening then appear to account satisfactorily for the experimental result. Additional broadening could arise from paramagnetic sites in the material, but these are deemed to be insignificant because of the

+3 oxidation state cobalt in the stoichiometric compound. The main peaks obtained from the other two cases where y=0.08 and 0.35 are also shifted very little, with no quadrupole splittings present. Compared with the stoichiometric sample (y=0.00), there is a modest increase of about 10% in FWHM for the excess Li samples (y=0.08, 0.35). The measurements of spin-lattice relaxation time T_1 at 23 °C is summarized in Table **4-2.**

Table 4-2 The spin-lattice relaxation T_1 of $Li_{1+y}CoO_2$ (y=0.0, 0.08 and 0.35), at 23°C.

$Li_{1+y}CoO_2$	y=0.0	y=0.08	y=0.35
T_1(ms)	390	144	137

The enhanced line width and relaxation rates in the excess Li samples are attributed to the generation of Co^{2+}, although it appears as though there is far less Co^{2+} than given by the value of y. For example in 10% Li-deficient material ($Li_{0.9}CoO_2$), the corresponding presence of paramagnetic Co^{4+} yields approximately a 30% increase in ^{7}Li line width [14]. In addition there are some intriguing low-intensity features which are substantially shifted from the main resonance. These are readily seen in the expanded vertical-scale spectra of the sample of y=0.35 displayed in **Figure 4-14 (a, b)**. For ^{7}Li spectra, two small peaks are observed to be located at 40kHz(~300ppm) and 160kHz(~1380ppm), whose integrated signal intensities relative to the main peak are approximately 3.5% and1%, respectively. By inversion recovery, it was also determined that the first small peak (at 40kHz) has a T_1 of about 7ms. The T_1 value and the peak position suggested that it might be due to metallic Li, which has a Knight- shift of 265ppm[69]. However, by

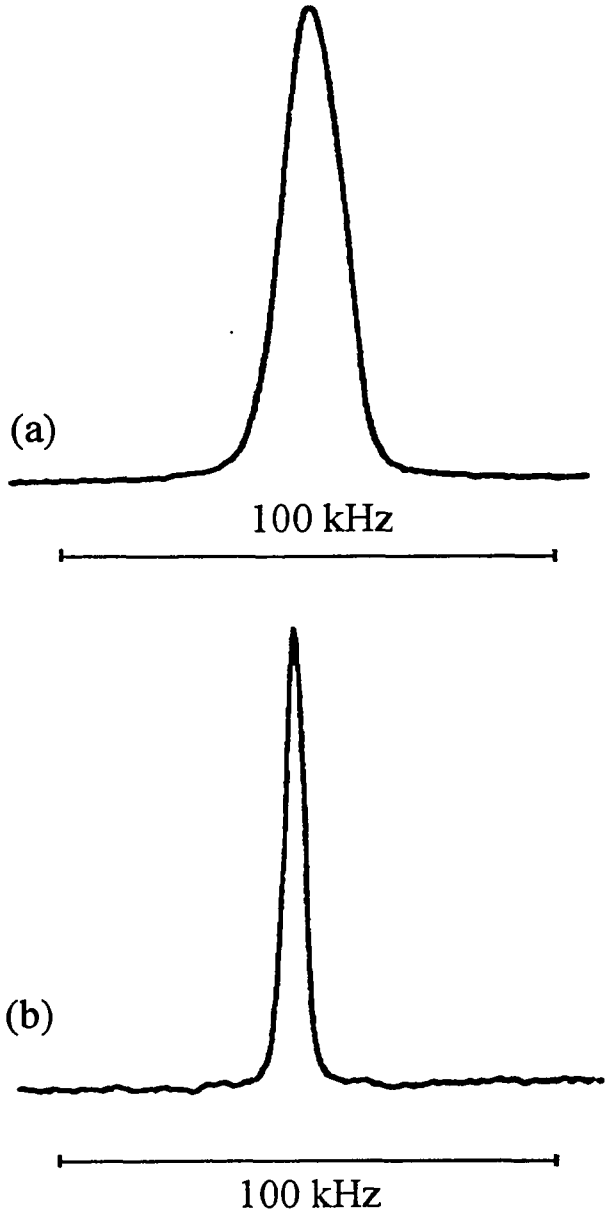

Figure 4-13: NMR spectra of stoichiometric $LiCoO_2$. (a) Lithium-7; (b) Lithium-6.

variable temperature NMR, it was found that the small peak (40kHz) shifts even further downfield with decreasing temperature, as summarized in **Table 4-3.**

Table 4-3 Chemical (paramagnetic) shifts of extra components in non-stoichiometric $Li_{1+y}CoO_2$ at various temperatures

T(°C)	21	-40	-80	-100
Shift(kHz)	41.44	51.73	57.15	65.28
Shift(kHz)	153.0	200.7	224.5	>250

The result demonstrates that the origin of the shift is a localized paramagnetic ion interaction (i.e. with a nearby Co^{2+}), rather than a metallic Knight shift, which is almost temperature independent in the experimental temperature range. The usually large shift of the second peak (at about 160kHz) is attributed to interstitial Li^+ ions in even closer proximity to paramagnetic Co^{2+} ions than those giving rise to the 40 kHz-shifted peak in the excess Li material. The temperature dependence of this feature's shift (160 kHz) is also given in **Table 4-3**. The ^6Li spectrum in **Figure 4-14(b)** reveals that both of the shifted features described above move in by the γ_6/γ_7 ratio, thus helping to confirm their identity. **Figure 4-15** is an expanded vertical scale ^7Li NMR spectrum of the y = 0.08 sample, showing the 300 ppm feature with greater resolution than that of y = 0.35 **(Figure 4-13a)**. The far-shifted feature at about 155 kHz(1400 ppm) is also present.

With the paramagnetic-shifted Li accounting for no more than ~4% of the total signal intensity, it remains to identify the nature of the majority of the excess Li in the y = 0.35 sample. Spectra obtained under MAS are useful in this regard, although only indirectly so for the case of ^7Li. **Figure 4-16** shows the ^7Li spectrum resulting from 7

kHz MAS in combination with an inversion recovery sequence, with a pulse delay chosen to produce a null in the main part of the wide-line spectrum. It is clear that some intensity remains, diamagnetically shifted about 2 kHz (~17 ppm) from the position of the nulled signal from the stoichiometric Li, thus indicating a different T_1 than the main component. The ^{6}Li MAS results are clearer still, in which case the extra diamagnetically shifted component could be resolved directly, without selective inversion (or nulling). Lithium-6 spectra under 6 kHz MAS, with two different horizontal frequency scales, are displayed in **Figure 4-17**. In Figure **4-17(a)**, the 300 ppm peak is clearly seen about 3 kHz outside the high-field spinning side-band. The close-in shoulder is shown in greater detail in **Figure. 4-17(b)**, shifted about 750 Hz (again, about 17 ppm). This extra component is attributed to a Li environment that is not much different, magnetically or with regard to symmetry of the surrounding charge distribution (i.e. absence of quadrupole effects), than the stoichiometric Li. If the excess Li were to enter the structure in the same ionic configuration as the stoichiometric Li, then the excess electrons introduced would necessarily reduce the formal cobalt valence, with a one-to-one correspondence (i.e. $Li_{1+y} \rightarrow Co^{3-y}$). From the results in **Table 4-4**, the average Co valence of the y = 0.35 sample is reduced by only ~ 0.15. The modest increase in NMR line broadening suggests that even this value obtained by chemical analysis may be somewhat high.

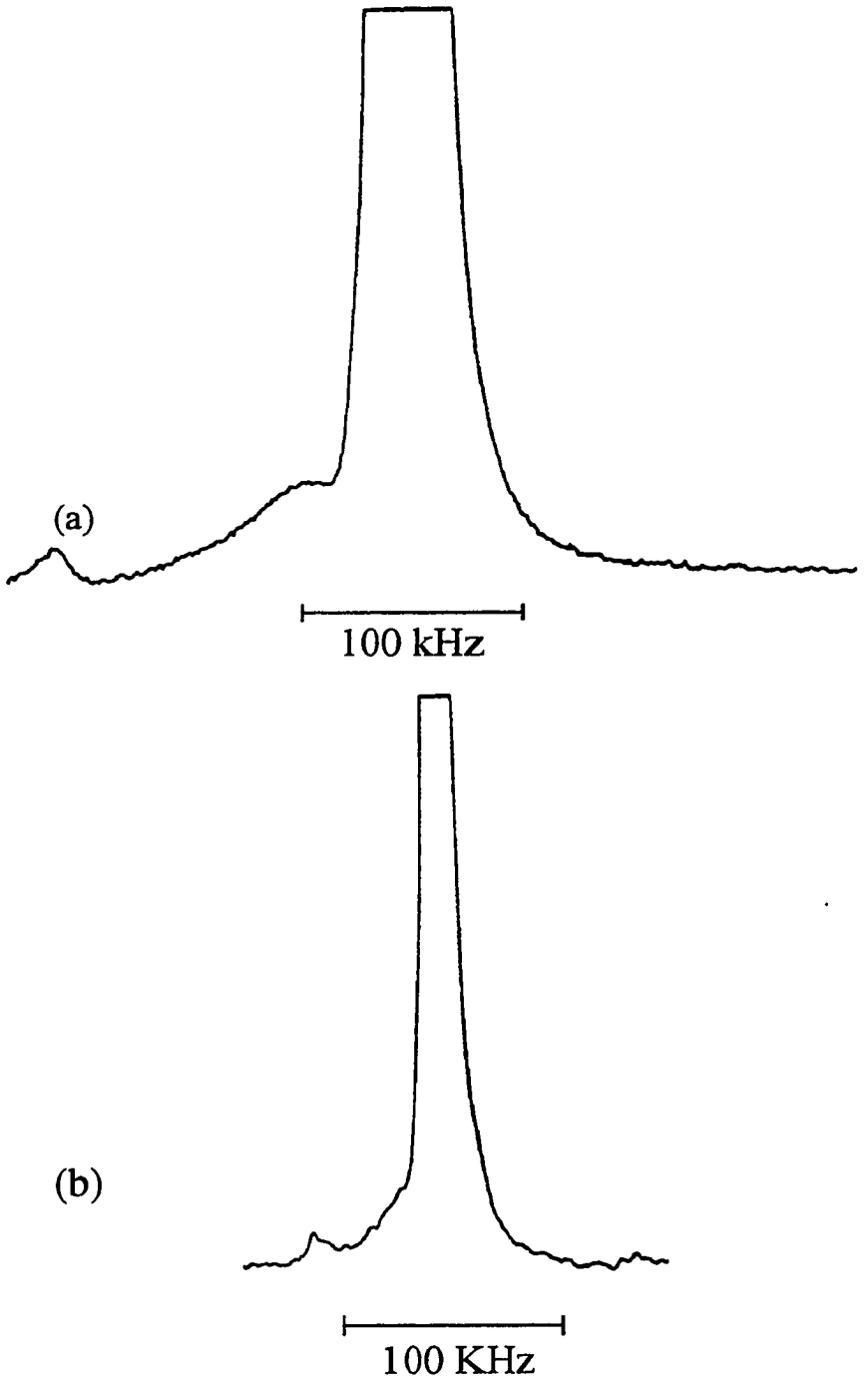

Figure 4-14: Expanded vertical-scale NMR spectra of $Li_{1.35}CoO_2$. (a) Lithium-7; (b) Lithium-6.

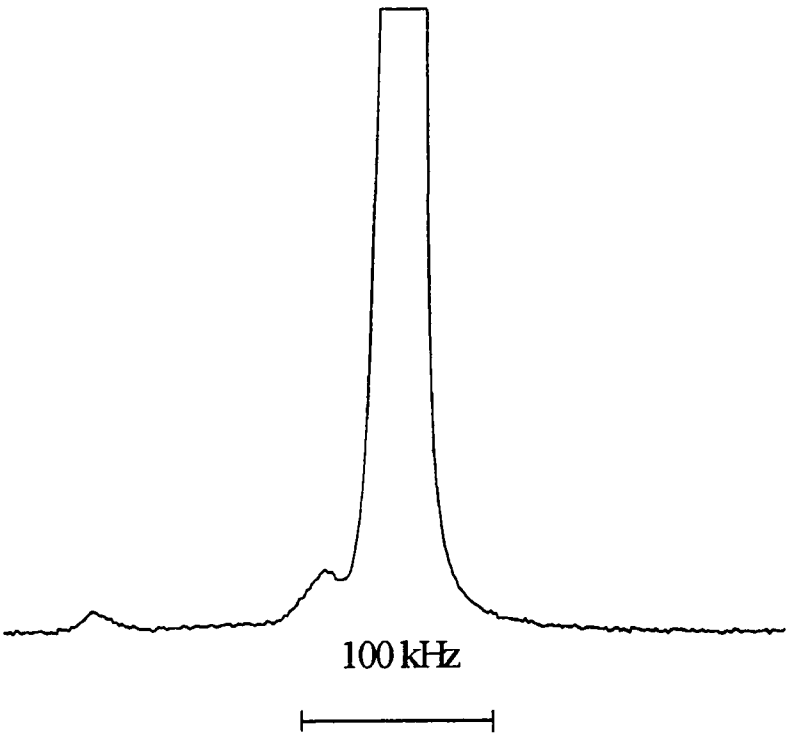

Figure 4-15: Expanded vertical-scale ^{7}Li absorption spectrum of $Li_{1.08}CoO_2$.

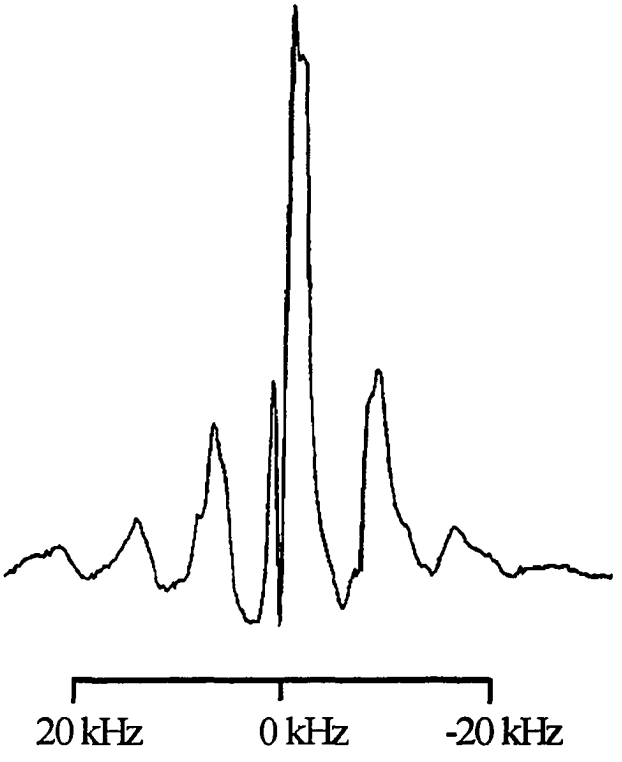

Figure 4-16: Lithium-7 MAS (7 kHz spinning rate) absorption spectrum of $Li_{1.35}CoO_2$ under inversion recovery.

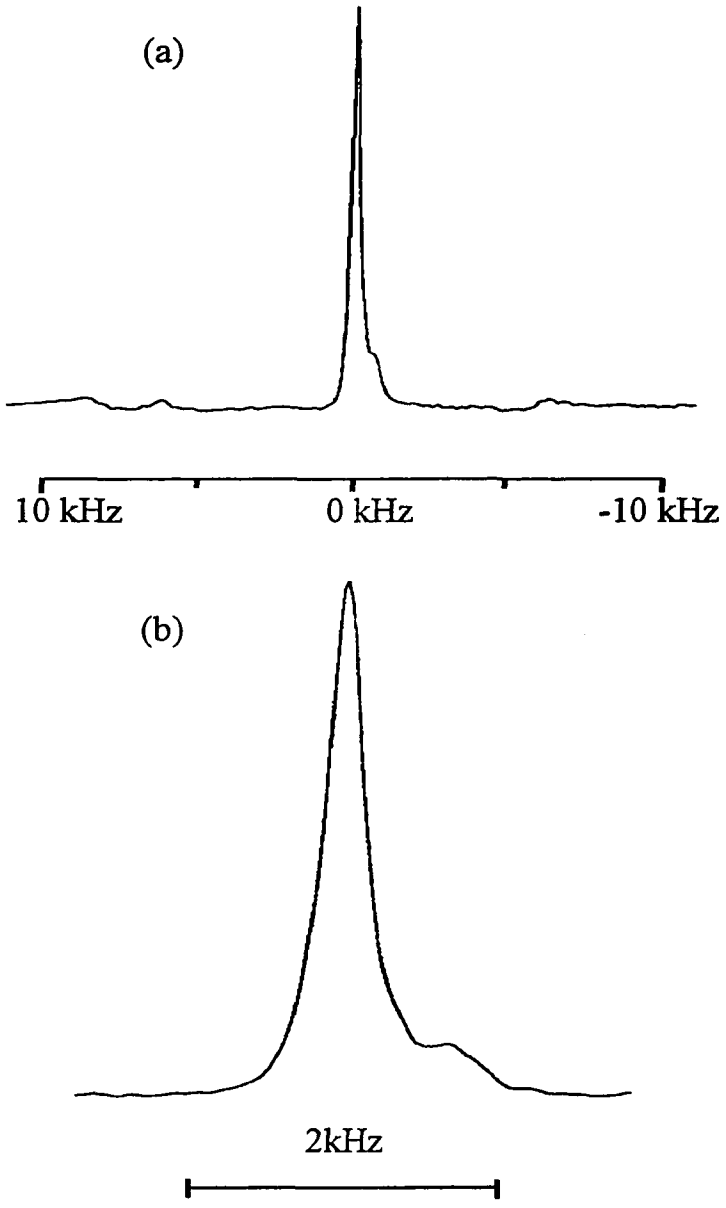

Figure 4-17: (a) Lithium-6 MAS (6 kHz spinning rate) spectrum of $Li_{1.35}CoO_2$. Spinning side-bands appear at ±6 kHz. (b) Same as (a) with expanded horizontal scale.

Table 4-4. Nominal (y) and experimental (y*) lithium content, water soluble lithium, average oxidation state of Co for $Li_{1+y}CoO_2$ and chemical composition.

Y	y*	Soluble Lithium compounds (mol/mol)	Average oxidation state of Co	Composition
0.00	0.00	0.003	3.00	$Li_{1.02}Co_{1.02}O_2$
0.08	0.08	0.003	2.90	$Li_{1.05}Co_{0.97}O_2$
0.35	0.27	0.07	2.85	$Li_{1.13}Co_{0..89}O_2$

The same observation holds for the y = 0.08 sample. This is emphasized additionally by the fact that at least a portion of the extra line width has now been attributed to the 17 ppm diamagnetically shifted component. Again, in studies of Li-deficient $LiCoO_2$ substantially larger line widths and also paramagnetic shifts were observed at 40% deficiency[14]. It is expected that the presence of Co^{3-y} would have similar effects on the NMR results as does Co^{3+y} (that is, Co^{2+} and Co^{4+} are both paramagnetic). It is thus concluded that some of the excess Li (not counting the paramagnetically-shifted sites) resides in the impurity phase already identified (Li_2CoO_3) as well as, possibly, other unidentified compounds which were undetected by the X-ray diffraction characterization. This inference does not bode well for reversibility of the excess Li, which would have signified a cathode material of enhanced capacity, compared to the stoichiometric compound.

The effect of Mg-doping on the ^7Li spectra is shown in **Figures 4-18** and **4-19a**, corresponding to a Li excess of y = 0.08. The spectrum of the y = 0.00 stoichiometric sample, not shown here, is essentially the same as that of **Figure 4-13a** and therefore exhibits no change upon incorporation of Mg. The wide-line spectrum (**Figure 4-18**) has

a ~25% greater line width than the y = 0.08 sample without Mg. The presence of the 300 ppm peak is masked by the breadth of the wide-line spectrum. The line width data for all of the samples at room temperature are summarized in **Table 4-5**.

Table 4-5. Lithium-6 nad –7 line widths (full width at half maximum) of $Li_{1+y}CoO_2$, with and without Mg, at room temperature.

Sample	^{7}Li linewidth (kHz)	^{6}Li linewidth (kHz)
$LiCoO_2$	14.53	4.25
$Li_{1.08}CoO_2$	16.25	5.72
$Li_{1.30}CoO_2$	15.56	4.94
$LiCoO_2$:Mg	14.59	4.00
$Li_{1.08}CoO_2$:Mg	19.27	5.74

Interestingly, the far-field (1380 ppm) low intensity feature observed in all of the other excess Li samples is absent in the Mg-doped one. The 7 kHz MAS ^{7}Li spectrum of $Li_{1.08}CoO_2$:Mg is displayed in **Figure 4-19a**, with the undoped, stoichiometric $LiCoO_2$ spectrum shown for reference in **Figure 4-19b**. Although the MAS reveals the 17 ppm shoulder observed in the other excess Li samples, no other features can be resolved. The central peak and spinning side bands are about 25% wider than in the stoichiometric sample. This extra line width is attributed to paramagnetism of distributed $Co^{2+}$and/or Co^{4+} ions in the structure. An additional source of line broadening in the ^{7}Li spectrum could be envisioned if the Mg substitution were to produce some distortion of the octahedral Li environment which characterizes undoped $LiCoO_2$. The distortion would result in ^{7}Li nuclear quadrupole splittings, leading to observable $\pm 3/2 \rightarrow \pm 1/2$ satellite

transitions. However, evidence for such transitions is lacking, and the interpretation of line broadening from distributed paramagnetic cobalt sites thus remains. As far as the

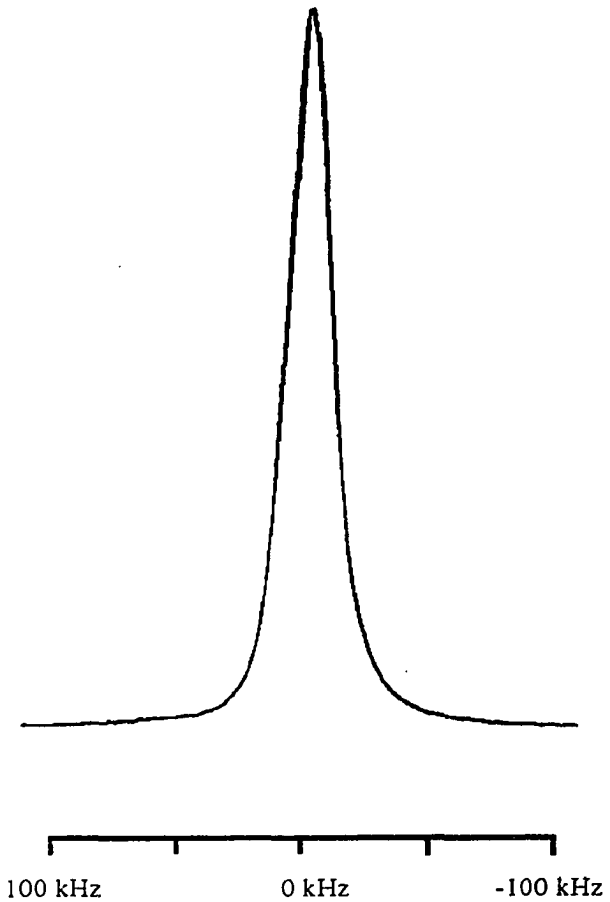

Figure 4-18: Lithium –7 wide line spectrum of $Li_{1.08}CoO_2$:Mg

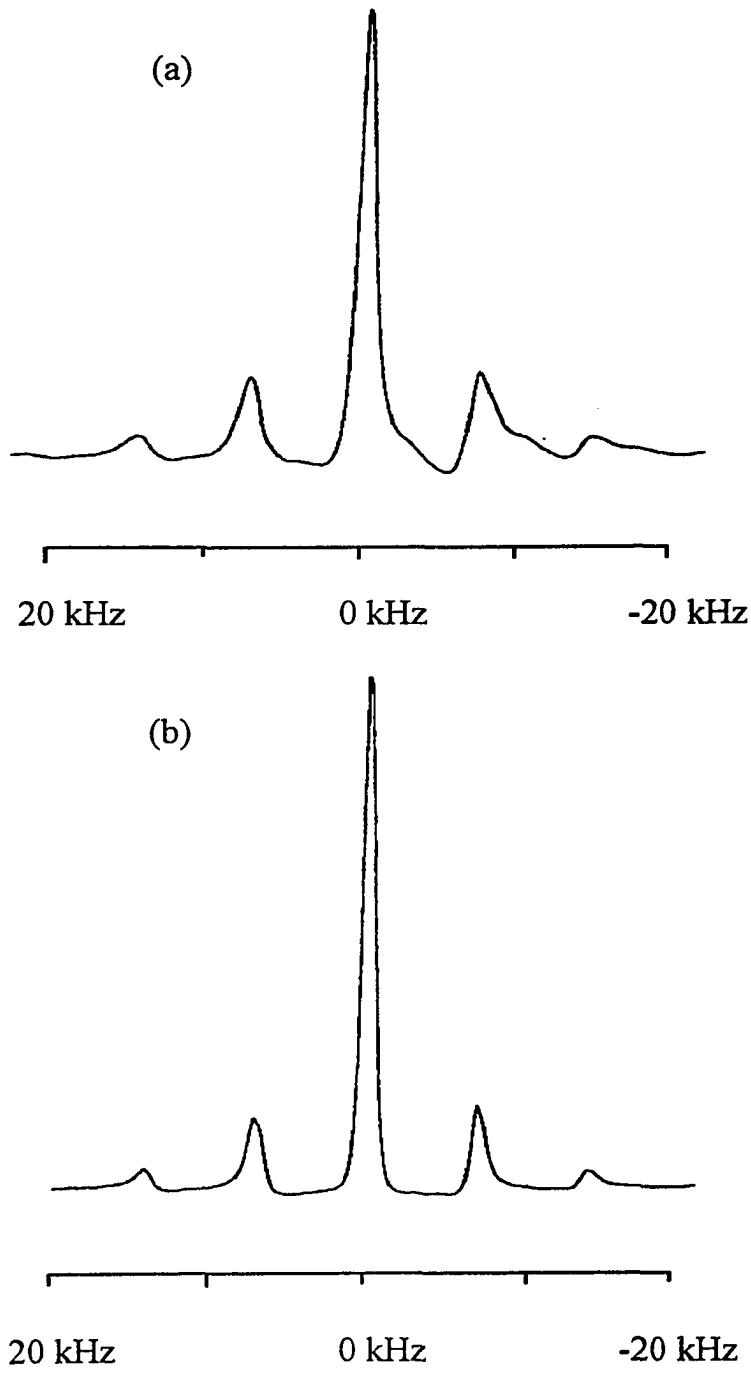

Figure 4-19: Lithium-7 MAS (spinning rate 7 kHz) spectra of (a) $Li_{1.08}CoO_2$:Mg; (b) stoichiometric $LiCoO_2$.

NMR results are concerned, the effect of Mg doping of the excess Li sample is either to generate Co^{4+} ions or to increase the efficiency with which the excess Li enters the structure ionically while reducing the Co valence (i.e. generate Co^{2+} ions - the original intention of incorporating excess Li). The mechanism by which the latter might be achieved is unknown at this time.

4-3.3. Sub-conclusions

Solid state NMR measurements show that a small amount of Li (about 10% of the excess) occupies sites, perhaps some of them interstitial, in close proximity to Co^{2+} ions, while the majority of the excess Li forms ionic impurity compounds. A small amount of the excess Li (< 20 % of the excess) may enter the structure ionically with a corresponding reduction of the Co valence. This process appears to be facilitated by the deliberate incorporation of Mg.

Summarizing the above discussion, it is concluded that a fairly small part of excess Li causes the change of Co valence($Co^{3+} \rightarrow Co^{2+}$), and some of the excess Li ions might be located near these paramagnetic Co ions. Excess Li is randomly added into parent structure y=0 so that the structure can be deformed randomly. Thus there is an inhomogeneity of local environments about the Li^{+} ions. The inhomogeneity can increase the line width by quadrupole interactions or by forcing the Co, which is the only element with changeable valence in the sample system, to change its valence from +3 to +2, the latter being paramagnetic.

4-4. $LiCo_xNi_{1-x}O_2$

(Samples provided by Dr. P. Kumta, Carnegie Mellon Unversity)

4-4.1. Sample background[90]

The lithiated nickel oxide based cathode materials containing stoichiometric and excess lithium was synthesized using a low temperature colloidal particulate sol-gel process. The process yields a xerogel precursor that transforms to the crystalline oxide at 800 °C in 2 hours. ^{7}Li NMR measurements of the organic precursor, $LiNiO_2$, $LiNiO_2$ with 5% excess Li, $LiCo_{1/4}Ni_{3/4}O_2$, and $LiCo_{1/4}Ni_{3/4}O_2$ with 5% excess Li were conducted by quadrupole echo sequence. Aqueous LiCl solution was employed as chemical shift reference.

4-4.2. Experimental results and discussions

The ^{7}Li NMR line-widths with variable temperatures for Li-Co-Ni-O series are displayed in **Figure 4-20, 21.** From **Figure 4-20**, a dramatic change is found in the $LiNiO_2$ precursor upon heating. The ^{7}Li line width reaches a minimum around 100°C. This indicates that some chemical reaction takes place above 100°C, consistent with the idea that the precursor must be heated to form $LiNiO_2$. Subsequent broadening above 100 °C is attributed to formation of Ni^{3+} characteristic of the final structure. The line widths of the other samples are replotted in Arrhenius format (See **Figure 4-22**). From regression lines, it is concluded that these samples are strongly paramagnetic systems because $\Delta\nu \propto 1/T$ [14]. Room temperature T_1 results for the sample series are listed in the **Table 4-6**. The presence of excess Li has a greater effect on the T_1 of $LiNiO_2$ than on

$LiCo_{1/4}Ni_{3/4}O_2$. The absolute difference of T_1 is 2.6ms for Li-Ni-O system and is 0.5ms for Li-Co-Ni-O system. We can say that the influence

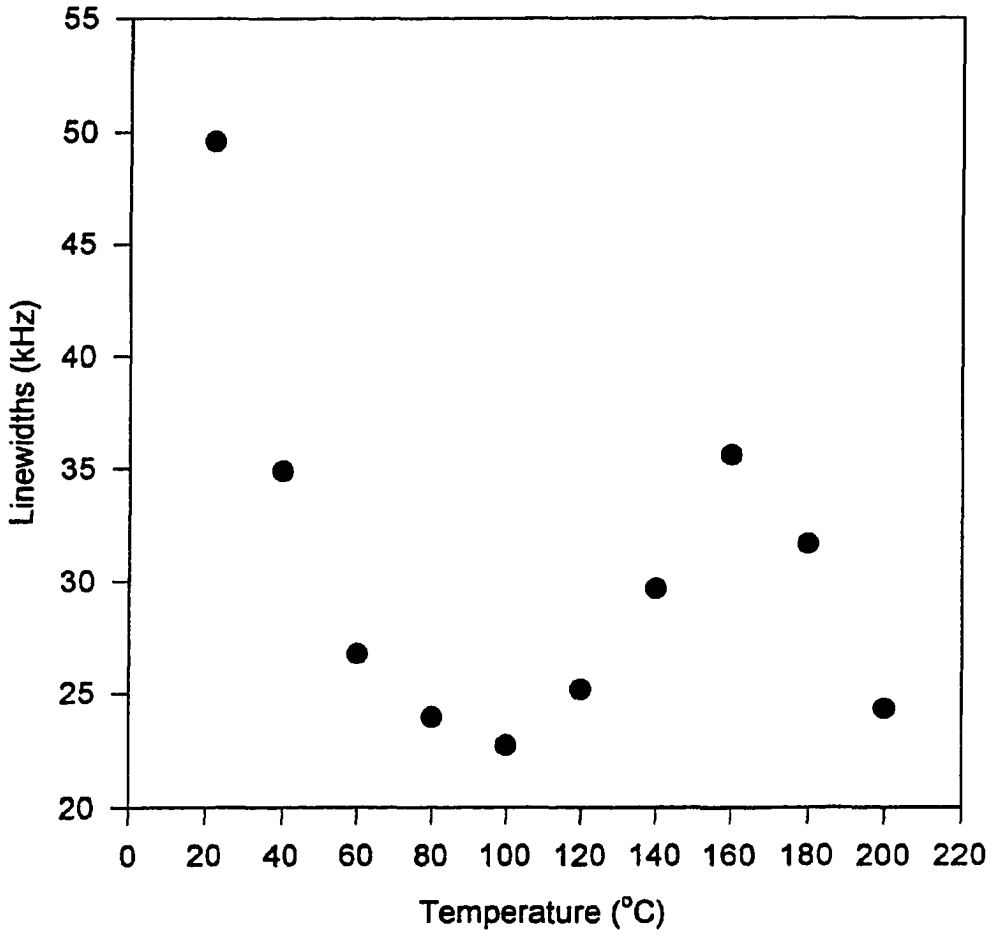

Figure 4-20: Line widths with temperature for $LiNiO_2$ (precursors).

of excess Li on T_1 in Li-Ni-O system is greater than that in Li-Co-Ni-O. The presence of 5% excess Li causes almost no change in NMR line width or T_1 in mixed (Ni/Co) cathode, but does produce an almost 30% reduction in line width for the pure $LiNiO_2$. The change in magnetic environment about the Li ions is correlated with effective Ni valence change measured by x-ray absorption spectroscopy[90]. Although the strong interaction between Li and the paramagnetic Ni^{3+} dominates the behavior of the 6,7Li line widths and T_1 among the samples, more subtle changes observed here imply that excess Li incorporation and Co-alloying have similar effects on the Li environment. In fact, both strategies yield significant improvement in electrochemical stability of $LiNiO_2$.

Table 4-6 The spin lattice relaxation time T_1 of sample system $LiCo_xNi_{1-x}O_2$

Sample Name	T_1(ms)
$LiNiO_2$(precursor)	5.48
$LiNiO_2$	3.44
$LiNiO_2$(5% excess Li)	6.04
$LiCo_{1/4}Ni_{3/4}O_2$	5.65
$LiCo_{1/4}Ni_{3/4}O_2$(5% excess Li)	5.40

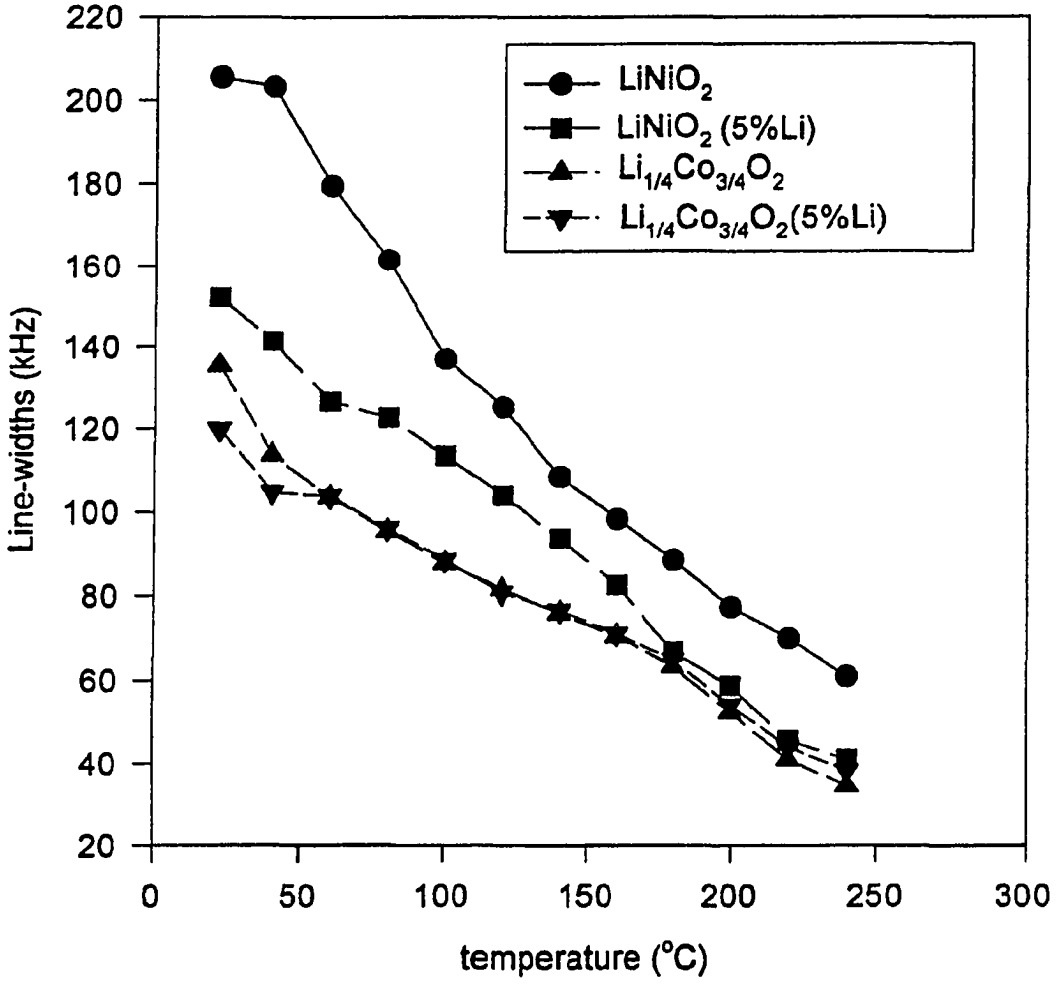

Figure 4-21: Line widths with temperatures for $LiNiO_2$, $LiNiO_2$ (5% excess Li), $LiCo_{1/4}Ni_{3/4}O_2$, and $LiCo_{1/4}Ni_{3/4}O_2$(5% excess Li).

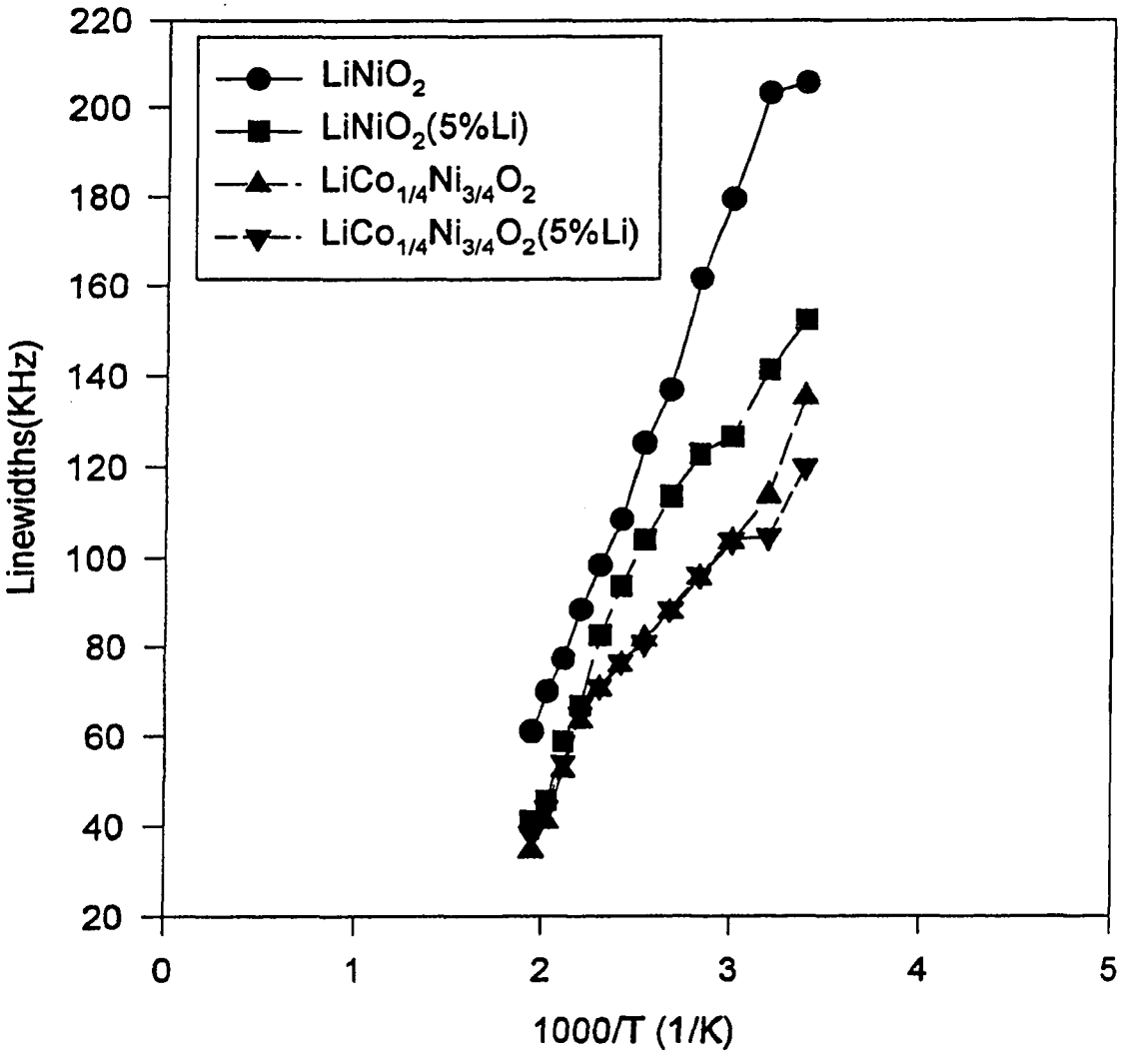

Figure 4-22: Line widths vs. the inversion of temperatures.

4-5. $Li(Cr,Fe)_xMn_{2-x}O_4$

(provided by Dr.D.Fauteux, Arthur D.Little. Inc., now Hirion Electrochemical, Inc.)

4-5.1. Experimental results and discussions

Since the "dead time" problem affects the measurement, the echo pulse sequence (90x' - τ - 90y' - echo) was employed to acquire spectra. The NMR reference is aqueous LiCl. **Table 4-7** summarizes the ^7Li line widths and chemical shifts of the sample series, and **Table 4-8** summarizes the ^6Li line widths and chemical shifts of the sample series.

Table 4-7. The ^7Li line widths and chemical shifts of the sample series: $Li(Cr,Fe)_xMn_{2-x}O_4$ (x=0.0, 0.4 and 1.0)

Sample Name	$\omega_{1/2}$(kHz)	Shift(kHz)
$LiCr_{0.4}Mn_{1.6}O_4$	127.84	61.51
$LiMn_2O_4$	149.20	57.42
$LiFe_{0.4}Mn_{1.6}O_4$	157.07	48.75

Table 4-8. ^6Li line **Figure 3-7** shows a typical MAS spectrum. widths (FWHM) and chemical shifts of $Li(Cr,Fe)_xMn_{2-x}O_4$

Sample Name	$\omega_{1/2}$(kHz)	Shift(kHz)
$LiCr_{0.4}Mn_{1.6}O_4$	53.30	33.59
$LiMn_2O_4$	59.94	32.37
$LiFe_{0.4}Mn_{1.6}O_4$	69.45	20.59

The sample series have a common character that all have a large concentration of paramagnetic ions. When these ions enter the lattice, a very strong local field will act on the NMR nuclei. The d electron number of magnetic element (Cr,Mn,Fe) should play an important role in NMR spectra. For simplifying the discussion, the nominal designation

of sample $LiMn_2O_4$ is rewritten to $LiMn_{0.4}\ Mn_{1.6}\ O_4$ to resemble $LiCr_{0.4}\ Mn_{1.6}O_4$ and $LiFe_{0.4}\ Mn_{1.6}O_4$.

Now we are concentrating on the discussion of the roles of substituted $Cr_{0.4}$, $Mn_{0.4}$ and $Fe_{0.4}$. According to the law of substitution in compounds of similar structure, the electro-negativity and ionic radius of the substitutions have to be close to those of the original ones. The Cr, Mn and Fe ions of +3 valence have the radii of 0.615, 0.645 and 0.645[91] A respectively, which are quite close to each other. On the other hand, even with a same element such as Mn, different valence has much different radius. We also know that Cr^{3+}, Mn^{3+} and Fe^{3+} have $3d^4$, $3d^5$ and $3d^6$ electrons, respectively. Based on the above facts, the trend (Table 4-7), which is linewidths and chemical shifts with the order of paramagnetic Cr^{3+}, Mn^{3+} and Fe^{3+} ions, shows that there exists complex interactions between Li^+ and the paramagnetic ions. Table 4-8 shows that the chemical shift decreases as the d-shell is filled, from $3d^4$ to $3d^6$. However, counter to this trend, the linewidth increases, Thus both of these measurements give apparently the conflicting views regarding the magnitude of the local magnetic field at the Li^+ site. No further explanation for this unusual result is given at this time.

Summarizing the above discussions, it is concluded that the magnetic ion substitutions greatly change the local magnetic field and possibly the structural environment on Li^+ sites. They result in complex behavior of linewidths and chemical shifts.

4-6. LiI/Al_2O_3 mixtures

(Provided by Gilat Ardel, Dina Golodnitsky and Emanuel Peled, Tel Aviv University)

4-6.1. Sample background and experiments[92]

The solid electrolytes were prepared in an argon glove box (< 10-ppm water) from commercially available starting materials, which were vacuum dried prior to use. The LiI (Aldrich) was dissolved in acetonitrile, dried in the argon atmosphere of the glove box and then vacuum dried at 160 °C for about 6 hours. The Al_2O_3 powder (Buehler) has an average particle diameter of 15 nm. Two methods of preparation of the LiI/Al_2O_3 solid electrolytes containing 0 to 50% w/w Al_2O_3 were used. The first one, denoted as "Series A", was made by hand milling of dry powders and pressing pellets (inside glove box) at 4 ton/cm^2. For the second type of LiI/Al_2O_3 solid electrolytes, denoted as "Series B", the starting powders were mixed in acetonitrile in appropriate amounts, ground together as a slurry and vacuum dried at 120°C for about 5 hours, prior to pressing into pellets. In NMR measurements, approximately 300 - 500mg of each sample was packed into 5mm OD Pyrex tubes and sealed under vacuum with Torrseal. The Pyrex tubes were then fitted with Teflon sleeves and inserted into 7.5 mm ID NMR rotors for MAS measurements. Both wide-line and MAS techniques were employed for NMR measurements. The spinning rate was from 5 to 6 kHz for the latter. In measurements, a single excitation pulse was utilized. The typical pulse width was 4 μs. An inversion recovery pulse sequence was utilized for the T_1 measurements. Aqueous

LiCl and LiI solutions were employed as chemical shift reference for ^{7}Li and ^{127}I NMR, respectively. The resonance frequency of ^{7}Li was 117 MHz and ^{127}I was 60.3 MHz.

4-6.2. Experimental results and discussions

Wide line ^{7}Li NMR spectra, obtained at 23 °C, of three LiI/Al_2O_3 (70/30, 60/40 and 50/50 ratios) from "series A" are displayed **Figure 4-23**. The spectra are qualitatively similar, although the 50/50 sample exhibits a somewhat narrower line, due to partial averaging attributed to a significant mobile fraction of Li^+ ions. In some case it is possible to observe the coexistence of broad and narrow lines, as reported in reference [40]. Because LiI has a cubic structure, the electric field gradient, and hence the nuclear quadrupole interaction at the Li site, vanishes. Even as the symmetry about the Li^+ ions might be expected to change due to interactions with the surface of the Al_2O_3 particles, there is no evidence, in fact, of quadrupole broadening in the mixtures. Therefore the principal sources of line broadening are magnetic dipole - dipole (^{7}Li – ^{7}Li and ^{7}Li - ^{127}I) interaction, which are partially averaged as the temperature or the Al_2O_3 fraction increases. In order to glean additional evidence about the Li^+ environment in these materials, it is necessary to employ high resolution (MAS) methods. **Figure 4-24, 25 and 26** show variable temperature ^{7}Li MAS NMR spectra of the same three samples as shown in **Figure 4-23**. In **Figure 4-24**, a room temperature spectrum of pure LiI is included as a reference which, itself, is shifted about -0.5 kHz (4.3 ppm) from the aqueous LiCl reference. At all temperature for all samples studied, a major spectral component remains at the pure LiI reference position, which is indicative of bulk-like LiI in the mixture. All

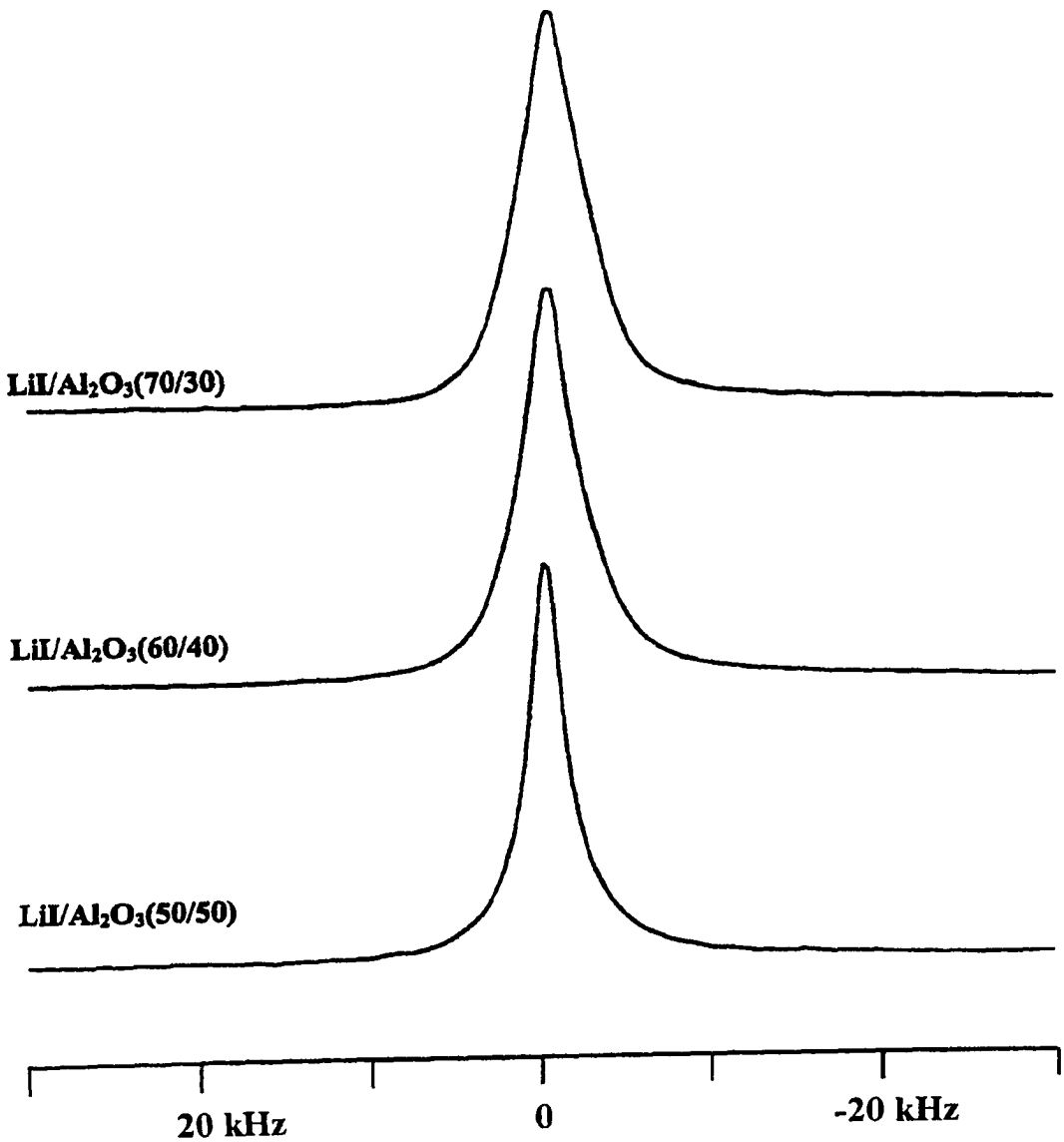

Figure 4-23: Lithium-7 wide-line NMR spectra of Series A samples, at 23°C.

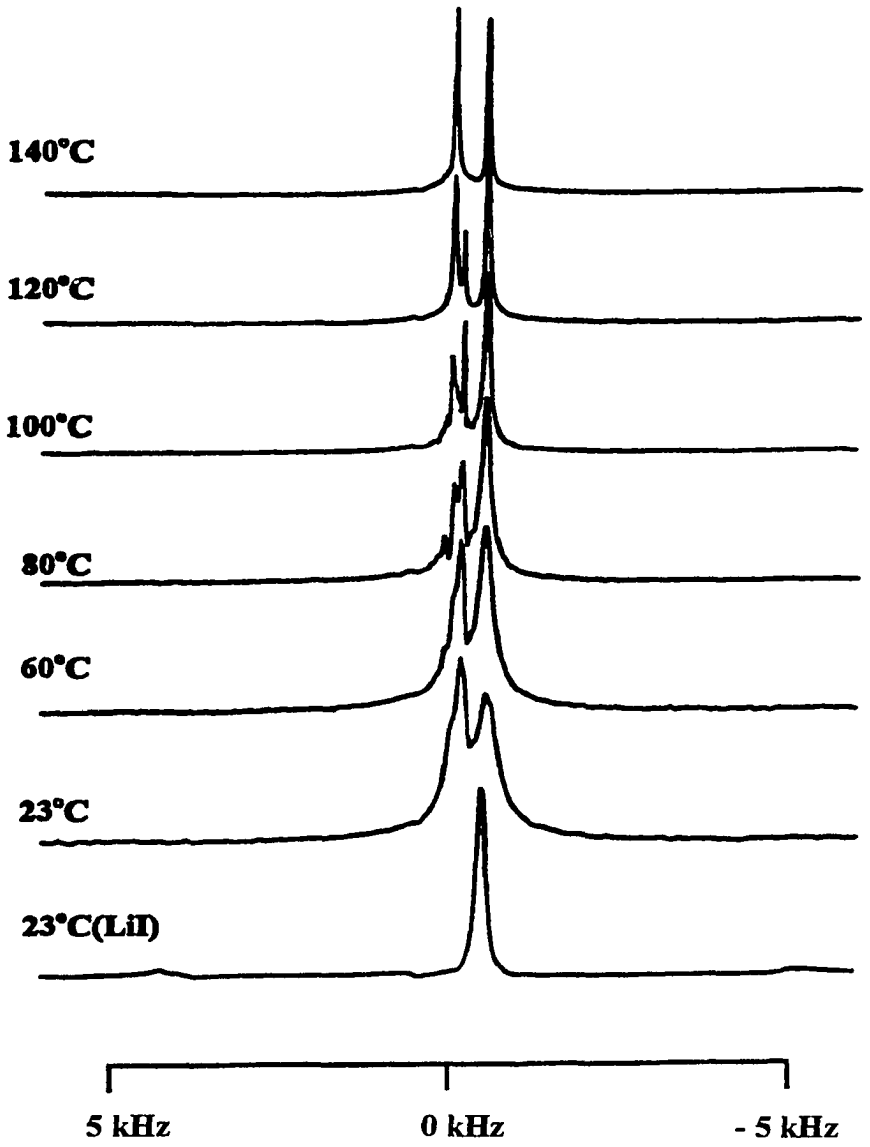

Figure 4-24: Variable temperature ^{7}Li MAS NMR spectra of Series A LiI/Al_2O_3 sample (50/50).

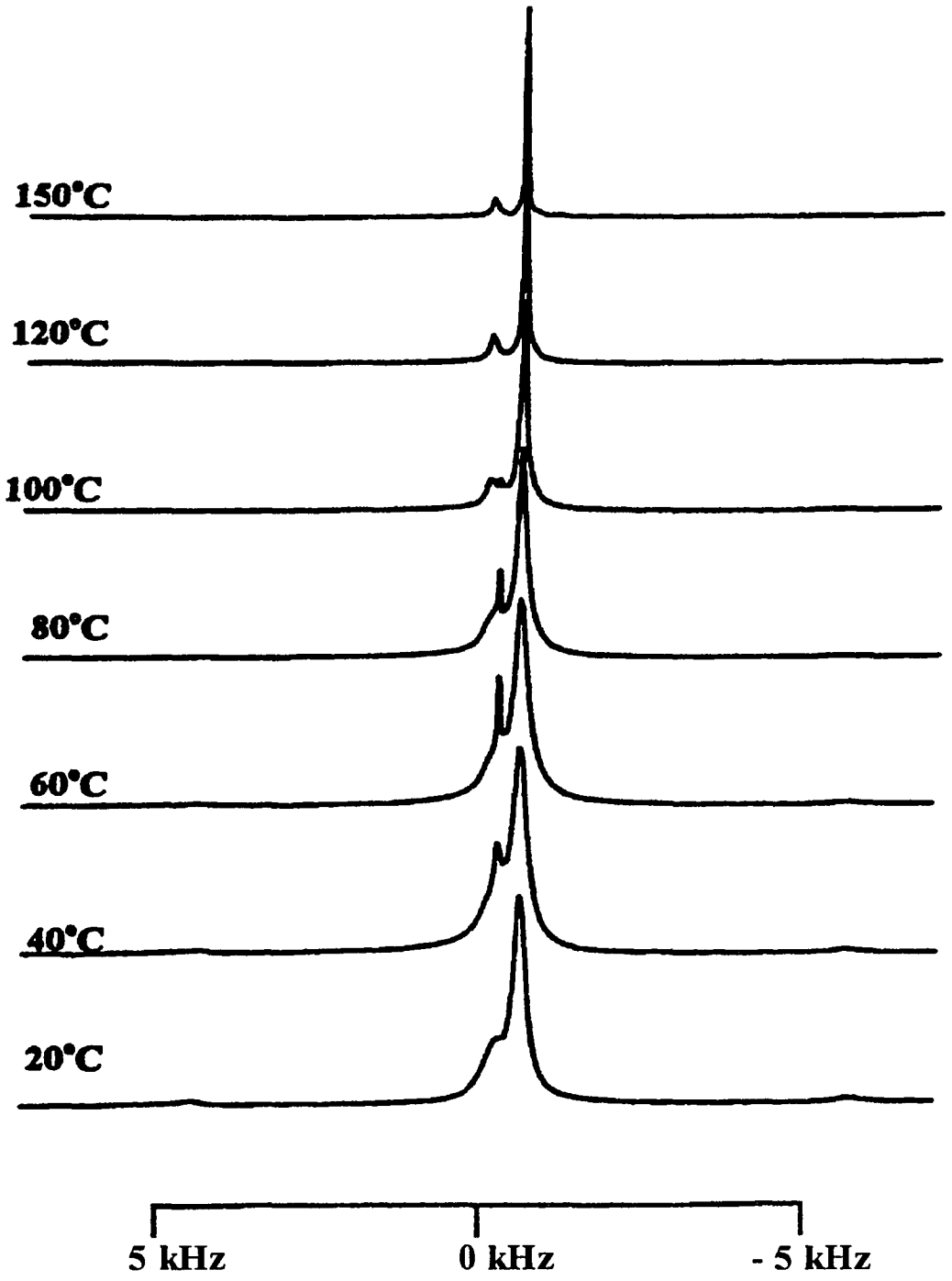

Figure 4-25: Variable temperature ^{7}Li MAS spectra of Series A LiI/Al_2O_3 sample (60/40).

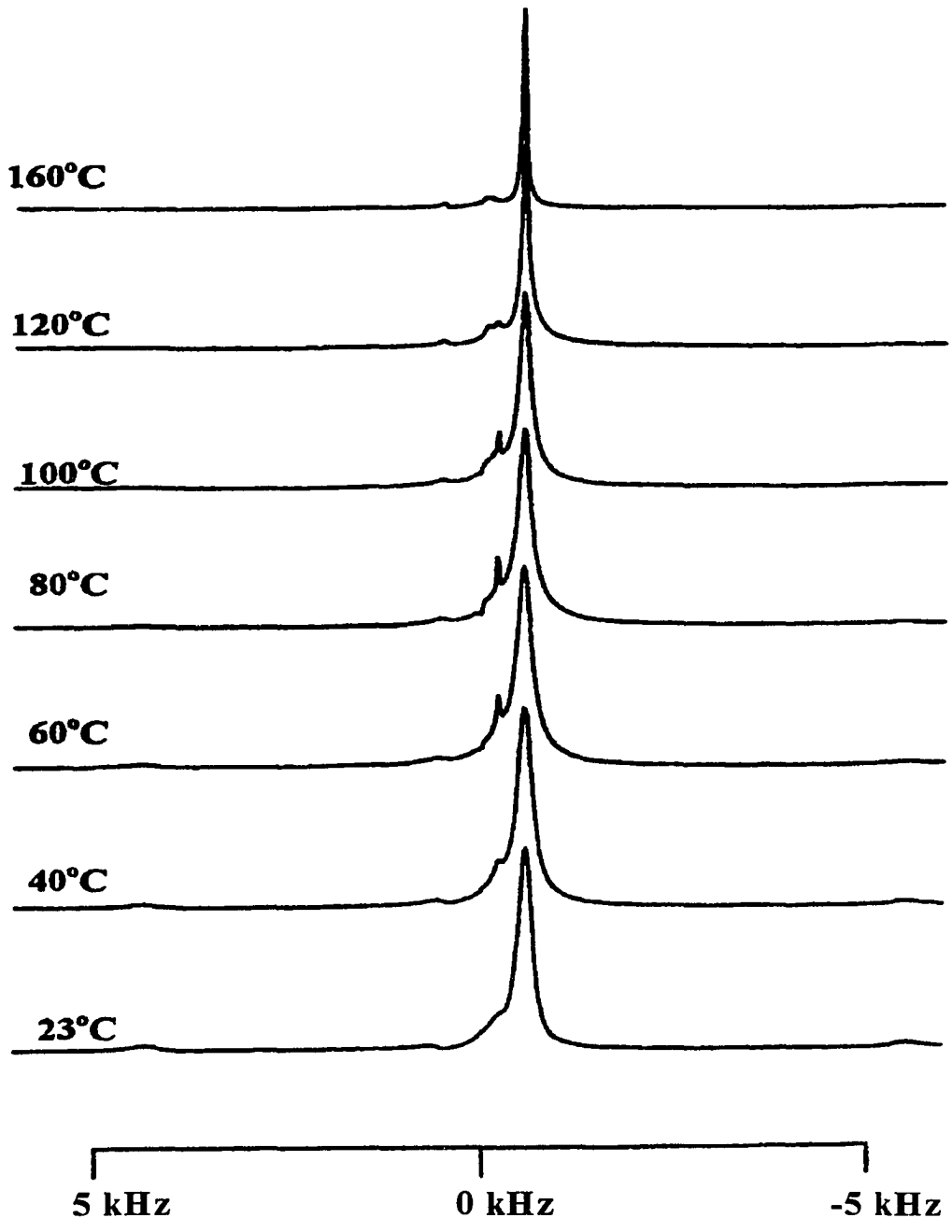

Figure 4-26: Variable temperature ^{7}Li MAS NMR spectra of Series A LiI/Al_2O_3 sample (70/30).

samples exhibit at least two inequivalent Li sites, as evidenced by two or more NMR lines with different chemical shifts. The chemical shift is apparently sensitive to interaction between the Li^+ ions and oxygen atoms on the surface of the Al_2O_3 particles. This effect is particularly dramatic in the case of the 50/50 mixture, which shows as many as four distinct lines 80°C. At 140°C, the 50/50 sample exhibits only two sites, one characteristic of bulk LiI and one appearing approximately at the "ionic" Li environment reference position (aqueous LiCl). The latter site is therefore attributed to a dynamically disordered Li^+ environment not unlike that of molten salt. Interestingly, similar behavior has been observed in polymer electrolytes based on poly (ethylene oxide), LiI and Al_2O_3, which is undoubtedly a more complex system, where ion solvation by ether oxygens is also present [93]. The latter system will be discussed in more detail later.

Although a specific one to one correspondence between features observed in the conductivity and NMR behavior (i.e. the appearance of a specific site at a certain temperature or composition) is not possible at this time, it is reasonable to suppose that the presence of chemically inequivalent Li^+ whose populations are affected by temperature and Al_2O_3 content is related to the various mobile Li^+ sites that contribute to the total ionic conductivity. It is also clear from the NMR line intensities that, owing to the large surface area of the Al_2O_3 particles, there is a large interfacial region that accounts for a significant fraction of the Li^+ ions. It can be seen that the 50/50 sample of Series A exhibits comparable NMR line intensities of the bulk and non-bulk (interfacial) Li. **Figures 4-27, 28** are a comparison between variable temperature ^7Li MAS spectra for LiI/Al_2O_3 mixtures of Series A and Series B. The latter preparation method results in

NMR behavior more characteristic of bulk LiI than the former method. This outcome is consistent with the lower electrical conductivity of Series B samples.

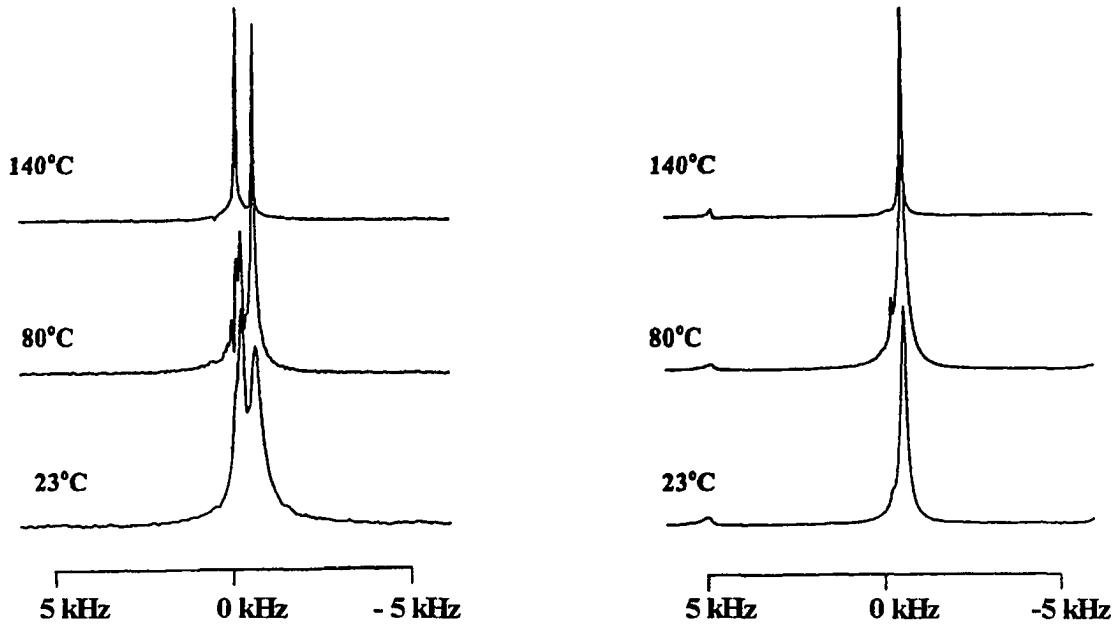

Figure 4-27: Comparison between variable temperature ^{7}Li MAS NMR spectra of Series A and Series B LiI/Al_2O_3 samples: (a) 50/50, Series A – left, Series B – right.

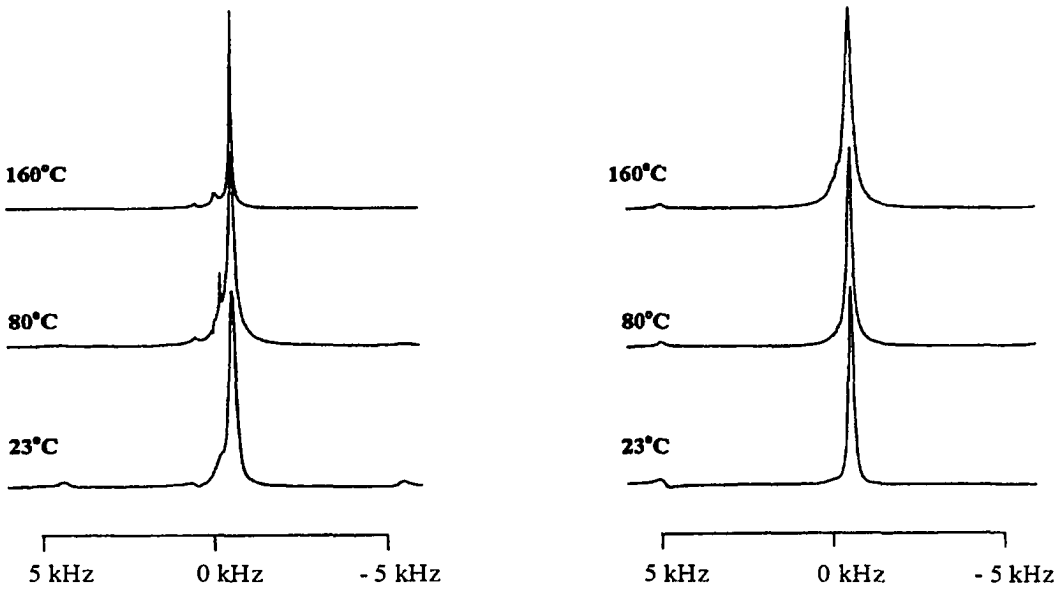

Figure 4-28: Comparison between variable temperature ^{7}Li MAS NMR spectra of Series A and Series B LiI/Al_2O_3 samples: (a) 70/30, Series A – left, Series B – right.

Wide-Line ^{127}I spectra of the 60/40 LiI/Al_2O_3 samples from both Series A and Series B are displayed in **Figure 4-29**, at both room temperature and elevated temperature. The spectra are similar to each other and to that of LiI. The extraordinarily large ^{127}I nuclear quadrupole moment makes this nucleus an extremely sensitive probe of its immediate environment and, in fact, even precludes observation of ^{127}I NMR signals unless the surrounding symmetry is very high, as in the LiI cubic crystal or an I ion in solution. It is therefore concluded that the wide-line response originates from the bulk phase of LiI in the mixed sample. There is however a temperature-dependent chemical shift of approximately 0.28 kHz (about 4.7 ppm) between 23 °C and 140 °C. This shift is comparable to, and even somewhat smaller than, that of pure LiI, which exhibits a shift of 0.46 kHz (7.6 ppm) between 23 °C and 140 °C. High resolution (MAS) spectra corresponding to the wide-line results for Series B in **Figure 4-29** are displayed in **Figure 4-30**. There is apparently no additional information available (besides slightly better resolution of the temperature-dependent shift) from the MAS measurements; i.e. only a single NMR peak is observed at all temperatures. The similarity in high resolution results between the mixture and the pure LiI lends additional evidence that the NMR signal originates primarily from the bulk phase of LiI in the mixture. Additional information regarding dynamic behavior can be obtained from the spin-lattice relaxation time ^{127}I and ^{7}Li measurements. Although the lithium ions are far more mobile than the iodide ions, fluctuations in the local fields about the latter due to motion of the former provide an efficient quadrupole relaxation mechanism. Variable temperature ^{127}I spin-Lattice relaxation time data for all of the LiI/Al_2O_3 mixtures of "Series A" are plotted in **Figure**

4-31. All samples exhibit a shallow T_1 minimum between roughly 25 °C and 45 °C. That the pure LiI ^{127}I T_1 does not show a minimum in the same temperature range as the

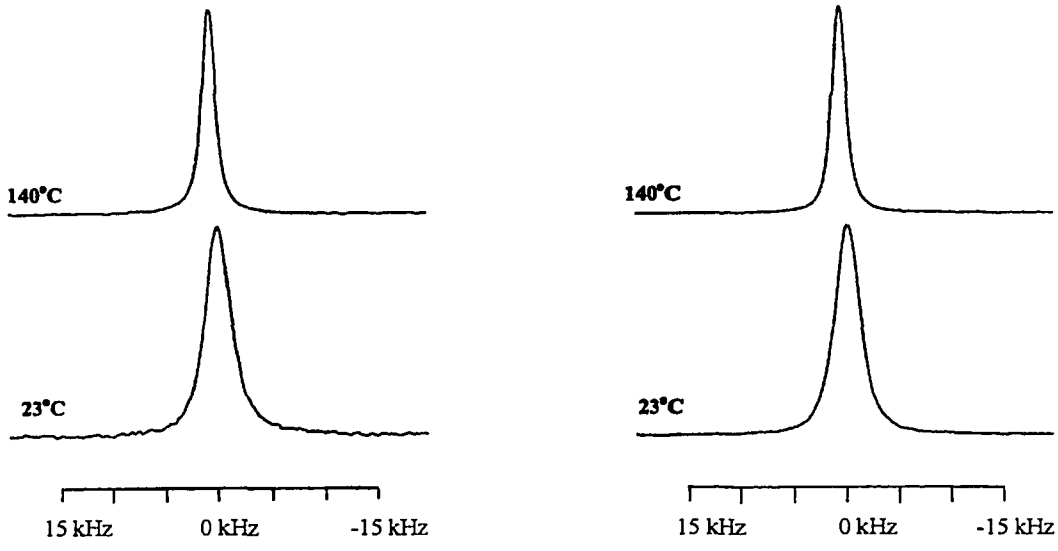

Figure 4-29: Variable temperature ^{127}I wide-line NMR spectra of 60/40 LiI/Al_2O_3, Series A – left, Series B – right.

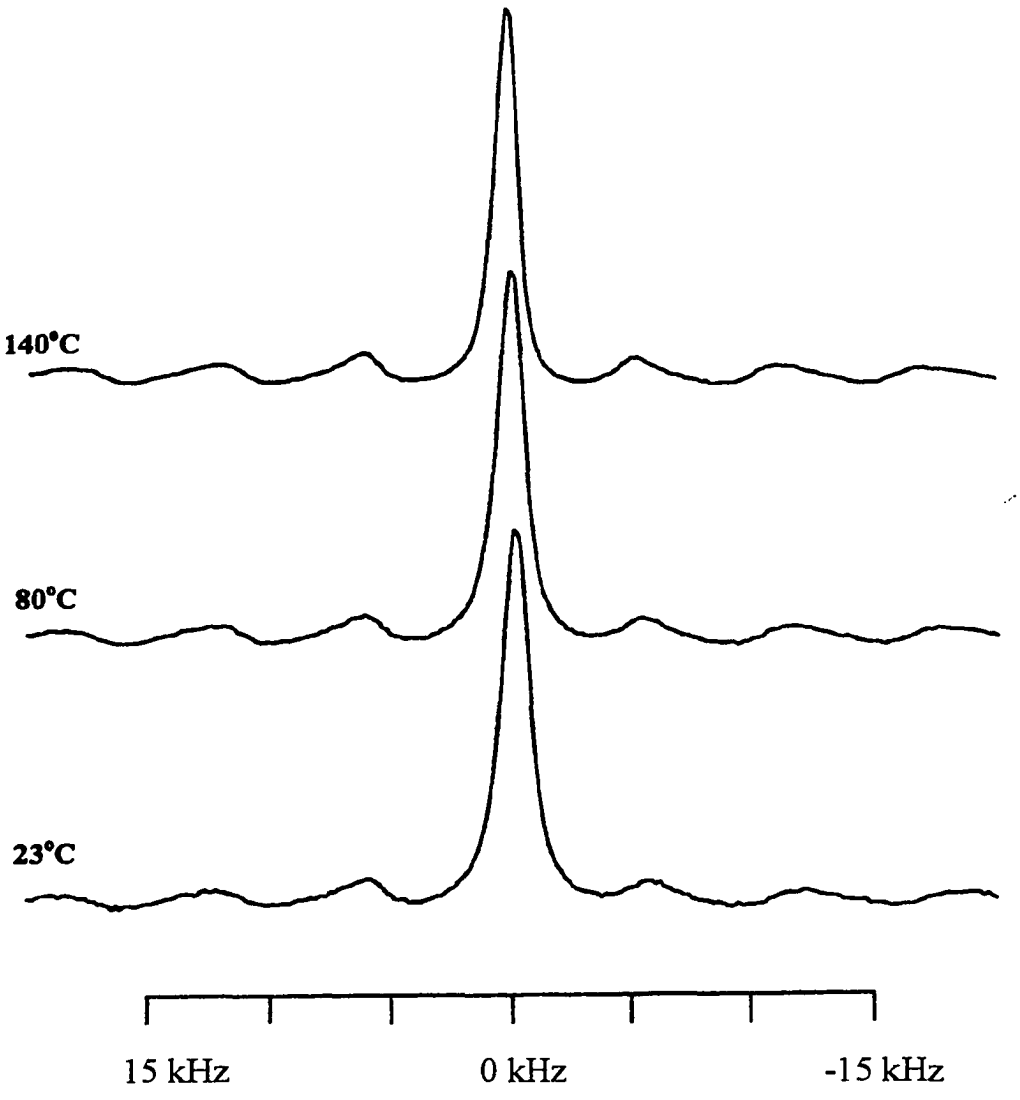

Figure 4-30: Variable temperature ^{127}I MAS NMR spectra of 60/40 LiI/Al_2O_3 Series B sample.

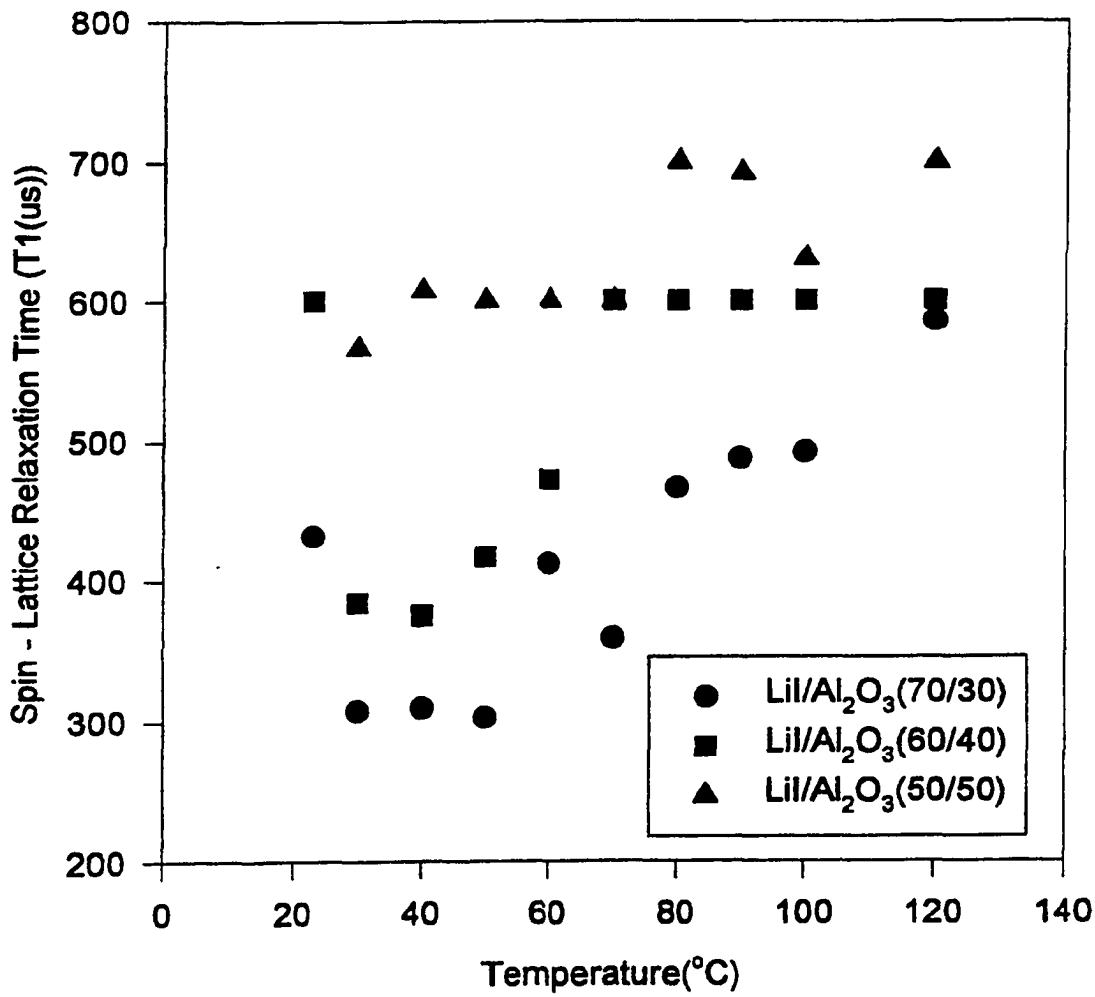

Figure 4-31: Variable temperature ^{127}I spin lattice relaxation time (T_1) of Series A samples.

mixtures indicates that there are dynamical effects, attributable to mobile Li^+ ions, which have a small but discernable influence on the I^- environment. ^7Li spin-lattice relaxation time (T_1) of the peak at –0.5 kHz as a function of Al_2O_3 content (% W/W Al_2O_3/LiI) is displayed in **Figure 4-32**.

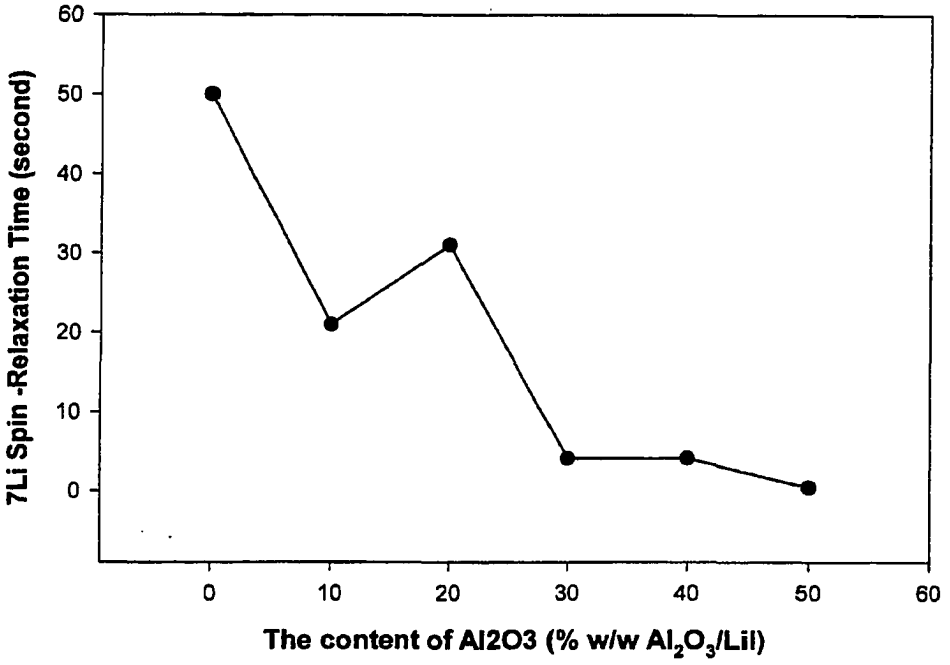

Figure 4-32: ^7Li spin-lattice relaxation of the peak at –0.5 kHz as a function of Al_2O_3 content (% W/W Al_2O_3/LiI).

The most significant change of the T_1 with Al_2O_3 content takes place at about 30% W Al_2O_3. The result indicates that the content of Al_2O_3 greatly affects the mechanism of Li^+ mobility.

To summarize the results, we build up the following pictures:

(LiI/Al_2O_3 70/30)

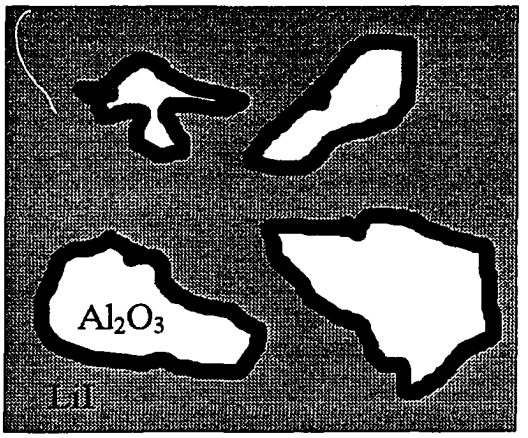

(LiI/Al_2O_3 50/50)

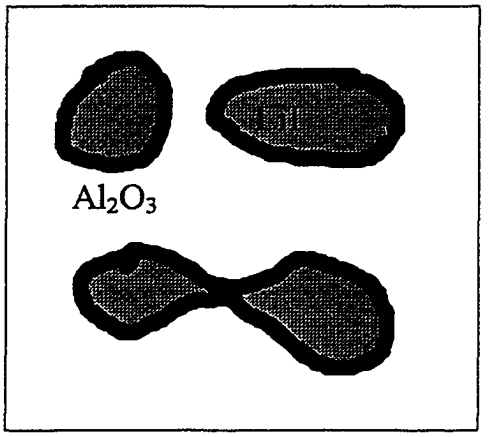

Comparing the two patterns above, the continuum of LiI is easier to form in a LiI-rich sample. In contrast, in an Al_2O_3 rich sample it is easier to form the continuum of Al_2O_3. In other words, there are some "Al_2O_3 islands" in the sample which has a higher content of LiI and some "LiI islands" in sample of higher Al_2O_3 content. There exist interfaces between the LiI and Al_2O_3 phase. With increasing temperature, the Li ions from LiI bulk diffuse into Al_2O_3. This creates Li vacancies at the boundary of LiI bulk. This can greatly modify the behavior of ion conductivity. Based on these arguments the upfield peak is assigned to the Li ions in bulk LiI. As the temperature is increased, the downfield peak is split into several sub-peaks. It appears that the interface between LiI and Al_2O_3 undergoes a chaotic process. The process is ended above 140°C, when the sub peaks merge back to the single interface peak. The intensities of the two peaks are comparable in the 50/50 sample, which indicates that the content of Li ions in the interfacial phase is comparable to that of LiI bulk phase

4-6.3. Sub-conclusions

This investigation has attempted to address the nature of the surface-level interaction between LiI and Al_2O_3 to a greater extent than was done previously. High resolution MAS ^7Li NMR measurements demonstrate the presence of two or more inequivalent sites, which depend on mixture composition as well as temperature. The site populations of Li^+ ions not residing in the bulk LiI phase are comparable to those in the bulk LiI phase at the 50/50 composition at elevated temperature, reflecting the very large effective interfacial region in this material. Iodine-127 NMR measurements, while perhaps not as revealing as ^7Li NMR due the high likelihood that only the bulk LiI phase contributes to the NMR signal, also show dynamical effects associated with mobile Li^+ ions.

4-7. Composite solid electrolytes based on PEO, LiI and high surface area inorganic oxides

(provided samples by D. Golodnitsky et al, Tel Aviv University,)

4-7.1. Sample background and experiments[94]

The composite solid electrolytes (CSEs), which contain poly(ethylene oxide)(PEO) and LiI at high salt concentrations (Li/PEO from 2/3 to 1/9) and high surface area Al_2O_3 or MgO, were prepared from high purity vacuum dried commercial components, according to procedures described elsewhere [95]. Al_2O_3 or MgO powder with average particle diameter of 15 nm was added to the polymer/salt suspension (in acetonitrile) prior to casting and drying. The inorganic oxide content of the samples is reported as volume percentage. All materials were processed under argon in a VAC glove box. The final thickness of films ranged from 50 to 100μm. For ^{7}Li NMR measurement, samples were sealed under Ar in 5mm Pyrex tubes. Both wide-line and high-resolution spectra were obtained under variable conditions, the latter utilizing ^{1}H cross-polarization. decoupling and magic angle spinning (CP/MAS). A typical RF field value in the proton channel was 50 kHz for both CP and decoupling.

4-7.2 Experimental results and discussions

Because of the complicated multi-phase behavior of the materials in this investigation, one does not necessarily expect to find a single transition temperature below which a rigid NMR linewidth is observed (the rigid limit is characterized by molecular motions much slower than the reciprocal of NMR linewidth). The present

samples are generally partially crystalline, and there is evidence for the onset of Li motion below the DSC eutectic melting transition. This is manifested as narrowing of the ^{7}Li NMR signal beginning around 40°C in samples with $(PEO)_3LiI$. Spectra of three different samples at several temperatures are displayed in **Figure 4- 33,34 and 35**. At –20°C, all samples exhibit rigid-limit lineshapes with a broad baseline due to a distribution if ^{7}Li nuclear quadrupole satellite transitions [96]. As the temperature is raised, partial line-narrowing results and most of the spectra in **Figure 4-33, 34 and 35** can be characterized by a superposition of mobile and immobile lithium phases.

The most salt-dilute sample in **Figure 4-33** exhibits the lowest temperature onset of motional narrowing and is effectively completely narrowed at 70°C. This result is due to the effect of the plasticizer(EC/PC) in the relatively dilute electrolyte. The sample in **Figure 4-34** shows partial narrowing even below the eutectic melting point and is almost completely narrowed by 90°C. The most concentrated sample (**Figure 4-35**) exhibits a small but finite mobile component as low as 40°C(spectra for 30 and 50°C only are shown), but retains a rigid phase up to the highest temperature investigated, 110°C(although only 90°C is shown). Additional data regarding Li mobility can be viewed in **Figure 4-36,** which is a plot of ^{7}Li NMR linewidth vs. temperature for several samples. In **Figure 4-36** it is possible to discern the onset of motional narrowing which, again, implies ionic or molecular motion on a timescale comparable to the reciprocal of the linewidth. It is important to point out that the linewidth data are only qualitative because the spectra are generally superpositions of at least two components. The most salt-concentrated sample (n=3/2), which exhibits an immobile phase even at 110°C, shows no evidence of crystalline (or even microcrystalline) LiI, as verified by the absence

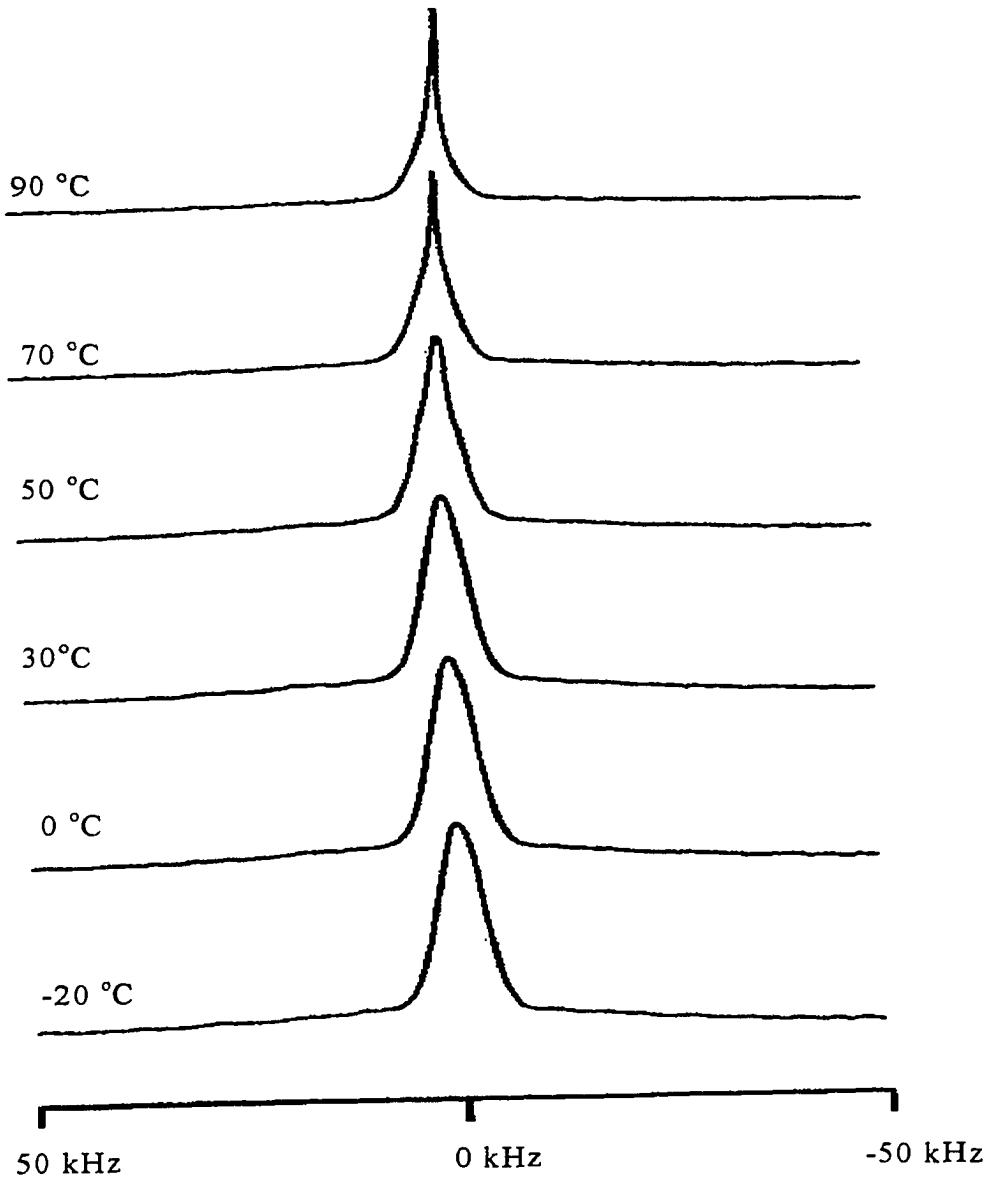

Figure 4-33: Wide-line ^{7}Li NMR spectra of LiI(1)PEO(1.5)+ 6%V/V Al_2O_3 at different temperature.

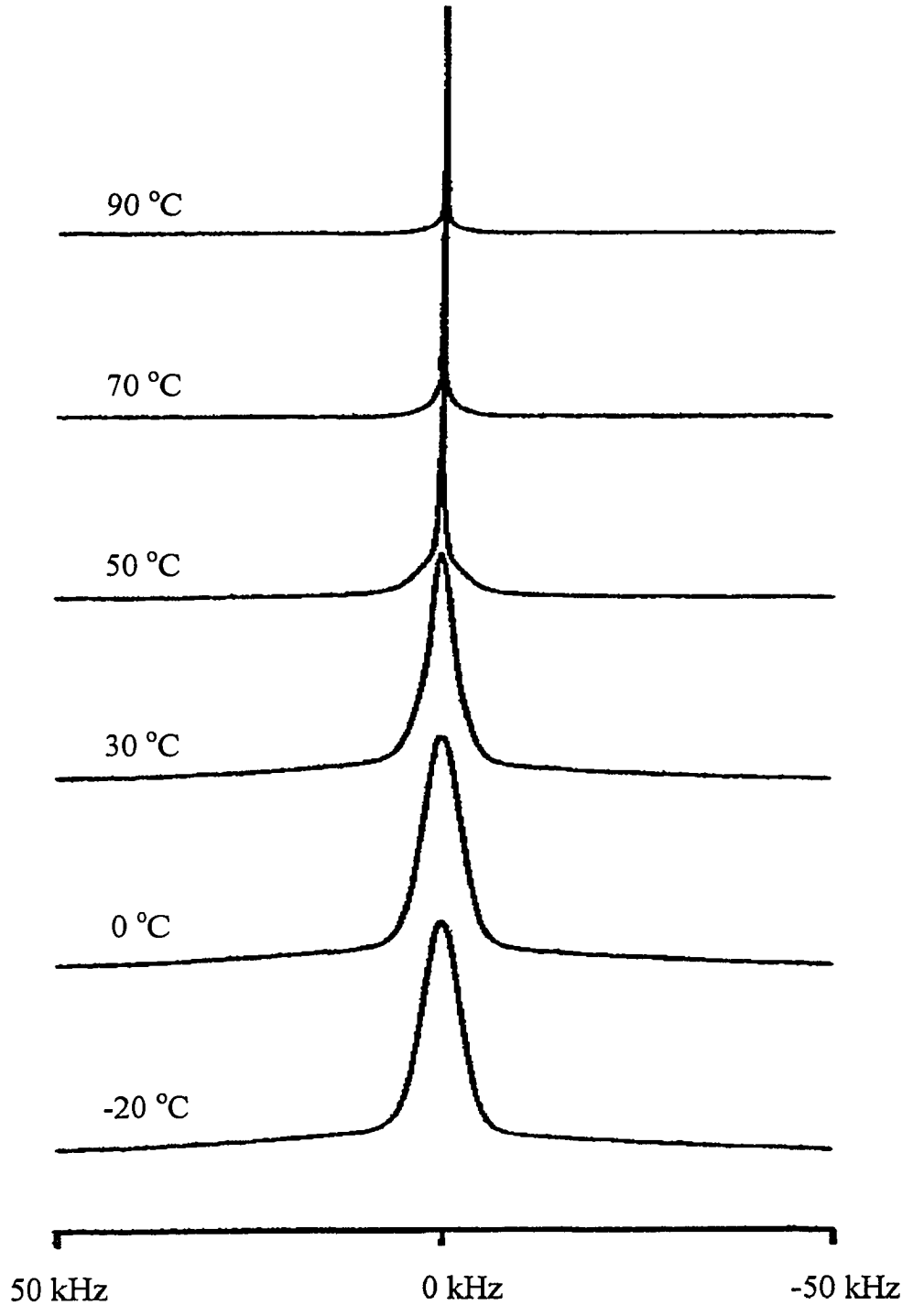

Figure 4-34: Wide-line ^{7}Li NMR spectra of LiI(1)PEO(3)+ 12%V/V Al_2O_3 at different temperature.

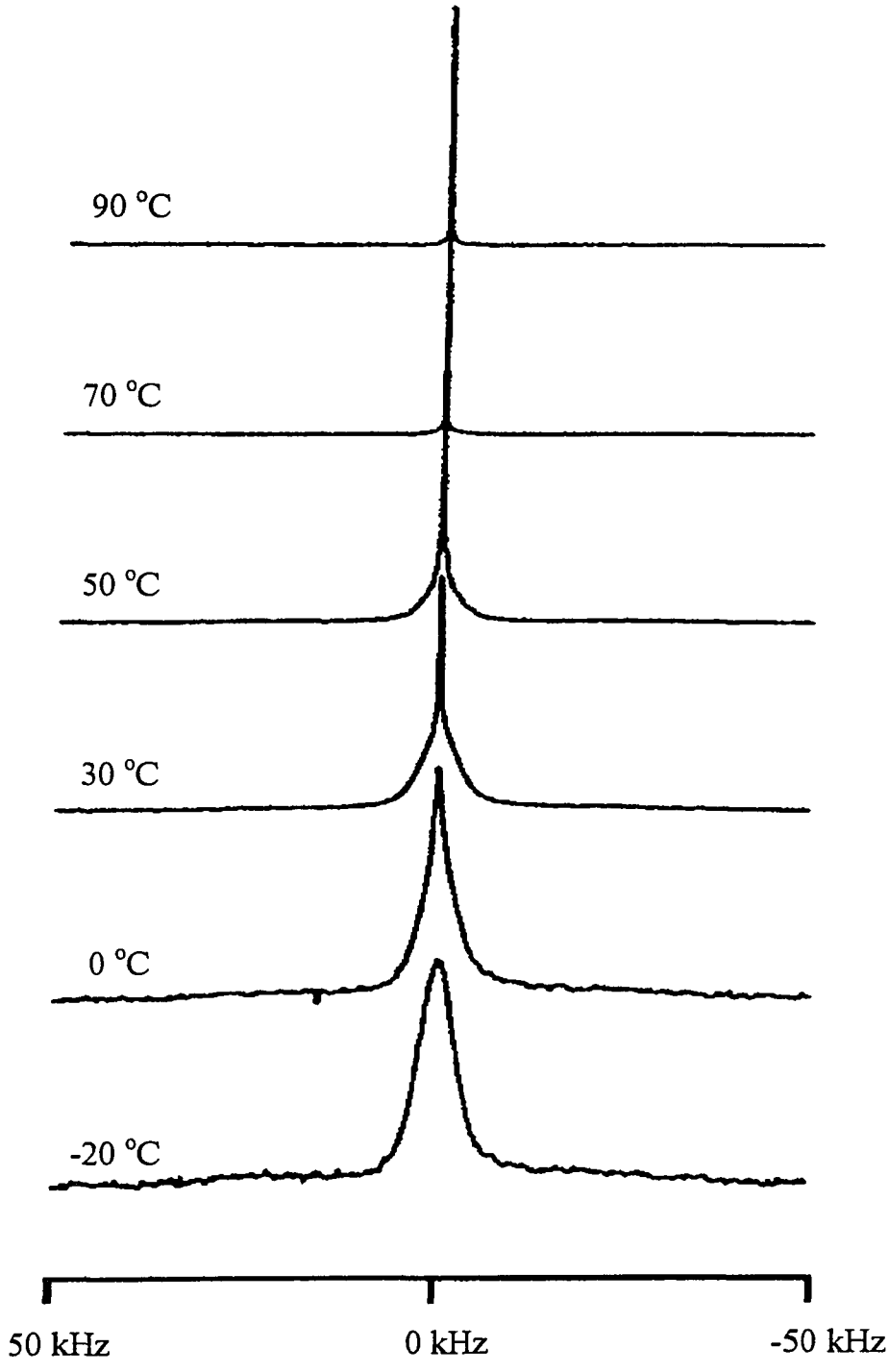

Figure 4-35: Wide-line ^{7}Li NMR spectra of LiI(1)PEO(9)PMMA(1) EC(1) + 6%Al_2O_3 at different temperature.

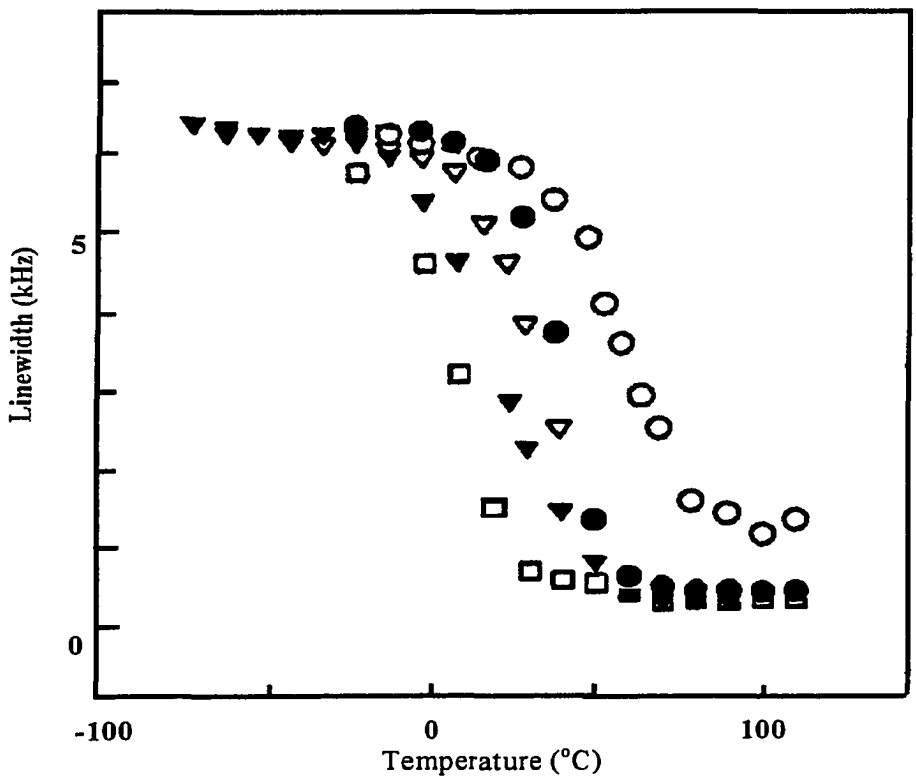

Figure 4-36: Temperature dependence of full width at half height ^7Li linewidth for several CSE samples

of the ^{127}I NMR signal (detectable at the >5% level in our samples, if present). This is consistent with X-ray diffraction results, which failed to detect LiI peaks.

For comparison purposes two of the samples included in **Figure 4-33, 34,35 and 36** LiI (1) PEO (1.5) + Al_2O_3 and LiI (1) PEO (3) EC (1) + Al_2O_3, were also prepared without Al_2O_3. The NMR line widths were observed to be approximately independent of the presence of Al_2O_3[93].

In order to gather additional information regarding the Li ionic environment, beyond the qualitative linewidth results discussed above, high-resolution CP/MAS techniques were employed. High-resolution ^{7}Li spectra are displayed in **Figure 4-37**, for (a) LiI (1) PEO (1.5) + Al2O3 at 23°C; (b) the same sample at 80°C; (c) LiI (1) PEO (9) PMMA (0.5) EC (1) + Al_2O_3 at 23°C. In the frequency range shown in **Figure 4-37**, only the central relatively narrow component is visible; the spinning sidebands appear outside this range. The frequency scale was set at zero corresponding to the position of an aqueous LiCl reference. The spectrum in **Figure 4-37(a)** exhibits two distinct peaks, separated by about 220Hz. The left-hand peak represents Li in a more purely ionic configuration because of its approximately zero chemical shift relative to aqueous LiCl. These clusters are too small to yield identifiable crystalline LiI regions. Furthermore, if this peak were due to segregated regions of LiI, magnetization from protons in the PEO would not be transferred to these nuclei during cross-polarization and this part of the signal would not be observed as strongly as it is. The right-hand peak is somewhat narrower and is attributed to Li solvated by the polyether chains. This assignment is further validated by the sensitivity of this peak to changes in CP parameters. The spectrum in **Figure 4-37(a)** was obtained

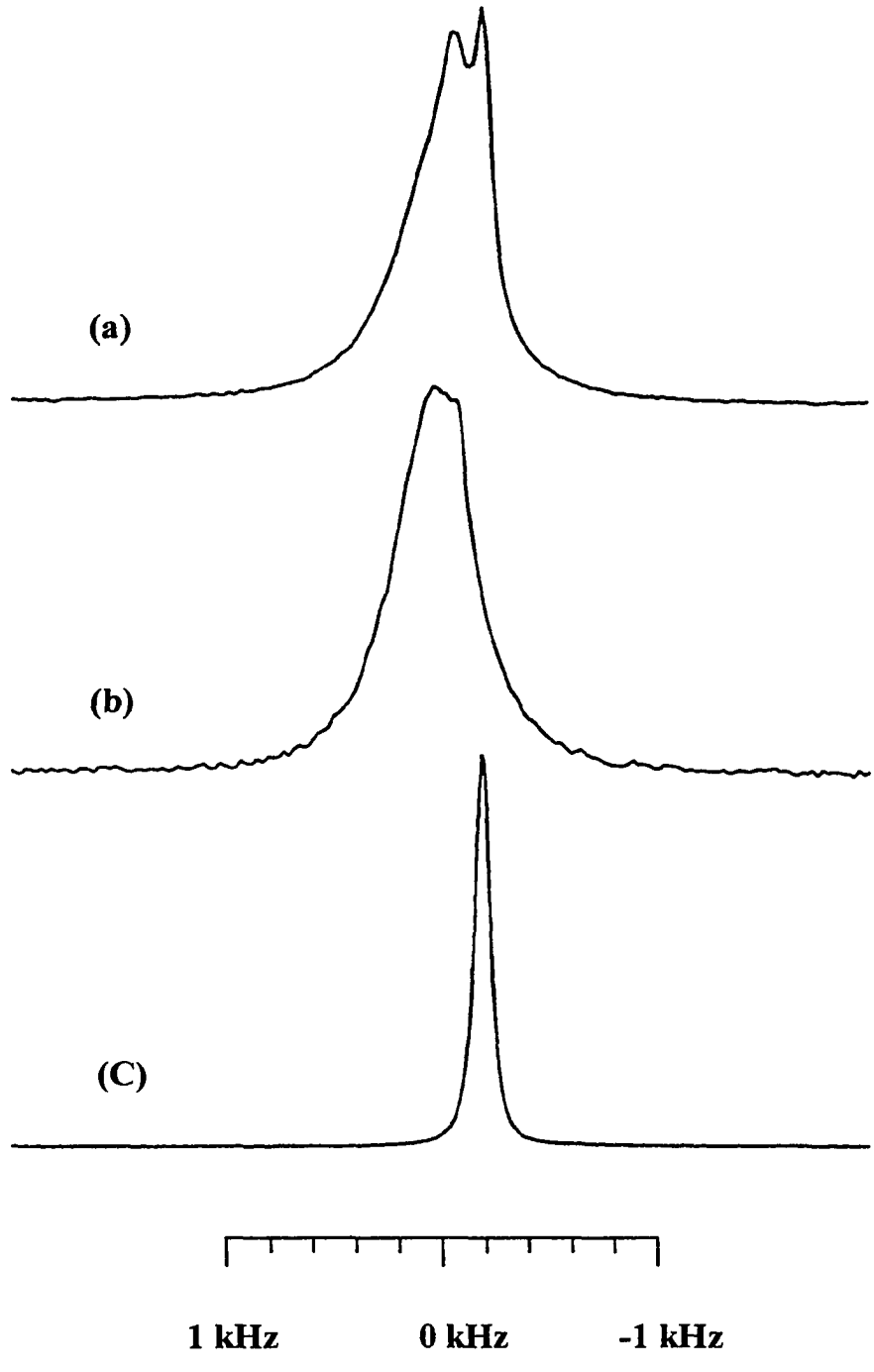

Figure 4-37: High resolution CP/MAS (spinning rate 5.5 kHz) ^{7}Li NMR spectra for (a) LiIP(EO)$_{1.5}$ 6%Al_2O_3 at 23°C; (c) LiIP(EO)$_{1.5}$ 6% Al_2O_3 at 80 °C; (c) LiIP(EO)$_9$PMMA$_{0.5}$EC$_1$ 6%Al_2O_3 at 23°C.

with an optimized CP contact time of 3 ms; variations in contact time cause changes in the peak. The greater sensitivity of this peak to CP conditions is thus ascribed to the proximity of the ^{7}Li nuclei to protons associated with the polyether chains. When the temperature is raised to 80°C (**Figure 4-37(b)**), the spectral splitting disappears and the center of the spectrum is shifted toward the ionic Li reference. This result is significant in that it implies that at elevated temperatures corresponding to the conductivity jump region[86], where Li^{+} ion transport readily occurs, the Li environment is almost purely ionic rather than solvated by the polyether oxygen. This outcome is important in understanding the nature of the ion transport mechanism in concentrated CSEs, and it is consistent with the previously stated conclusion that polymer segmental motion is not a deciding factor in concentrated electrolytes to the extent that it is in dilute electrolytes. For completeness, it is noted that the spectrum of **Figure 4-37(c)** is centered approximately at the position associated with the polyether-solvated Li, it exhibits strong CP effects and shows little change at 80°C. These results are not expected for this more dilute electrolyte.

4-7.3. Sub-conclusions

Several PEO-based CSEs, which are characterized by much higher salt concentrations than in "conventional" polymer electrolytes, were investigated by solid state NMR. High-resolution NMR results for the concentrated CSE indicate at least two Li environments, one solvated by PEO and one in ionic clusters at room temperature. At 80°C, the Li environment becomes more purely ionic as the polymer-associated peak vanishes. The confluence of the conductivity [94] and the change in Li environment

suggests that the conduction mechanism in concentrated CSEs is quite different than that in more dilute polymer electrolytes.

4-8. Summary of conclusions

By applying Nuclear Magnetic Resonance (NMR) methods to many materials used in secondary batteries, this thesis has confirmed that NMR is a powerful method to investigate the immediate environment of ions such as Li^+. The materials involved in the work include:

Cathode materials: $Li_{1+y}CoO_2$, $LiCo_xNi_{1-x}O_2$ and $Li(Cr,Fe)_xMn_{2-x}O_4$.

Anode materials: lithiated graphite, disordered carbons and lithiated SnO.

Composite Solid electrolytes PEO-LiI, LiI/Al_2O_3.

1. Lithium insertion in hard carbon

In high-resolution MAS experiments, the fully lithiated hard carbon exhibited three features(50 ppm, 17 ppm and 0 ppm) in which are attributed to: 1) intercalated Li^+ ions residing between graphene rings (50 ppm), 2) HVR portion of the lithium insertion (17 ppm), 3) SEI (0 ppm). It was concluded that high Li capacity hard carbon exhibits two distinct insertion mechanisms (50 ppm and 17 ppm), which is intercalation between disordered graphene planes and possibly covalent C-Li bond to defect sites. In addition, there is very small evidence of the presence of LiH in the proton decoupled NMR experiments.

2. Lithiated natural graphite before and after mild oxidation

Solid state ^7Li NMR measurement identified two kinds of Li sites in lithiated graphite: Li intercalated between graphene planes, with ~40 ppm Knight shift, and Li

chemically associated with the SEI, characterized by a chemical shift around 0 ppm. The partially oxidized graphite also exhibited a feature around 14 ppm correlated with excess Li and attributed to Li bonded to edge, or other sites. In addition, the ^{7}Li signal associated with the SEI was more intense in the burnt graphite, consistent with earlier indications that mild oxidation prior to lithiation results in thicker and more salt-rich SEI.

3. Electrochemically lithiated SnO

High-resolution ^{7}Li NMR spectra of SnO/Li samples with ratios ≤ 2.0 are attributed to amorphous Li_2O. ^{7}Li MAS NMR spectra for samples with Li/SnO ratio equal to 4.3 exhibit three distinct Li environments corresponding to the intense feature are ~17 ppm, large shoulder centered at around 0 ppm and a smaller peak at around 43 ppm. The 0-ppm shoulder is attributed to the same amorphous Li_2O phase. Other peaks arise from Knight shift interactions in the metallic Sn/Li phase. At the maximum Li/SnO ratio (6.40) the Li environments of the lithiated SnO and reference $Li_{x-2}Sn$ alloy are very different, suggesting that the metallic $Li_{4.4}Sn$ phase formed by electrochemical lithiation of the oxide is structurally different than that of the melt-prepared alloy.

4. $Li_{1+y}CoO_2$

The battery cathode materials $Li_{1+y}CoO_2$ (y=0.0, 0.8, 0.35), and Mg-doped $Li_{1+y}CoO_2$: Mg (y= 0.08) were investigated by solid state NMR. Wide-line ^{7}Li and ^{6}Li absorption spectra of stoichiometric $LiCoO_2$ reveals that Li is completely ionized. The Li is located at octahedral symmetry sites as evidenced by lack of quadrupole splittings in both the $^{7,6}Li$ wide-line spectra. For ^{7}Li, the sources of line -broadening mainly come

from the ^{7}Li-^{7}Li homonuclear and ^{59}Co heteronuclear dipole-dipole interactions. The linewidths of y=0.08 and 0.35 samples increase about 10% compared to the stoichiometric $LiCoO_2$. Spin-Lattice relaxation measurements yield T_1 of about 390, 144 and 137 ms for y=0.0, 0.08 and 0.35 samples, respectively. The enhanced line width and relaxation rates in the excess Li sample is attributed to the generation of Co^{2+}. With variable temperature experiments, the far-shifted features at 40 kHz and 160 kHz in y=0.35 sample are attributed to Li^{+} ions in closer proximity to paramagnetic Co^{2+} because the features move further downfield with decreasing temperature. MAS spectra also detect some ionic impurity phase. The effect of Mg doping of the excess Li sample is either to generate Co^{4+} ions or to increase the efficiency with which the excess Li enters the structure ionically while reducing the Co valence.

5. $LiCo_xNi_{1-x}O_2$ and $Li(Cr,Fe)_xMn_{2-x}O_4$

For $LiCo_xNi_{1-x}O_2$ sample system, NMR line widths show a 1/T dependence, consistent with the temperature dependence of magnetic susceptibility in a strongly paramagnetic system. The ^{7}Li NMR line widths and spin-lattice relaxation (T_1) behavior are dominated by strong interactions with the paramagnetic Ni^{3+}. The presence of 5% excess Li causes almost no change in NMR line width or T_1 in the mixed (Ni/Co) cathode, but does produce an almost 30% reduction in line width for the pure $LiNiO_2$, implying that Co stabilizes the structure. With $Li(Cr,Fe)_xMn_{2-x}O_4$ sample system, a correlation between paramagnetic chemical shifts (decrease) and line widths (increase) with 3d electrons (increasing in order of Cr, Mn and Fe) was found.

6. LiI/Al_2O_3 Mixtures

High resolution MAS ^{7}Li NMR measurement demonstrates the presence of two or more inequivalent sites, which depend on mixture composition as well as temperature. The site population of Li+ ions in the non-bulk LiI phase is comparable to that in the bulk LiI phase at the 50/50 composition at elevated temperature, reflecting the very large effective interfacial region this material. ^{7}Li spin-lattice relaxation measurements indicate that with the content of Al_2O_3 increasing, the ^{7}Li spin-relaxation decreases. In variable temperature ^{127}I T_1 measurements, All samples exhibit a shallow T_1 minimum between roughly 25° and 45°C. That the pure LiI ^{127}I T_1 does not show a minimum in the same temperature range as the mixture indicates that there is dynamical effect, attributable to mobile Li^+ ions, which have a small but discernable influence on the I^- environment.

7. Composite Solid Electrolytes Based on PEO, LiI and High Surface Area Inorganic Oxides

High-resolution NMR results for the concentrated CSE indicate at least two Li environments, one solvated by PEO and one in ionic clusters at room temperature. At 80°C, the Li environment becomes more purely ionic as the polymer-associated peak vanishes. The confluence of the conductivity jump (observed by electrical measurements) and the change in Li environment suggests that conduction mechanism in concentrated CSEs in quite different than that in more dilute polymer electrolytes where polymer segmental motion is required for the latter.

References

1. M. B. Salamon, Physics of Superionic Conductors, Spriger, (1979).
2. D. W. Murphy et.al., *Mater. Res. Bull.*, 13, 1395 (1978).
3. J. B. Goodenough, D. G. Wickham, and W. J. Croft, *J. Appl. Phys.*, 29, 382(1958).
4. J. B. Goodenough, K. Mizushima, and T. Takeda, tpn. *J. Appl. Phys.*, 19, 305(1980).
5. K. Nassau and D. W. Murphy, *J. Non-Cryst. Solid*, 44, 297(1981).
6. K. Mizushima, P. C. Jones, P. J. Wiseman, and J. B. Goodenough, *Mater. Res. Bull.*, 15, 783(1980).
7. M.G.S.R Thomas, W. I. Thackeracy, J. B. Goodenough and P. Groves, *Mater. Res Bull.*, 20, 1137 (1985).
8. T. Nagaura, *Prog. Batt. & Batt. Mater.*, 10, 209 (1990).
9. J. R. Dahn, U. Von Aackon and C. A. Michal, *Solid State Ionics*, 10. 87 (1990).
10. M. Carewska, S. Scaccia, Fausto Croce, S. Arumugam, Y. Wang, S. Greenbaum, *Solid State Ionics*, 93, 227(1997).
11. T. Ohzuku, H. Komori, K. Sawai, and T. Hirai, *ibid.*, 5, 733 (1990).
12. F. Capitaine, P. Gravereau, and C. Delmas, *Solid state ionics*, 89, 197(1996).
13. B. Garcia, P. Barboux, F. Ribot, A. Kahn-Harari, L. Mazerolles, N. baffier, *Solid State Ionics*, 80, 111 (1995).
14. B. Ouyang, X. Cao, H. W. Lin, S. Slane, S. Kostov, M. denBoer, S. G. Greenbaum, Mater. Res. Soc. Symp. Proc. 369, 59-68 (1995).

15. M. P. J. Peters, M. J. van Bommel, P. M. C. neilen-ten Wolde, H. A. M. Van Hal, W. C. Keur, A. P. M. Kentgens, *Solid State Ionics* 112, 41-52 (1998).

16. M. M. Thackeray, P. Johnson, L. A. de Picciotto, P Bruce and J. B. Goodenough. *Mater. Res. Bull.*,19. 179 (1984).

17. F. K. Shokoohi, J. M. Tarascon, B. J. Wilkens, D. Guyomard, and C. C. Chang, *J. Electrochem. Soc., 139,* 1845 (1992).

18. G. Pistoia, G. Wang and C. Wang, *Solid State Ionics*, 58, 285 (1992).

19. P. Endres, b. fuchs, S. Kemmler-Sack, K. Brandt, G. faust-Becker, H. W. Praas, *Solid State Ionics*, 89, 221 (1996).

20. Yasushi Kanzaki, Akira Taniguchi, and Mitsuo Abe, *J. Electrochem. Soc.*, 138, 333 (1991).

21. W. John, *Phys. Rev.*, 96, 590(1954).

22. P. Ganguly, V. Ramaswamy, I. S. Mulla, R. F. Shinde, and P. P. Bakare, *Phys. Rev.*, 46, 595(1992).

23. M. Itoh, I. Yamada, K. Ubukoshi, K. Hirakawa, and H. Yasuoka, *J. Phys. Soc. Jpn.* 55, 2125 (1986).

24. G. Villenuve, T. Rojo, G. Demazeau, and P. Hagenmuller, *Mater. Res. Bull.* 23, 1787 (1986).

25. G . Pistoia (Ed.) Lithium Batteries, New materials, Development and Perspective, Elsevier, Amsterdam (1994).

26. R. Fong, V. von Saken, and J. R. Dahn, *J. Electrochem. Soc.*, 137, 2007 (1990).

27. N. Imanishi, S. Ohashi, T. Ichikawa, Y. Takeda, O. Yamamoto and R. Kanno, *J. Power Sources*, 39, 185(1992).

28. N. Imanishi, H. Kashiwagi, T. Ichikawa, Y. Takeda, O. Yamamoto and M. Inagaki, *J. Electrochem. Soc.*, 140, 315 (1993).

29. Y. Mori, T. Ishikawa, Iriyama, T. hashimoto, S. yamazaki, F. Kawakami, H. Shiroki, T. Yamabe, *J. Power Source*, 68, 263 (1995).

30. S. Surampudi, C. K Huang, M. C. Smart, D. Perrone, and B.V.Ratnakumar, Review and Status of Lithium Ion Cell Technology for Aerospace Applications, (1997).

31. K. Tatsumi, T. Akai, T. Imamura, K. Zaghib, N. Iwashita, S. Higuchi, and Y. Sawada, *J. Electrochem. Soc.*, 143, 1923 (1996).

32. N. Takami, A. Satoh, T. Ohsaki, and M. Kanda, *Electrochimica Acta*, 42, 2537(1997).

33. Satoh et al, private communication.

34. A. Nagai, M, Ishikawa, J. Masuko, N. Sonobe, H. Chuman, T. Iwasaki, *MRS Symp. Proc., Materials for Electrochemical Energy Storage*, 393, 339.

35. K. Sato. M. Noguchi, A. Demachi, N. Oki, M. Endo, *Science* 264, 556(1994).

36. Y. Idota, etc., European Patent #0651450A1.

37. J. R. Dahn, I. A. Courtney and O. Mao, *Solid State Ionics*, 111, 289(1998).

38. C.C Liang, *J. Electrochem. Soc.*, 120, 1289(1973).

39. A. M. Stoneham, E. Wade, J. A. Kilner, *Mat. Res. Bull.*, 14, 601(1979).

40. G. Wang, Z. Li, L. Chen and Z. Zhao, *Acta Phys. Sincia* 30, 1569(1981).

41. O. Nakamura, J. B. Goodenough, *Solid State Ionics*, 7, 119(1982).

42. J. L. Bjorkstam, M Villa, M, Rahman, P. M. Skarstad, *Solid State Ionics* 9&10, 111(1983).

43. R. Dupree, J. R. Howells, A. Hooper, F. W. Poulsen, *Solid State Ionics* 9&10, 131 (1983).

44. G. Wang et al , KEXUE TONGBAO, 26, 308 (1981).

45. F. M. Gray, *Solid Polymer Electrolytes*,VCH Publishers, Cambridge(1991).

46. D. Baril, Y. Chabre and M. B. Armand, *J. Electrochem. Soc.*, 140, 2687(1993).

47. F. Croce and B. Scrosati, *J. Power Sourecs*, 9, 43(1993).

48. E. Peled, D. Golodnitsky, G. Ardel and V. Eshkenazy, *Electrochim. Acta* ,40 2197(1995).

49. G. Ardel, D. Golodnitsky, E. Stauss and E. Peled, *J. Power Sources*, in press.

50. G. Ardel, D. Golodnitsky, E. Strauss, E. Peled, Proceedings of the 37th Power Sources Conference(ARL), 283(1996).

51. S. Wong and D. B. Zax, *Electrochim. Acta,* 12, 3513(1997).

52. R. Selim and P. Bro, *J. Electrochem. Soc.*, 121, 1467(1974).

53. J. Jorne and C. W Tobias, *J. Appl. Electrochem.*, 5, 279 (1975).

54. R. D. Rauh and S. B. Brummer, *Electrochim Acta*, 22, 75(1977).

55. V. R. Koch and J. H. Young, *J. Electrochem Soc.*, 125, 1371(1978).

56. F. Bloch, W. W. Hansen, and M.E. Packard, *Phys. Rev.*, 69, 127 (1946).

57. E. M. Purcell, H. C. Torrey, and R. V. Pound, *Phys. Rev.*, 69, 37-38 (1946).

58. C. P. Slichter, Principles of Magnetic Resonance, Springer- Verlag (1978).

59. A. Abragam, The Principles of Nuclear Magnetism, Oxford University Press, London (1978).

60. M. Mehring, High Resolution NMR Spectroscopy in Solids, Springer-Verlag (1976).

61. P. C. Taylor and P. J. Bray, *J. Mag. Res.*, 2, 305(1970).

62. M. H. Cohen and F. Reif, Solid State Physics, Vol 5, 321 (1957).

63. W. H. Jones, Jr., T.P. Graham, and R.G. Barnes, *Phys. Rev.*, 132, 5 (1963).

64. E. Fukushima and S.B.W. Roecder, Experimental Pulse NMR, A Nuts and Bolts Approach, Addison-Wesly Publishing Company, Inc (1981).

65. E. L. Hahn, *Phys. Rev.*, 80 580 (1950).

66. R. Chen, Nuclear Magnetic Resonance Studies of Water in Perfluorinated Ion Exchange Membrances, Ph.D Thesis in CUNY (1994).

67. CMX, User's Guide, (1994).

68. Y. Dai, Y. Wang, V. Eshkenazi, E. Peled, and S. G. Greenbaum, *J. Electrochem. Soc.*, 145, 1179(1998).

69. J. Conard and H. Estrade, *Mater. Sci. Eng.*, **31**, 173 (1977).

70. J. Conard, V. Nalimova, and D. Gerard, *Mol. Cryst. Liq. Cryst.*, 245, 25 (1994).

71. C. Menachem, E. Peled, and L. Burstein, 37th Power Sourcee Conference, p208, IEEE(1996).

72. J. W. Akitt, in Multinuclear NMR, J. Mason, Editior, p192, Plenum press, New York (1987).

73. O. Chusid, Y. Ein-Eli, and D. Aurbach, *J. Power Sources*, 43, 47 (1993).

74. H. Momose, H. Honbo, S. Takeuchi, K. Nishimura, T. Horiba, Y. Muranaka, Y. Kozono, and H. Miyadera, in Eighth International Meeting on Lithium Batteries, p 172 (1996).

75. C. Menachem, E. Peled, L. Burstein, and Y. Rosenberg, *J. Power Sources*, 68, 277(1997).

76. E. Peted, D. Golodnitsky, and J. Penciner, in Handbook of Battery Materials, J Bensenhard, Editor, In press.

77. T. Zhang, Y. Liu, E. W. Fuller, S. Tseng, U. von Sacken, and J. R. Dahn, *J. Electrochem. Soc.*, 142, 2581(1995).

78. J. R. Dahn, T. Zheng, Y. Liu, and J. S. Xue, *Science*, **270**, 590 (1995).

79. P. Papaneck, M. Radosavljevic, and J. Fischer, *Chem. Mater.*, **8**, 1519 (1996).

80. E. Peled, C. Menachem, D. Bar-Tow, A. Melman, *J. Electreochem Soc.*, 143(1996) L4.

81. C. Menachem , Y. Wang, J. Flowers, E. Peled, S.G. Greenbaum. *J. Power Sources* 3203 (1998).

82. E. Pelled, , Rechargeable lithium and lithium - -ion batteries, The Electrochem. Soc. Proceedings Series 94-28 (1995).

83. E. Peled, D. Golodnitsky , G. Ardel, C. Menachem, D Bar-Tow, V. Eshkennazi, Proceedings of the 1995 MAS Spring Meeting 393 , 209(1995).

84. Y. Wang, J. Sakamoto, C. K. Huang, Surampudi, S. G. Greenbaum, *Solid State Ionics*, 110, 167(1998).

85. I. A. Courtney, J. R. Dahn, *J. Electrochem. Soc.*, 144, 2045 (1997).

86. J. Mason (Ed.), Multinuclear NMR. Plenum Press, New York, (1987).

87. Y. Idota, T. Kobota, A. Matsufuji, Y. Maekawa, T. Miyasaka, *Science*, 276, 1395(1997).

88. T. B. Massalski (Ed.) Binary Alloy Phase Diagrams, 2nd Edition, ASM International Materials Park, Ohio, 3, 2469(1990).

89. D. R. Lide (Ed.), CRC Handbook of Chemistry and Physics , 74th Edition, CRC Press, Boca Raton, p. 12 (1993).

90. S. Kostov, Y.Wang, M. L. denBoer, S. Greenbaum , C. C. Chang, and Prashant N. Kumta, Mat. Res. Soc. Symp. Proc. 496, 427(1998).

91. Periodic table of the chemical elements, Aldrich chemical company. Inc.

92. G. Ardel, D. Golodnitsky, Emanuel Peled, Y. Wang G. Wang, S. Bajue and S. Greenbaum, *Solid State Ionics*, in press.

93. Y. Dai, S Greenbaum, D. Golodnitsky, E. Strauss and E. Peled and Y. Rosenberg, Solid State *Ionic, Solid State Ionics*, 106, 25(1998).

94. Y. Dai, Y. Wang, S. Bajue, S. Greenbaum, D. Golodnitsky, G. Ardel, E. Strauss, E. Strauss, E. Peled, *Electrochim, Acta*, 43, 1557(1998).

95. E. Peled, D. Golodnitsky, G. Ardel and V. Eshkenazy, *Electrochim, Acta*. 40, 2197(1995)

96. S. D. Brown, S. G. Greenbaum, M. G. McLin, M. C. Wintersgill and J.J. Fontanella, *Solid State Ionics*, 67, 257 (1994)